Mechanical Intelligence in Millimeter-Scale Machines

Thesis advisor
Robert J. Wood

Author
Pratheev Sabaratnam Sreetharan

Mechanical Intelligence in Millimeter-scale Machines

Abstract

Advances in millimeter-scale fabrication processes have enabled rapid progress towards the development of flapping wing micro air vehicles with wing spans of several centimeters and a system mass on the order of 100mg. Concerning flight stability and control mechanisms for these mass and power limited devices, this dissertation explores the use of underactuated "mechanically intelligent" systems to passively regulate forces and torques encountered during flight. Several experiments demonstrate passive torque regulation in physical flapping wing systems. Finally, this dissertation concludes with a detailed description of the Printed Circuit MEMS manufacturing process, developed to address the practical problem of building complex insect-scale machines.

Contents

Acknowledgments

First and foremost, I would like to thank my parents Sree and Mathini, my brothers Rajeev and Sanjeev, and my girlfriend Abby Chapman for their support and encouragement during my years of research. Without them, I would neither have been able to endure trying times nor fully enjoy my successes.

My advisor Professor Robert Wood has my gratitude for his advice and seemingly bottomless tolerance of my constant distraction with crazy research ideas. Professor Paul Horowitz and Dr. Lee Grodzins have also been important mentors to me, demonstrating the importance of curiosity and imagination in research. I must also thank Peter Whitney and all of my other colleagues at the Harvard Microrobotics Lab for years of conversation and collaboration, without which this work would not have been possible.

Finally, I would like to thank my funding sources, which include Harvard University, the Wyss Institute, the NSF, the NDSEG, and, of course, my parents when times were tight.

Chapter 1

Introduction

1.1 Hovering at 100mg

Advances in millimeter scale fabrication processes have enabled rapid progress towards the development of flapping wing micro air vehicles (FWMAVs) with wing spans of several centimeters and a system mass on the order of 100mg. Larger examples include the 16g Delfly II and the highly functional 19g AeroVironment hummingbird [17, 25]. At-scale devices include the Berkeley Micromechanical Flying Insect (MFI) and the Harvard Microrobotic Fly (HMF), both constructed with advanced composites using the Smart Composite Microstructure (SCM) manufacturing process [13, 40, 41]. The 60mg HMF is notable as the first sub-100mg FWMAV capable of producing thrust greater than the mass of its aeromechanical structure, though power and drive electronics are external.

This dissertation considers flight stability and control mechanisms for these mass and power limited systems, which remain active areas of research. Investigation into

the aerodynamics of biological insect flight has produced approximate aerodynamic models allowing computationally inexpensive prediction of aerodynamic forces and torques from wing trajectories [11, 12]. Accordingly, research into transmission and control mechanisms of flapping wing robotic insects has focused on control of wing trajectory. For example, the MFI is a FWMAV platform with the ability to execute a range of predetermined wing trajectories using a fully actuated wing drive mechanism, neglecting elastic deformation of the transmission and wings.

In one notable exception, the HMF has proven capable of realizing qualitatively biomimetic wing trajectories using passive compliance to allow variation of wing angles of attack. The associated reduction in complexity is a crucial advantage allowing the device to achieve takeoff. However, research into flight control largely proceeds along conventional lines of direct modification of wing trajectories [15, 28].

In a departure from conventional approaches to flapping wing flight control, this dissertation argues for the introduction of supplemental degrees of freedom into flapping wing drivetrains. Addition of mechanical complexity results in rich dynamic behavior that can be tuned to mechanically regulate forces and torques encountered during operation without the intervention of an active controller. Termed passive aeromechanical regulation of imbalanced torques (PARITy), this approach is atypical for FWMAVs but finds analogues in a diverse collection of other applications including automobiles and rotorcraft. Similar to its impact in other applications, it is hoped that PARITy designs will reduce performance requirements on active control systems by shifting the burden onto "mechanically intelligent" structures, leading to an overall system that is more robust.

1.2 Manufacturing at 100mg

An argument for increasing mechanical complexity, however, must respond to the immense challenge of manufacturing at the millimeter to centimeter scale. A multitude of conventional manufacturing techniques exist to create machines measured in centimeters or meters. Microelectromechanical systems, or MEMS, is a maturing industry that adopts integrated circuit technology to produce sub-millimeter Silicon-based machines with a more limited set of materials and topologies [24]. A 100mg insect-inspired flapping wing robot requires mesoscale manufacturing, existing on a size scale between these two manufacturing paradigms.

Existing mesoscale manufacturing techniques struggle to produce even unsophisticated flapping wing devices. MEMS approaches cannot easily attain complex topologies and lack the ability to incorporate performance materials or high power density actuators. Three-dimensional printing approaches can attain complex topologies but do not solve material or actuation concerns. The HMF relies on the SCM manufacturing paradigm, which allows complex topologies, high-performance actuators, and advanced structural composites at the cost of manufacturing precision and yield [41]. Though SCM has enabled takeoff of the HMF, manufacturing a successful device requires months to years of training, a jeweler's skill, and a fair bit of luck. Furthermore, each artisan device differs in performance from the next.

This dissertation addresses the mesoscale manufacturing problem by introducing Printed Circuit MEMS (PC–MEMS), a new process for manufacturing machines at the millimeter to centimeter scales. Whereas Silicon MEMS is based on integrated circuit manufacturing, the printed circuit board (PCB) industry inspires PC–MEMS

manufacturing. It allows a wide variety of materials, integrated high-performance actuators, and access to a range of three-dimensional topologies. Furthermore, PC–MEMS accepts pick-and-place external components and has expected compatibility with integrated electronic circuits from the industry that inspires it. Finally, by removing all artisanal operations and relying only on volume-scalable process steps, it provides a path for manufacturing high performance, mesoscale machines on an industrial scale. Expected to have a broad impact beyond FWMAV control, PC–MEMS provides a general mesoscale manufacturing platform for microrobotics and other mesoscale machines.

1.3 Organization

Chapter 2 focuses on theoretical topics, discussing mechanically regulated systems and the properties of several PARITy-enabled designs for FWMAVs, including the 'Drag PARITy' design for mechanically regulating roll torque. Chapter 3 bridges theory and practice, covering a numerical simulation model and two experimental case studies testing a Drag PARITy drivetrain manufactured with SCM techniques. Chapter 4 focuses on manufacturing, describing the PC–MEMS process for creating mesoscale machines, several demonstrative devices, and a monolithic, mass producible design for a 90mg FWMAV known as the Monolithic Bee (Mobee). Chapter 5 provides concluding remarks and describes the future of both PARITy and PC–MEMS.

Sections of this dissertation have been published in scientific literature. Elements from Chapters 2 and 3 appear in [32], [34], and [35]. The general PC–MEMS capabilities from Chapter 4 appear in [33] and [38].

Chapter 2

Mechanical Intelligence

2.1 Introduction: mechanically regulated systems

Tuned mechanical elements are capable of regulating the behavior of many systems, often enjoying the advantages of simplicity and robustness as compared to their active electronic counterparts. Such mechanical elements give rise to the term "mechanical intelligence," as they can fulfill a role more typically occupied by sophisticated electronic control systems. A wide variety of machines including automobiles, fixed-wing aircraft, and rotorcraft take advantage of tuned mechanisms to regulate their operation. This section will review some common mechanically intelligent systems to give insight into how similar mechanisms can pertain to flapping wing flight control.

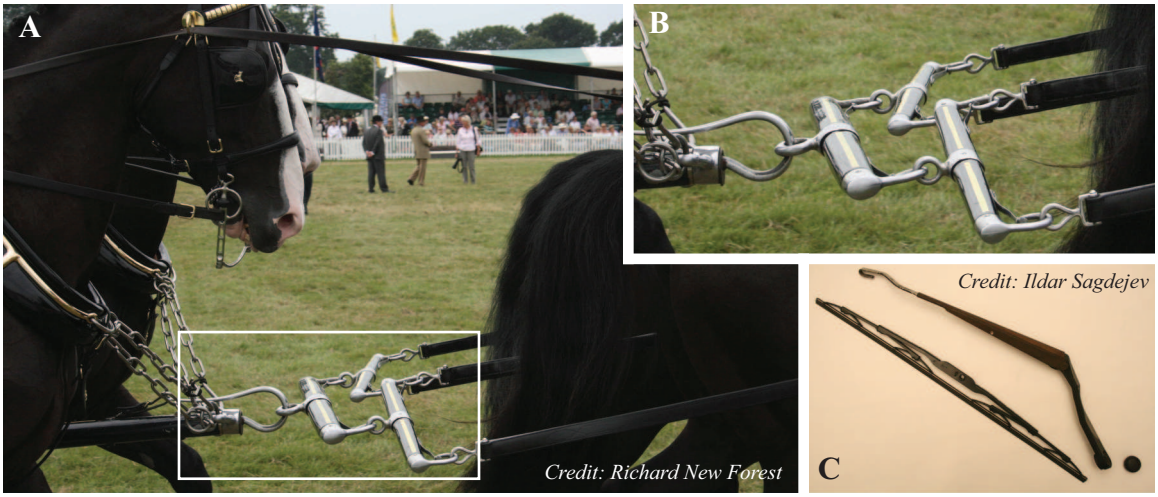

Figure 2.1: Common examples of passive force balancing using whippletrees. (A) Whippletrees are used to balance forces on a single draft animal and between multiple draft animals. (B) An enlarged view of the mechanism. (C) A common windshield wiper design uses multiple whippletrees to distribute force evenly across the wiper blade.

2.1.1 The whippletree

The whippletree is a simple mechanism involving a beam allowed to pivot freely about an internal axis. When the pivot is centered, a force applied to the pivot perpendicular to the beam will be divided evenly to two loads at either end of the beam. The beam rotates dynamically about the pivot, adapting to varying displacement of the loads to regulate forces. This allows, for example, both sides of a draft animal to be coupled to a heavy cart while still allowing it to walk freely (Figure 2.1A-B). Multiple whippletrees can be cascaded to accommodate many animals, and moving the central pivot along the beam alters the distribution of force to each end.

A similar problem in distributing force arises in wiping moisture off of a windshield. A modern windshield has a complex curved profile, and a wiper traverses this profile in an arc. The wiper blade itself must warp precisely during each stroke to maintain even pressure on the windshield. A typical electronic system directly controlling blade shape would involve an array of force or displacement sensors and a multitude of actuators in order to achieve the correct behavior. However, the problem is fundamentally one of distributing a force as opposed to determining a wiper blade configuration; ideally, a wiper blade will attain whatever shape necessary to ensure an evenly distributed force across the blade. Similarly, an FWMAV should execute whatever wing trajectories necessary to ensure proper forces and torques on the airframe.

A classic windshield wiper design involves a cascade of whippletrees connecting the wiper arm and the blade. Figure 2.1C shows a whippletree cascade attaching to eight points on the wiper blade. This mechanism distributes the force applied to the

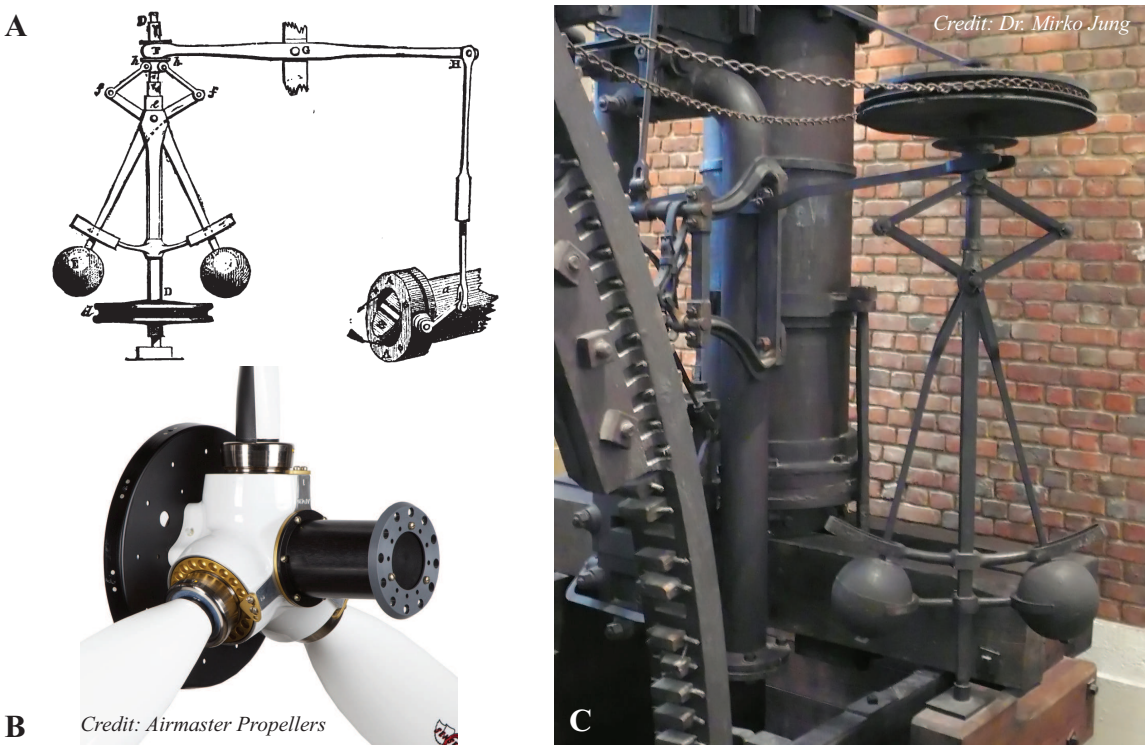

Figure 2.2: (A) A schematic diagram of a centrifugal governor. A modern embodiment can be found within (B) constant speed propellers, or in its (C) original form to regulate a steam engine.

wiper mechanism evenly among eight points on the wiper blade. This mechanically regulated system achieves a complex trajectory passively, without active control.

2.1.2 The centrifugal governor

The centrifugal governor is another classic mechanism used to regulate the operation of dynamic systems. Weights suspended from a rotating shaft experience a centrifugal force in the rotating frame, causing the weights to extend outwards as the rotation rate increases. The extension of the weights drives a mechanism that tends

to reduce the rotation rate. In the case of an engine this is often a valve restricting the entry of fuel or working fluid. In the case of a constant speed propeller, this is often a pump that hydraulically actuates the propeller blade angle of attack.

2.1.3 The helicopter stabilizer

Consider an idealized two-winged flapping insect capable of (1) a 180° wingstroke, (2) a constant-speed wing stroke with instant stroke reversal and (3) fixed angle of attack with instant rotation at stroke reversal. This scenario is exactly that of a helicopter with two superimposed, counter-rotating rotors, each with a single fixed-pitch blade. Though quite similar, the phenomena of stroke reversal, stroke plane deviation, and variable angle of attack cause FWMAV dynamics to deviate from helicopter dynamics.

However, it is telling that mechanically intelligent elements are are present in some large helicopters and ubiquitous in small radio-controlled models. These mechanical or aeromechanical elements, often integrated into the rotor mechanism, oppose disturbances in helicopter attitude and slow down the dynamics of the system. In-depth dynamic analysis of these systems' function can be quite complex [23]. Several common designs will be mentioned; more details can be found in [23].

The *Bell stabilizer bar* is an inertial rotor mounted coaxially with a twin-blade helicopter rotor (Figure 2.3). The stabilizer acts as a gyroscope, maintaining its orientation in the earth frame. A disturbance to the attitude of the helicopter body causes the axis of rotation of the stabilizer to deviate from the axis of rotation of the main rotor. This deviation is mechanically coupled into the rotor mechanism to

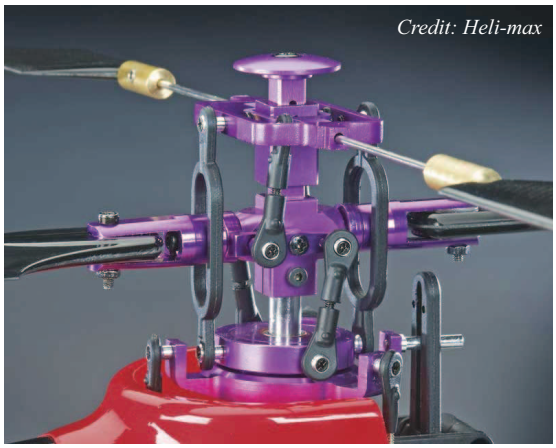

Figure 2.3: (left) The Bell Sioux H-13, incorporating a stabilizer bar. (right) A Heli-max Axe CPv3 radio controlled helicopter incorporating a Bell-Hiller stabilizer.

cyclically alter main rotor blade pitch so as to correct the disturbance.

The *Hiller stabilizer* extends the Bell stabilizer by adding an aeromechanical component in the form of small airfoils at the ends of the stabilizer bar. Active control of the swashplate, instead of directly impacting the pitch of the main rotor blades, instead drives the pitch of the stabilizer bar airfoils. The active control input perturbs the mechanical regulation mechanism instead of directly driving the main rotor airfoils, an approach that is a cornerstone of the PARITy control methodology introduced in later sections.

Most small radio-controlled helicopters use a hybrid mechanism known as a *Bell-Hiller stabilizer* (Figure 2.3). This mechanism couples active control into the rotor system using both techniques, directly driving main rotor pitch as in the Bell stabilizer, but also driving stabilizer airfoils as in the Hiller stabilizer. These two inputs are mechanically mixed in the rotor mechanism, allowing the balance between responsiveness and stability to be tuned.

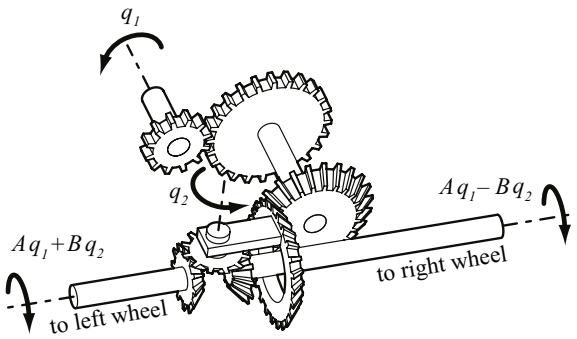

Figure 2.4: A car differential balances output torques using an underactuated mechanism. Degree of freedom q_1 receives engine torque while q_2 is unactuated.

Other mechanically intelligent systems exist for multi-bladed rotorcraft, for example, the gyroscopic Lockheed system for four-bladed rotors. Though rotational gyroscopes are difficult to implement in small flexure-based systems, they have a reciprocating analogue known as the vibrating structure gyroscope. Such a structure is present in many biological fliers and in this context is called a haltere. Though biological halteres are thought to be purely sensory, haltere-based mechanically intelligent flapping mechanisms are an interesting tract for future research.

2.1.4 The differential

The drivetrain for an FWMAV shares several characteristics with that of a classic two-wheel-drive automobile. Both devices must deliver power from a single actuator to two end effectors. In the case of an automobile, the actuator is an internal combustion engine whose single output shaft must drive two wheels. In the case of an FWMAV, the actuator can be a single piezoelectric cantilever that drives two wings.

In these devices, the drivetrain, defined here as a mechanism connecting the actu-

ator to the two end effectors, must accomplish two tasks: it must map the actuation stroke to the end effector strokes and it must distribute the available power amongst the two end effectors. The first task is accomplished by a device called a transmission. The automobile traditionally uses a 1DOF gearbox, though several discrete transmission ratios can be automatically or manually selectable.

A mechanistically simple method for executing the second task, the apportionment of available power, is to constrain the relationship of end-effector displacements. Balanced displacement of each end-effector, however, is not the ideal apportionment of actuator power. The automobile drivetrain from Figure 2.5 is not used in practice because of its poor performance during turns. Executing a turn without wheel slip requires the inner and outer wheels to rotate at different speeds. A drivetrain that distributes power in this equal-displacement fashion will waste power by causing one or both wheels to slip during a turn.

An alternative approach is to mechanically regulate wheel rotation so as to balance the torque delivered to each wheel. This intelligent mechanism, called a differential, is ubiquitous in automotive design. The differential (Figure 2.4) functions by introducing an additional degree of freedom to the 1DOF drivetrain of Figure 2.5. In an automobile drivetrain incorporating a differential, the engine shaft rotation q_1 no longer determines the individual wheel rotations, rather, it prescribes the *sum* of the wheel rotations. The degree of freedom q_2 introduced by the differential is proportional to the *difference* of the wheel rotations; its trajectory is determined not by an actuator, but by the system dynamics. The differential mechanism is designed such that q_2 passively follows a trajectory that results in an equal torque on each of the

two output shafts.

The Drag PARITy drivetrain, discussed in §2.4 is an embodiment of a differential for a flapping wing robotic insect. In an automobile, a differential allows individual wheels to rotate independently, but distributes power from the engine so as to balance the output torques. Similarly, Drag PARITy allows the wings to follow independent stroke trajectories, but delivers a balanced roll-aligned torque (Figure 2.10) to each.

2.2 The PARITy methodology

Though it would allow for a highly capable FWMAV, fully-actuated high-bandwidth control of wing trajectories has not been achieved on a 100mg platform. Millimeter-scale fabrication techniques have not yet demonstrated the requisite complexity within mass constraints, though PC–MEMS (§4) may provide the necessary breakthrough. However, power and mass constraints are likely to limit the bandwidth of electronic sensing and control systems on these lightweight platforms.

Acknowledging these limitations, research has been conducted into 'time-averaged' wing control. This strategy seeks to control average, rather than instantaneous, forces and torques by applying kinematic wing trajectory corrections on timescales longer than a wing flapping period [9]. The assumption that active control will not be attempted at short (sub-wingbeat) timescales raises the question of the ideal short timescale behavior of a wing flapping mechanism. Conventional kinematic control approaches tacitly assume that rigid specification of wing trajectory is a preferred short timescale behavior. The focus on wing kinematics in FWMAVs design likely results from both a similar focus in related aerodynamics models and the relative ease

of measuring kinematics over flight forces and torques.

However, the specific wing trajectory executed is not fundamentally important to an FWMAV. Rather, an active flight control system treats wing trajectory as merely a tool to generate desired reaction forces and torques on the airframe. Ideally, the wings should execute whatever trajectories are necessary to realize these desired forces and torques.[1] A drivetrain that passively regulates these forces and torques at a short timescale may simplify a longer timescale flight controller.

This alternative behavior is conjectured to produce systems that reject short timescale disturbances passively, alleviating requirements on active control systems. It is also expected to compensate for a subset of fabrication asymmetries, passively realizing the necessary adjustments to wing trajectory. This feature is an attractive one, since fabrication variation is a major concern for devices manufactured at the millimeter scale, though one somewhat mitigated by the new PC–MEMS process (§4).

Under the PARITy methodology, long timescale control is achieved not by altering the wing trajectories directly, but by modulating the dynamics of the short timescale passive system. In the context of PARITy based FWMAV designs, control inputs would perturb the set point of short timescale system dynamics. This control idea appears in helicopters incorporating a Hiller stabilizer, wherein the pilot's control input, instead of directly driving rotor blade pitch, perturbs the stabilizer mechanism that regulates it. Another example appears in constant speed propellers: in a common design, the pilot tunes propeller speed by altering a spring tension within a centrifugal governor that regulates propeller blade pitch.

[1] The specific trajectory may be important for efficiency concerns, but is irrelevant for the purposes of stabilizing and controlling the airframe.

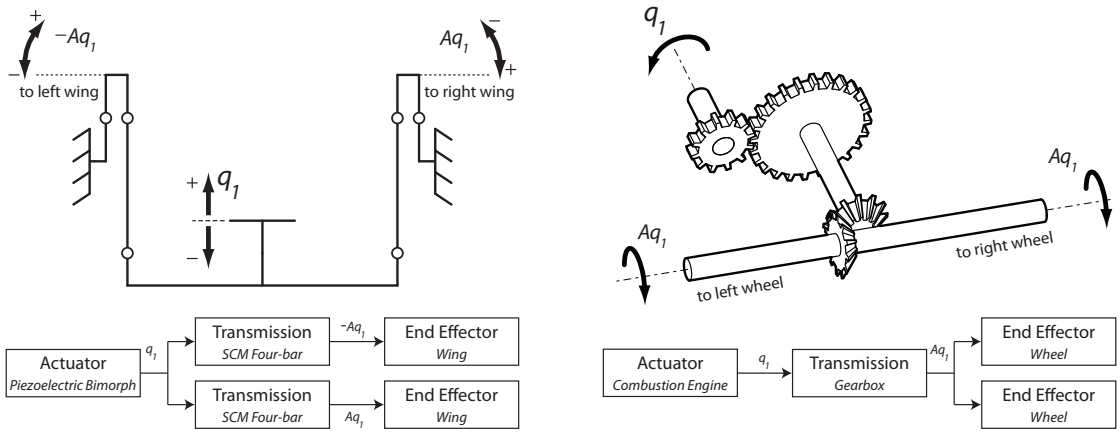

Figure 2.5: (left) Kinematic diagram and representative block diagram for the simple HMF transmission. (right) A simplified automobile drivetrain, analogous to the HMF transmission.

In the context of FWMAVs, the 'Drag PARITy' drivetrain (§2.4) passively balances body roll torques imparted by each wing. However, actuation of an active control input could bias system dynamics such that the magnitude ratio of roll torques imparted by the wings is passively regulated to a value other than one, similar to moving the pivot point of a whippletree. In such a manner, local passive regulation may enable direct active force and torque control at long timescales, simplifying the control problem for mass-limited FWMAVs.

2.3 Important mechanisms

Mechanically intelligent systems rely on sophisticated mechanisms. This section will cover the kinematic details of several important mechanisms. First, §2.3.1 will cover the non-mechanically intelligent transmission mechanism of the HMF to serve

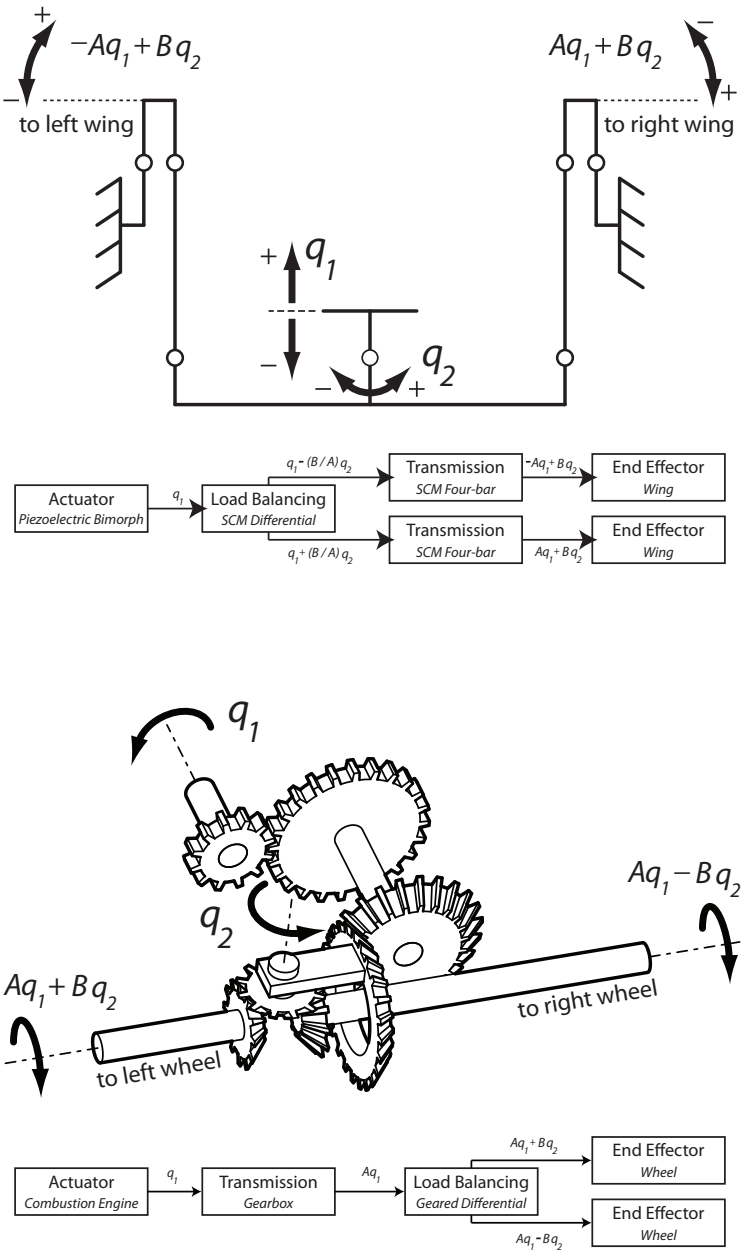

Figure 2.6: (top) Kinematic diagram and representative block diagram for the PARITy drivetrain. (bot) A classic automobile drivetrain, analogous to the PARITy design, incorporating a transmission and a differential.

as a baseline. A modified, mechanically intelligent version known as the "Drag PARITy" transmission is covered in §2.3.2. Finally, §2.3.3 describes a spherical shoulder mechanism developed for advanced PARITy designs and underlies the dynamic model presented in §3.2.

2.3.1 A symmetric four-bar transmission

Referring to Figure 2.5, the standard HMF transmission consists of two symmetric four-bar linkages. Each side of the airframe serves as a ground, and four links from each side extend inward to a shared central link that is driven by the actuator. The wings mount to links adjacent to the airframe ground on each side. Using a typical linkage design, a 400μm displacement of the central link results in a 60° wing stroke. The link lengths can be altered to impact both the average transmission ratio and linearity over the flapping stroke.

The actuator constrains the central link to undergo purely translational motion; this single degree of freedom can be expressed either as an input actuator displacement q_1 or as an output wing stroke angle ϕ. The HMF transmission is identical to the two degree of freedom transmission of Figure 2.7 with degree of freedom q_2 constrained to zero. Figure 2.7b-c depicts the single degree of freedom symmetric flapping motion, while Figure 2.7a defines links L_1, L_2, L_3, and L_4.

2.3.2 A 2-DOF transmission

The 2-DOF transmission illustrated in Figure 2.7 will be called the "Drag PARITy" transmission, and is the core mechanism enabling roll torque regulation. The

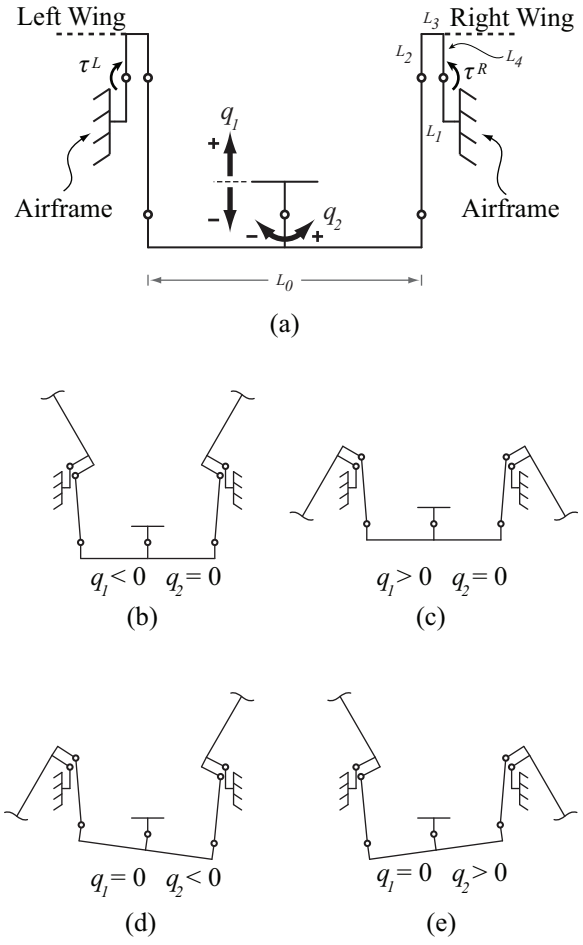

Figure 2.7: (a) Planar kinematics of the two degree of freedom drag PARITy transmission. Holding $q_2 = 0$ and allowing q_1 to oscillate between (b) negative and (c) positive values produces a symmetric flapping motion. Holding $q_1 = 0$ and allowing q_2 to take (d) negative and (e) positive values produces a differential flapping motion, coupling the upstroke of one wing with the downstroke of the other.

transmission has a single actuated input q_1 and dual outputs driving the stroke angles of each wing. The right wing stroke angle ϕ^R is illustrated in Figure 2.11c, while the left wing stroke angle ϕ^L (not shown) is the analogous angle on the opposing wing. The transmission mechanism has two degrees of freedom; referring to Figure 2.11b, q_1 is actuated and allows power to be injected into the system, while q_2 is passively determined.

The two degrees of freedom of the Drag PARITy transmission are illustrated in Figure 2.7. The actuator output drives the transmission input q_1 in an oscillatory trajectory, while q_2 describes the rotation of the 'whippletree' link L_0. Figures 2.7b and 2.7c demonstrate the symmetric wingstrokes achieved by fixing $q_2 = 0$. Rotation of the balance beam through an angle q_2 couples the upstroke of one wing to the downstroke of the other, a feature central to the passive torque balancing properties of the Drag PARITy transmission. An invertible kinematic mapping relates q_1 and q_2 to the wing stroke angles ϕ^L and ϕ^R; the latter pair of coordinates are used in the theoretical model.

2.3.3 A spherical shoulder

Kinematics

The spherical linkage consists of six links connected by six revolute joints, with all joints intersecting in a single spherical center. Every link has an associated coordinate frame; the spherical center is the origin of all coordinate frames, and in the neutral configuration all frames are coincident. Link 1 is the mechanism ground.

The six vectors $\hat{s}_1, \hat{s}_2, \ldots, \hat{s}_6$ represent the rotational axes of the six revolute joints.

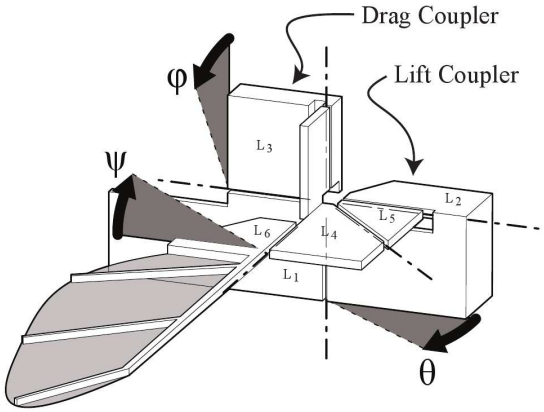

Figure 2.8: Diagram of linkage kinematics.

The rotational deflections of the revolute joints are described by the six joint angles $\gamma_1, \ldots, \gamma_6$. Three joint angles form the three element configuration vector $\vec{p}$ describing the configuration of the linkage:

$$\begin{bmatrix} \gamma_1 \\ \gamma_4 \\ \gamma_6 \end{bmatrix} \equiv \begin{bmatrix} \phi \\ \theta \\ \psi \end{bmatrix} \equiv \vec{p} \tag{2.1}$$

The remaining joint angles are fully determined by specifying the three elements of $\vec{p}$. Note that each joint vector has constant coordinates in the coordinate frames of the two links it joins. For example, joint $\hat{s}_3$ connects links 4 and 5, so $\hat{s}_3^4$ is constant and identical to $\hat{s}_3^5$, irrespective of linkage configuration.

Two parallel kinematic chains extend from the ground link L_1 to link L_4. The first chain extends from L_1 to L_3 to L_4, through joints $\hat{s}_1$ and $\hat{s}_5$. The second chain extends from L_1 to L_2 to L_5 to L_4, through joints $\hat{s}_4$, $\hat{s}_2$, and $\hat{s}_3$. A final joint $\hat{s}_6$

connects link L_6 serially to L_4.

$$\mathbf{R}_3^1 = \mathbf{R}_x(\phi) \tag{2.2}$$

$$\mathbf{R}_2^1 = \mathbf{R}_y(\theta) \tag{2.3}$$

$$\mathbf{R}_6^4 = \mathbf{R}_z(\psi) \tag{2.4}$$

$$\mathbf{R}_4^3 = \mathbf{R}_y(\gamma_5(\phi,\theta)) \tag{2.5}$$

$$\mathbf{R}_5^2 = \mathbf{R}_{\hat{s}_2^2}(\gamma_2(\phi,\theta)) \tag{2.6}$$

Based on manufacturing consideration, the linkage has been parameterized by two angles, α_2 and α_3, with $0 \leq \alpha_3 < \alpha_2 \leq \pi$. These parameters describe the location of joints 2 and 3, assumed to be in the xz planes of their associated links:

$$\hat{s}_2^5 = \hat{s}_2^2 \equiv \begin{bmatrix} s_{\alpha_2} \\ 0 \\ c_{\alpha_2} \end{bmatrix} \; ; \; \hat{s}_3^5 = \hat{s}_3^4 \equiv \begin{bmatrix} s_{\alpha_3} \\ 0 \\ c_{\alpha_3} \end{bmatrix} \tag{2.7}$$

The notation s_x and c_x is shorthand for $\sin x$ and $\cos x$, respectively. Refer to Appendix A.1 for further clarification of nomenclature.

Forward kinematics

The joint angles γ_2 and γ_5 are functions of two of the three configuration angles and must satisfy the following constraint, arising from the notion that both parallel chains must map joint $\hat{s}_3$ to consistent ground frame coordinates:

$$\mathbf{R}_3^1 \mathbf{R}_4^3 \hat{s}_3^4 = \mathbf{R}_2^1 \mathbf{R}_5^2 \hat{s}_3^5 \tag{2.8}$$

Equivalently, using (2.2)-(2.6), (2.8) can be written:

$$\mathbf{R}_x(\phi)\, \mathbf{R}_y(\gamma_5(\phi,\theta))\, \hat{s}_3^4 = \mathbf{R}_y(\theta)\, \mathbf{R}_{\hat{s}_2^2}(\gamma_2(\phi,\theta))\, \hat{s}_3^5 \tag{2.9}$$

$$\begin{bmatrix} s_{\theta+\alpha_2} & -c_\phi c_{\theta+\alpha_2} \\ c_\phi c_{\theta+\alpha_2} & s_{\theta+\alpha_2} \end{bmatrix} \begin{bmatrix} c_{\gamma_5} \\ s_{\gamma_5} \end{bmatrix} = \begin{bmatrix} s_{\alpha_2} s_{\alpha_3}^2 + c_{\alpha_2} s_{\alpha_3} c_{\alpha_3} + (s_{\alpha_2}(1 - s_{\alpha_3}^2) - c_{\alpha_2} s_{\alpha_3} c_{\alpha_3}) c_{\gamma_3} \\ s_{\alpha_2} s_{\alpha_3} c_{\alpha_3} + c_{\alpha_2} c_{\alpha_3}^2 + (-s_{\alpha_2} s_{\alpha_3} c_{\alpha_3} + c_{\alpha_2}(1 - c_{\alpha_3}^2)) c_{\gamma_3} \end{bmatrix} \tag{2.12}$$

$$\begin{bmatrix} c_\phi & s_{\theta+\alpha_2} s_\phi \\ s_{\theta+\alpha_2} s_\phi & -c_\phi \end{bmatrix} \begin{bmatrix} c_{\gamma_2} \\ s_{\gamma_2} \end{bmatrix} = \begin{bmatrix} c_{\gamma_3} \\ (s_{\alpha_2} s_{\alpha_3} + c_{\alpha_2} c_{\alpha_3}) s_{\gamma_3} \end{bmatrix} \tag{2.13}$$

$$s_{\gamma_3} = \frac{c_{\theta+\alpha_2} s_\phi}{c_{\alpha_2} s_{\alpha_3} - s_{\alpha_2} c_{\alpha_3}} \tag{2.14}$$

Satisfying this constraint leads to the system of five equations (2.12)-(2.14). Equation (2.14) leads to the following condition establishing joint limits on the inputs ϕ and θ:

$$\left| \frac{c_{\theta+\alpha_2} s_\phi}{c_{\alpha_2} s_{\alpha_3} - s_{\alpha_2} c_{\alpha_3}} \right| \leq 1 \tag{2.10}$$

Assuming this condition is satisfied, (2.14) admits two possibilities for γ_3. In practice, however, input angles ϕ and θ are often limited to the domain $(-\frac{\pi}{2}, \frac{\pi}{2}]$, in which case the unique solution for γ_3 in the same domain can be used:

$$\gamma_3 = \arcsin\left(\frac{c_{\theta+\alpha_2} s_\phi}{c_{\alpha_2} s_{\alpha_3} - s_{\alpha_2} c_{\alpha_3}} \right) \tag{2.11}$$

Once γ_3 is known, (2.12) and (2.13) reduce to simple linear equations in c_{γ_5}, s_{γ_5}, c_{γ_2}, and s_{γ_2}, allowing straightforward determination of γ_2 and γ_5 to satisfy the constraint.

Determination of γ_2 and γ_5 allows use of equations (2.2)-(2.6) to establish the rotation matrix representing each link frame with respect to the mechanism ground, fully describing the kinematic configuration of the linkage.

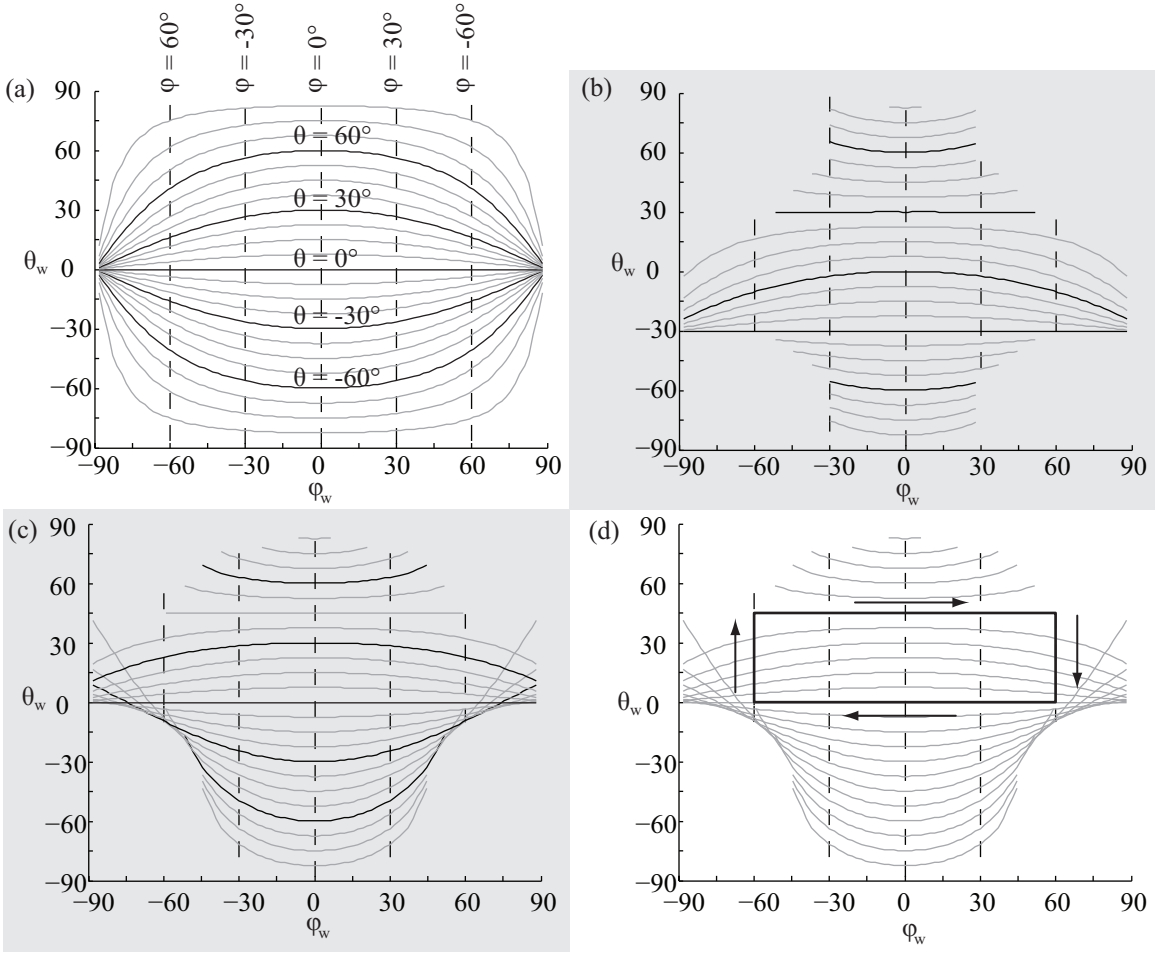

Figure 2.9: Transmission mapping for (a) $\alpha_2 = 90°$,$\alpha_3 = 0°$, (b) $\alpha_2 = 90°$,$\alpha_3 = 45°$, and (c) $\alpha_2 = 120°$,$\alpha_3 = 60°$.

Transmission characteristics

In all cases, input angles ϕ and ψ map directly to output 'wing' angles ϕ_w and ψ_w. Input angle θ, however, maps to output angle θ_w coupled with ϕ: $\theta_w = \theta_w(\phi, \theta)$. The joint is always nearly decoupled close to the origin, that is, $\theta_w(0, \epsilon) \approx \epsilon$. However, the behavior of this mapping is highly dependent on the configuration parameters α_2 and α_3. Setting $\alpha_2 = 90°$ and $\alpha_3 = 0°$ results in a joint of excellent performance, with $\partial\theta_w/\partial\theta \approx 1$ and $\partial\theta_w/\partial\phi \approx 0$ over a wide range of the configuration space (Figure 2.9a).

However, other configurations can be preferable in situations where the output trajectory is known a priori, as often occurs in driving leg motion for ambulatory robots. For example, consider a case where ϕ_w corresponds to leg stroke and θ_w corresponds to leg lift. Suppose further that walking with this leg entails tracing the perimeter of a box in configuration space between $\phi_w = \pm 60°$ and $\theta_w = 0°, 45°$. Then, setting $\alpha_2 = 90°$ and $\alpha_3 = 45°$ produces a perfectly decoupled trajectory, as shown in Figure 2.9d. However, deviating from this specific trajectory can produce undesirable behavior.

2.4 Drag PARITy

2.4.1 Regulating roll torques

The HMF transmission is a fully actuated transmission for driving two flapping wings from a single reciprocating actuator. It is a 1-DOF mechanism (see §2.3.1): the motion of the single actuator drives symmetric stroke angle trajectories. Knowl-

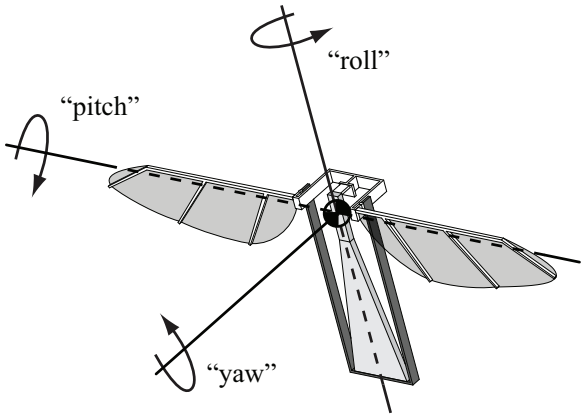

Figure 2.10: Definition of roll, pitch, and yaw in the body frame.

edge of the actuator displacement allows direct calculation of each wing stroke angle, commensurate with the methodology of driving wing trajectory.

By contrast, the Drag PARITy transmission is an underactuated mechanism for driving two flapping wings from a single actuator. It is a 2-DOF mechanism driven by a single actuator; rather than fully determining wing stroke angles, the displacement of the actuator only determines the average wing stroke angle. Motion of the actuator produces a symmetric wing stroke motion, but the wings are free to stroke antisymmetrically. The difference between the left and right wing stroke angles is a degree of freedom not coupled to the drive actuator, and is instead determined purely dynamically during operation.

Underactuation in a flapping wing mechanism is not itself novel: the HMF transmission outputs typically mount each wing through a compliant span-aligned wing hinge, creating a singly actuated 3-DOF system [40]. Wing rotation during the stroke is realized passively, greatly reducing mechanical complexity compared to fully actuated designs such as the Berkeley MFI [13]. However, Drag PARITy demonstrates

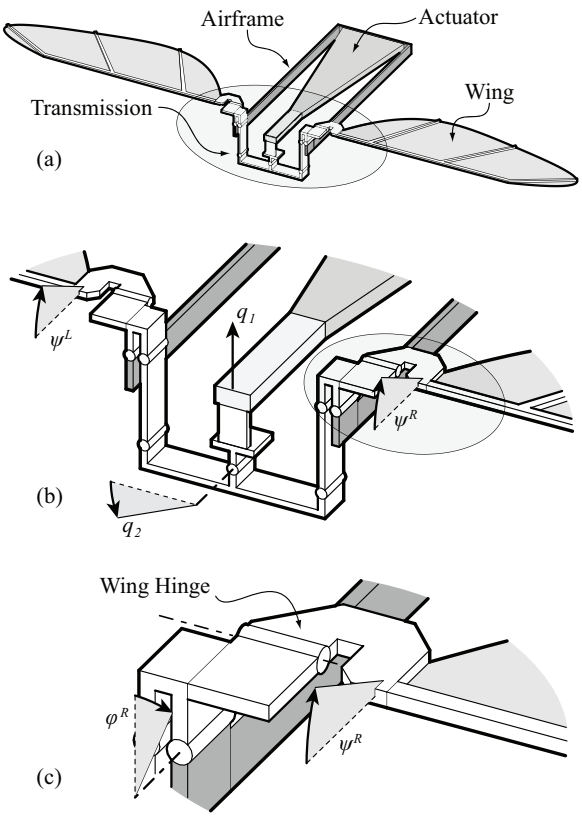

Figure 2.11: (a) Diagram of an FWMAV design incorporating a Drag PARITy transmission. (b) The four degrees of freedom q_1, q_2, ψ^L, and ψ^R with respect to airframe ground. (c) A view of the shoulder clarifying rotation angle ψ^R. Right wing stroke angle ϕ^R can be determined from q_1 and q_2, as can ϕ^L of the left wing (not shown).

that the benefits of underactuation extend beyond simple reduction of mechanical complexity.

In Drag PARITy, a degree of freedom has been added intentionally to create a mechanically regulated system. During operation, the flapping of each wing exerts a roll reaction torque on the airframe. The unactuated degree of freedom causes the system to alter its behavior in response to imbalanced roll reaction torques from the wings. Antisymmetric wing stroke motion passively decreases the stroke velocity of the wing delivering more torque and increases the stroke velocity of the one delivering less, tending to reduce the imbalance in roll torques. Without intervention from an active controller, wing stroke velocities modulate dynamically to regulate total body roll torque.

The operating principle of Drag PARITy is analogous to that of an automobile differential, described in §2.1.4. Both drive symmetric output motions from the actuation source; an automobile drives symmetric wheel rotation with its engine while an FWMAV using Drag PARITy drives symmetric wingstrokes with its piezoelectric actuator. Both systems allow antisymmetric motion to occur freely during operation. Such an underactuated mechanism drives outputs so as to regulate output torques to be equal, allowing each output to passively execute potentially complex relative trajectories.

The passive torque balancing mechanism in Drag PARITy can be conceptually understood by considering the complete FWMAV system in operation. When the actuator is driven, the left and right wings execute a periodic flapping motion, exerting roll-aligned torques τ^L and τ^R, respectively, on the transmission outputs (see

Figure 2.7). These torques arise from both inertial and aerodynamic effects, and the difference $\tau^L - \tau^R$ comprises the net roll torque experienced by the FWMAV airframe during flight. These torques are also transmitted through the kinematic structure, appearing on the central whippletree (link L_0 of Figure 2.7) after magnification by the transmission ratios $\frac{\partial \phi^L}{\partial q_2}$ and $\frac{\partial \phi^R}{\partial q_2}$ for the torques from the left and right wings, respectively.

In a completely symmetric system, these torques cancel exactly and the whippletree undergoes no rotation. However, should an asymmetry arise, a net torque will appear on the whippletree, causing it to rotate. This rotation alters the stroke velocities of each wing; if the torque from a wing is too low its stroke velocity increases in comparison to the stroke velocity of the opposing wing. This passive modulation of wing stroke trajectories tends towards cancellation of any asymmetric roll torques experienced by the airframe. Chapter 3 describes two experiments demonstrating and modeling operation and torque balancing within the Drag PARITy transmission.

2.4.2 Controlling Drag PARITy

Under the PARITy methodology, control inputs do not directly impact wing kinematics, but instead alter the dynamics of the mechanically regulated system. An embodiment of such a control technique can be found in whippletrees and is readily adaptable to Drag PARITy. Whippletrees with a central pivot divide a force on the pivot equally to the two outputs. Moving the central pivot still produces a mechanically regulated system, but now the pivot force is divided asymmetrically to each whippletree output. For example, if the distance from each output to the pivot has

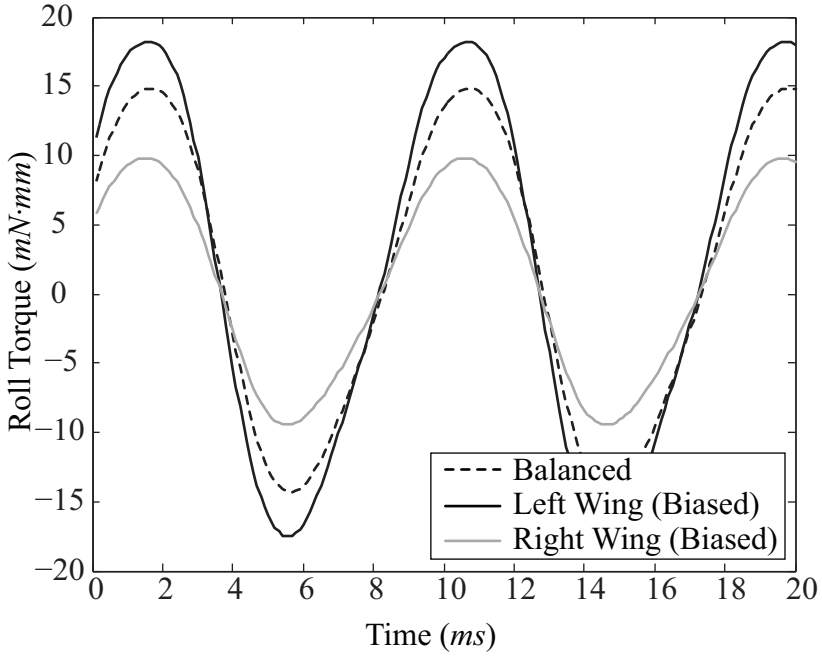

Figure 2.12: Simulation results showing roll torques from a biased Drag PARITy drivetrain compared to the baseline balanced drivetrain. This demonstrates PARITy flight control by biasing a mechanically regulated system, in this case such that the left wing delivers twice the roll torque of the right wing.

the ratio 2:1, then the resulting division of force from the pivot will be mechanically regulated to the ratio 1:2.

This control scheme has been explored in theory using the numerical model presented in §3.2. Figure 2.12 shows a simulation result of a Drag PARITy drivetrain of typical parameters compared to the same drivetrain with a biased pivot point. The pivot point location is such that the left arm of the whippletree (link L_0 of Figure 2.7) is half of the length of the right arm, causing the roll torque experienced by the airframe from the left wing to be double that experienced from the right wing. Mechanical regulation is still in effect, but the set point has been biased to produce

an imbalanced roll torque.

While this scheme succeeds in providing a control input to Drag PARITy, it has several problems. Firstly, producing a constant roll torque imbalance does not lead to an average roll torque on the airframe during operation. Though the torque from one wing will always be larger than the other, the reciprocating nature of the roll torque means that an imbalance will produce a zero-averaged roll oscillation. Combination with a split-cycle control strategy is one avenue to produce a net roll [39]. Secondly, the problem of designing a mechanism to implement the moving-pivot behavior has not yet been solved.

2.5 Lift PARITy and Dual PARITy

While the Drag PARITy transmission focuses on regulating roll torques, more sophisticated PARITy mechanisms can be expected to mechanically regulate larger subsets of the forces and torques experienced during flight. This section describes some initial attempts to demonstrate mechanisms capable of regulating torques other than roll.

2.5.1 Regulating lift-aligned torques

Lift PARITy and Dual PARITy are designs intended to take the PARITy concept beyond regulation of roll torques to regulation of other torques experienced during flight, namely, the torque resulting from imbalanced lift. While this torque is the primary non-inertial component of airframe yaw, its axis follows the wing and is constantly in motion in the body frame. This presents a difficulty in mapping this

behavior into the body frame; this difficulty is not present in Drag PARITy as aerodynamic drag torque and body roll torque are always aligned.

Lift PARITy contains a lift balancing apparatus driven with the standard HMF transmission, while Dual PARITy combines the Lift PARITy and Drag PARITy mechanisms in an attempt to regulate both. Though the effort to mechanically regulate yaw torques has not yet reached a successful conclusion, it warrants description as it both has impacted the theoretical and experimental results reported here and will aid future investigation of the PARITy concept for FWMAVs.

While the Drag PARITy mechanism modulates stroke velocity in response to imbalanced roll torques, the core Lift PARITy mechanism modulates wing angle of attack in response to imbalanced lift torque. There are several parallels between this mechanism and the Bell stabilizer bar for helicopters described in §2.1.3:

1. The error signal: the Bell stabilizer detects an attitude error, while Lift PARITy detects an attitude acceleration error.

2. The correction signal: both systems modulate airfoil angle of attack to correct the error.

Detection of lift-aligned torque error motivated the development of the spherical shoulder described in §2.3.3. Referring to Figure 2.8, the spherical shoulder drives the wing through a 2-DOF parallel linkage mapping wing stroke and deviation to two decoupled ground referenced links called the *drag coupler* and *lift coupler*, respectively. At any point in the wing stroke, the drag torque acts along the wing stroke axis, while lift torques act along the deviation axis. Thus, drag-aligned torques on the wing appear as torques on the drag coupler linkage, which can be driven by Drag PARITy,

while lift-aligned torques appear as torques on the lift coupler linkage. The Lift PARITy mechanism connects the lift couplers from each wing, in effect using deviation angle as a mechanism to sense an imbalance in lift-aligned torque experienced by the wings.

The correction to imbalanced lift-aligned torque relies on altering angle of attack with a tunable wing hinge. The wing angle of attack modulates passively, dependent on a compliant wing hinge; typically, a stiffer wing hinge results is less wing rotation and vice versa. The tunable wing hinge is a compliant mechanism whose stiffness along the wing rotation axis is dependent on wing deviation: higher deviation results in a stiffer wing hinge. The basics of a control loop are present: a lift imbalance creates a deviation angle, which, through the tunable wing hinge, alters wing angle of attack so as to reduce the imbalance.

A numerical simulation model (§3.2) allows exploration of this candidate mechanically regulated system. In practice, the high level operational theory presented in this section has many problems.

2.5.2 Unsolved issues

The proportionality of stroke plane deviation and yaw torque error requires a vanishingly small wing inertia as measured at the shoulder hinge about an axis perpendicular to the wing surface. Unfortunately, the largest principle inertia of the airfoil is a lower bound for this inertia, and manufacturing concerns restrict excessive reduction. Grossly simplified, a yaw torque error creates a deviation acceleration, which is integrated twice to produce a deviation angle. This creates a large lag be-

tween the appearance of an imbalance and the resulting error signal.

In addition to a lagging error signal, the correction similarly experiences a lag. Altering wing angle of attack occurs by modulating the wing hinge torque and accelerating the wing about the rotational axis. Similar to the error mechanism, two integrations produce a lag in response.

Another critical problem is backdriving, or more broadly, coupling of all parts of the system. Dividing a system into separate parts such as an error sensor or a correction mechanism implies that connecting these parts does not alter their individual behavior. In electronics, this concept is expressed in terms of input and output impedance; creating high input impedance and low output impedance often implies a form of gain. In the context of Lift PARITy, creating a system that alters wing rotation in response to lift-aligned torque also creates a system that alters wing deviation in response to rotation-aligned torque. While a helicopter blade can be designed to have no rotation-aligned torque during operation, such a torque is necessary for passive wing rotation. Lift PARITy and Dual PARITy may have more success paired with designs that drive wing rotation kinematically.

2.6 Stability

An underactuated system such as Drag PARITy will not be useful unless it is capable of operating stably. This section creates a simplified model of Drag PARITy and proves that all designs exhibit stable operation under normal conditions.

The question of stability is confounded by kinematic and dynamic nonlinearities arising from linkage designs and aerodynamics. Applying various simplifying approx-

imations, however, can reduce the problem into one that is analytically tractable. Consider the simplest PARITy system, the Drag PARITy with fixed wings (configuration #4 in Table 3.1).

2.6.1 Linearized equations for flapping

This system has two kinematic degrees of freedom, expressible either as wing angles (ϕ_1 and ϕ_2) or in actuator displacement and transmission rotation (q_1 and q_2, respectively). A quantity takes a q or ϕ as a superscript to designate the coordinate system when necessary. A transmission ratio T, assumed to be constant, and a whippletree length L result in a linear relationship between these coordinates:

$$\begin{pmatrix} \phi_1 \\ \phi_2 \end{pmatrix} = \begin{pmatrix} -T & TL \\ -T & -TL \end{pmatrix} \begin{pmatrix} q_1 \\ q_2 \end{pmatrix} \equiv \mathbf{T}_q^\phi \begin{pmatrix} q_1 \\ q_2 \end{pmatrix} \tag{2.15}$$

Using an Euler-Lagrange approach, the kinetic energy U and the potential energy V of the system are:

$$U = \frac{1}{2} I \dot{\phi}_1^2 + \frac{1}{2} I \dot{\phi}_2^2 = \frac{1}{2} I T^2 (\dot{q}_1^2 + L^2 \dot{q}_2^2)$$
$$V = \frac{1}{2} K_1 q_1^2 + \frac{1}{2} K_2 q_2^2$$

The resulting equations of motion for the non-dissipative system are decoupled in q_1 and q_2:

$$2IT^2 \ddot{q}_1 + K_1 q_1 = \tau_1^q$$

$$2IT^2 L^2 \ddot{q}_2 + K_2 q_2 = \tau_2^q$$

This model ignores phenomena such as friction and joint hysteresis, accounting only for the two primary sources of generalized torques τ_1 and τ_2: the actuator driving

force F_A and aerodynamic drag on the wings. Simplifying the sophisticated blade-element aerodynamic model given in §3.2.4, wing drag has the opposite sign of stroke velocity and magnitude proportional to its square (with proportionality constant Ω):

$$\begin{pmatrix} \tau^{\phi}_{1,aero} \\ \tau^{\phi}_{2,aero} \end{pmatrix} \equiv \vec{\tau}^{\phi}_{aero} = \begin{pmatrix} -\Omega\dot{\phi}_1^2 \mathrm{sgn}(\dot{\phi}_1) \\ -\Omega\dot{\phi}_2^2 \mathrm{sgn}(\dot{\phi}_2) \end{pmatrix} \tag{2.16}$$

A Jacobian converts to q coordinates:

$$\begin{aligned} \vec{\tau}^{q}_{aero} &= \left(\mathbf{T}^{\phi}_{q}\right)^{T} \vec{\tau}^{\phi}_{aero} \\ &= \Omega T \begin{pmatrix} \dot{\phi}_1^2 \mathrm{sgn}(\dot{\phi}_1) + \dot{\phi}_2^2 \mathrm{sgn}(\dot{\phi}_2) \\ -L\dot{\phi}_1^2 \mathrm{sgn}(\dot{\phi}_1) + L\dot{\phi}_2^2 \mathrm{sgn}(\dot{\phi}_2) \end{pmatrix} \end{aligned}$$

Assuming that $L\dot{q}_2 << \dot{q}_1$ and noting that the drag torque is zero to first order whenever the signum function changes sign, we replace both $\mathrm{sgn}(\dot{\phi}_1)$ and $\mathrm{sgn}(\dot{\phi}_2)$ with $-\mathrm{sgn}(\dot{q}_1)$, resulting in the following expression for the aerodynamic torque:

$$\vec{\tau}^{q}_{aero} = -2\Omega T^2 \mathrm{sgn}(\dot{q}_1) \begin{pmatrix} \dot{q}_1^2 + L^2\dot{q}_2^2 \\ 2L^2\dot{q}_1\dot{q}_2 \end{pmatrix} \tag{2.17}$$

The final equations of motion are:

$$2IT^2\ddot{q}_1 + K_1 q_1 = -2\Omega T^2 \mathrm{sgn}(\dot{q}_1)(\dot{q}_1^2 + L^2\dot{q}_2^2) + F_A \tag{2.18}$$

$$2IT^2L^2\ddot{q}_2 + K_2 q_2 = -4\Omega T^2 L^2 \mathrm{sgn}(\dot{q}_1)\dot{q}_1\dot{q}_2 \tag{2.19}$$

Using a tailored driving force, it is straightforward to determine a sinusoidal flapping solution to this system of equations with amplitude A and frequency ω_0:

$$\tilde{q}_1(t) = A\sin(\omega_0 t) \tag{2.20}$$

$$\tilde{q}_2(t) = 0 \tag{2.21}$$

$$\tilde{F}_A(t) = A(K_1 - 2IT^2\omega_0^2)\sin\omega_0 t + 2\Omega T^2 A^2 \omega_0^2 \mathrm{sgn}(\cos\omega_0 t)\cos^2\omega_0 t \tag{2.22}$$

Define the non-dimensional parameters β_0, κ_1, κ_2, and η as follows:

$$\beta_0 \equiv \frac{2\Omega A}{I}$$
$$\kappa_1 \equiv \frac{K_1}{2IT^2\omega_0^2}$$
$$\kappa_2 \equiv \frac{K_2}{2IT^2L^2\omega_0^2}$$
$$\eta \equiv \frac{F_A - \tilde{F}_A}{2IT\omega_0}$$

Linearizing (2.18)-(2.19) about this solution and using the non-dimensional variables $Q_1 \equiv Tq_1$, $Q_2 \equiv q_2$, and $\tau \equiv \omega_0 t$, we arrive at the equations of motion:

$$\ddot{Q}_1 + \beta_0 \left|\cos\tau\right| \dot{Q}_1 + \kappa_1 Q_1 = \eta \tag{2.23}$$

$$\ddot{Q}_2 + \beta_0 \left|\cos\tau\right| \dot{Q}_2 + \kappa_2 Q_1 = 0 \tag{2.24}$$

2.6.2 Floquet analysis

Motivated by the equations of motion linearized around sinusoidal flapping, we investigate a differential equation for $x(t)$ of the following form:

$$\ddot{x} + \beta_0 \left|\cos t\right| \dot{x} + \kappa x = 0 \tag{2.25}$$

This equation is a time-varying periodic linear equation with period $T = \pi$. It is a modified form of the Hill equation, as can be seen by applying the following coordinate transformation:

$$x(t) = y(t) \exp\left(-\frac{1}{2}\beta_0 \int_{t_0}^{t} \left|\cos\tau\right| \mathrm{d}\tau\right) \tag{2.26}$$

The differential equation for $y(t)$ becomes:

$$\ddot{y} + \left(\frac{1}{2}\beta_0^2 \cos^2 t - \frac{1}{2}\beta_0 \frac{\mathrm{d}}{\mathrm{d}t}\left|\cos t\right| + \kappa\right) y = 0 \tag{2.27}$$

This differential equation is in the classic Hill form $\ddot{y} + f(t)y = 0$ with $f(t)$ periodic. However, in this transformed equation, $f(t)$ includes periodic δ-functions due to the differentiated absolute value, so the simpler original form will instead be directly analyzed.

Define an **A**-matrix as follows:

$$\mathbf{A}(t) \equiv \begin{pmatrix} 0 & 1 \\ -\kappa & -\beta_0 \left|\cos t\right| \end{pmatrix} \tag{2.28}$$

Defining $\vec{x} \equiv \left(\begin{smallmatrix} x \\ \dot{x} \end{smallmatrix}\right)$, we can write (2.25) in first order matrix form:

$$\dot{\vec{x}}(t) = \mathbf{A}(t)\vec{x}(t) \tag{2.29}$$

Define $\mathbf{\Pi}(t, t_0)$ as the matrix solution to this equation with initial condition $\mathbf{\Pi}(t_0, t_0) = \mathbf{I}$. The monodromy matrix $\mathbf{M}(t_0)$ is defined as the matrix solution over one period:

$$\mathbf{M}(t_0) \equiv \mathbf{\Pi}(t_0 + T, t_0) \tag{2.30}$$

Note that $\mathbf{M}$ is periodic with period T. Liouville's formula assures that the determinant of $\mathbf{M}$ is non-zero and positive, allowing $\mathbf{M}$ to be expressed as the exponential of another matrix $\mathbf{Q}$ (also periodic with period T):

$$\mathbf{M}(t_0) = \exp\left(T\mathbf{Q}(t_0)\right) \tag{2.31}$$

Floquet's theorem states that the solution matrix $\mathbf{\Pi}(t, t_0) = \mathbf{P}(t, t_0) \exp\left((t - t_0)\mathbf{Q}(t_0)\right)$ where $\mathbf{P}(t, t_0)$ has period T and $\mathbf{P}(t_0, t_0) = \mathbf{I}$. Furthermore, the transformation $\vec{y}(t) = P(t, t_0)^{-1}\vec{x}(t)$ results in a constant coefficient differential equation:

$$\dot{\vec{y}}(t) = \mathbf{Q}(t_0)\vec{y}(t) \tag{2.32}$$

It can now be easily seen that a periodic system is stable if all eigenvalues of $\mathbf{Q}(t_0)$ (the Floquet exponents γ_j) satisfy $\mathrm{Re}(\gamma_j) \leq 0$ and asymptotically stable if $\mathrm{Re}(\gamma_j) < 0$. Since the eigenvalues of $\mathbf{M}(t_0)$ (the Floquet multipliers ρ_i) are related by $\rho_i = \exp(T\gamma_j)$, a periodic system is stable if all ρ_j satisfy $|\rho_j| \leq 1$ and asymptotically stable if $|\rho_j| < 1$.

Returning to the analysis of equation (2.29), assume $\xi_1(t)$ and $\xi_2(t)$ are two solutions such that:

$$\mathbf{\Pi}(t, t_0) = \begin{pmatrix} \xi_1(t) & \xi_2(t) \\ \xi_1'(t) & \xi_2'(t) \end{pmatrix} \tag{2.33}$$

$$\mathbf{M}(t_0) = \begin{pmatrix} \xi_1(t_0+T) & \xi_2(t_0+T) \\ \xi_1'(t_0+T) & \xi_2'(t_0+T) \end{pmatrix} \tag{2.34}$$

The Floquet exponents satisfy the characteristic equation:

$$\det\left(\mathbf{I}\rho - \mathbf{M}(t_0)\right) = 0 \tag{2.35}$$

If we define $a \equiv \mathrm{tr}(\mathbf{M}(t_0))/2$ and $b \equiv \det(\mathbf{M}(t_0)$, the characteristic equation reduces to:

$$\rho^2 - 2a\rho + b = 0 \tag{2.36}$$

This gives the Floquet multipliers:

$$\rho_{1,2} = a \pm \sqrt{a^2 - b} \tag{2.37}$$

Referring to Fig. 2.13, there are several cases to consider. First, for $b > a^2$, $\rho_{1,2}$ are a complex conjugate pair with magnitude $|\rho_{1,2}| = \sqrt{b}$, and thus the system is unstable for $b > 1$ (Region II in Fig. 2.13) and asymptotically stable for $b < 1$. Second, for

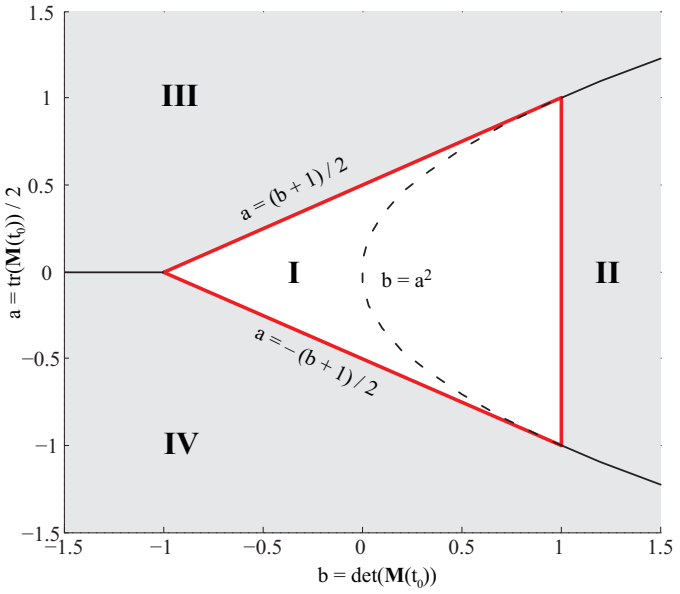

Figure 2.13: System stability in terms of the trace and determinant of the monodromy matrix $\mathbf{M}$. A system in Region I is stable.

$b = a^2$, the monodromy matrix has a double root, so the system is asymptotically stable for $|a| < 1$ and unstable for $|a| \geq 1$. Note that at in the case when $|a| = b = 1$, there exists a solution that grows linearly in t. Finally, for $b < a^2$ there are two real roots. In this case, when $a > 0$, there is at least one unstable root when $a > (b-1)/2$ or $a > 1$ (Region III). Conversely, when $a < 0$ there is at least one unstable root when $a < (-b-1)/2$ or $a < -1$ (Region IV). Region I indicates a stable system with respect to the trace and determinant of the monodromy matrix.

The quantity $b = \det(\mathbf{M}(t_0))$ can be calculated without knowledge of the solution

matrix $\mathbf{\Pi}$. Noting that:

$$\ddot{\xi}_1 + \beta_0 \left|\cos t\right| \dot{\xi}_1 + \kappa \xi_1 = 0 \tag{2.38}$$

$$\ddot{\xi}_2 + \beta_0 \left|\cos t\right| \dot{\xi}_2 + \kappa \xi_2 = 0 \tag{2.39}$$

$$\tag{2.40}$$

Multiplying 2.38 by ξ_2 and 2.39 by ξ_1 and subtracting results in:

$$\xi_1 \ddot{\xi}_2 - \xi_2 \ddot{\xi}_1 = -\beta_0 \left|\cos t\right| \left(\xi_1 \dot{\xi}_2 - \xi_2 \dot{\xi}_1\right) \tag{2.41}$$

$$\frac{\mathrm{d}}{\mathrm{d}t} \det \mathbf{\Pi}(t, t_0) = -\beta_0 \left|\cos t\right| \det \mathbf{\Pi}(t, t_0) \tag{2.42}$$

$$\det \mathbf{\Pi}(t, t_0) = \exp\left[-\beta_0 \int_{t_0}^{t} \left|\cos \tau\right| \mathrm{d}\tau\right] \tag{2.43}$$

$$\det \mathbf{M}(t_0) = \exp\left[-\beta_0 \int_{t_0}^{t_0+\pi} \left|\cos \tau\right| \mathrm{d}\tau\right] \tag{2.44}$$

Thus, b depends only on the damping term:

$$b = e^{-2\beta_0} \tag{2.45}$$

Calculating $a = \mathrm{tr}\mathbf{M}(t_0)$ analytically has proved difficult in general, but the problem is tractable in some limited cases.

2.6.3 Limited analytical Floquet solutions

When $\beta_0 << \kappa$ and $\beta_0 << 1$, the system reduces to a simple harmonic oscillator, which is stable and supports constant amplitude oscillations. The properties of this system are well known and will not be described further here.

The case $\kappa << \beta$ and $\kappa << 1$ is more interesting and is relevant to the Drag PARITy design. It corresponds to an extremely weak restoring spring. In this case,

we have the governing equation:

$$\ddot{x} + \beta_0 \left|\cos t\right| \dot{x} = 0 \tag{2.46}$$

Considering a single period starting at $t_0 = -\pi/2$ allows the absolute value to be dropped:

$$\ddot{x} + (\beta_0 \cos t)\, \dot{x} = 0 \ ; \ t \in \left[-\frac{\pi}{2}, \frac{\pi}{2}\right] \tag{2.47}$$

We find a solution for $\dot{x}$ of the form:

$$\dot{x}(t) = \dot{x}\,(t_0)\, e^{-\beta_0(1+\sin t)} \tag{2.48}$$

Integrating gives:

$$x(t) = x(t_0) + \dot{x}(t_0) \int_{t_0}^{t} e^{-\beta_0(1+\sin\tau)} \mathrm{d}\tau \tag{2.49}$$

By calculating $x(t_0 + T)$ and $\dot{x}(t_0 + T)$ from equations (2.48) and (2.49), we arrive at the monodromy matrix:

$$\mathbf{M}(t_0) = \begin{pmatrix} 1 & \pi e^{-\beta_0} I_0(\beta_0) \\ 0 & e^{-2\beta_0} \end{pmatrix} \tag{2.50}$$

In the preceding expression, $I_\alpha(x)$ refers to the modified Bessel function of the first kind. Due to the periodic nature of the system, equations (2.48)-(2.50) are valid for $t_0 = -\frac{\pi}{2} + n\pi$ and $-\frac{\pi}{2} \leq t \leq \frac{\pi}{2}$ for any integer n, and thus constitute a complete piecewise solution. The Floquet multipliers of $\mathbf{M}(t_0)$ are 1 and $e^{-2\beta_0}$, leading to the following stability criterion:

$$\boxed{\beta_0 \geq 0} \tag{2.51}$$

We can find a matrix $\mathbf{Q}(t_0)$ such that $\mathbf{M} = \log(T\mathbf{Q}(t_0))$:

$$\mathbf{Q}(t_0) = \begin{pmatrix} 0 & -2I_0(\beta_0)\frac{\beta_0 e^{\beta_0}}{1-e^{2\beta_0}} \\ 0 & -\frac{2\beta_0}{\pi} \end{pmatrix} \tag{2.52}$$

A further result of Floquet theory is the existence of a periodic transformation $\mathbf{P}(t, t_0)\vec{y}(t) = \vec{x}(t)$ that converts the time varying linear equation into a constant one $\dot{\vec{y}} = \mathbf{Q}(t_0)\vec{y}$. We see immediately that the solution to $\vec{y}(t)$ will be an exponential decay.

The long term behavior of this system can be found by taking:

$$\mathbf{M}^n = \begin{pmatrix} 1 & \pi e^{-\beta_0} I_0(\beta_0) \frac{1-e^{-2(n+1)\beta_0}}{1-e^{-2\beta_0}} \\ 0 & e^{-2(n+1)\beta_0} \end{pmatrix} \tag{2.53}$$

In the limit as $n \to \infty$, we find:

$$\lim_{t\to\infty} x(t) = x(t_0) + \dot{x}(t_0) \left(I_0(\beta_0) \frac{e^{-\beta_0}}{1 - e^{-2\beta_0}} \right) \tag{2.54}$$

$$\lim_{t\to\infty} \dot{x}(t) = 0 \tag{2.55}$$

The stability criterion (2.51) indicates that under this rudimentary model, all systems with positive aerodynamic damping are stable. This intuitive constraint is respected independent of any design parameters within Drag PARITy, indicating that all implementations will be stable. However, this is a simplest-case model assuming linearity and non-rotating wings; many pitfalls remain for Drag PARITy operating in more complex environments. Real experiments conducted in Chapter 3 as well as results of numerical simulations (see Figure 3.4) provide some empirical support for system stability in specific cases.

2.6.4 A direct solution

R. W. Brockett, in [5], undertakes a more sophisticated stability analysis of equations of the form:

$$\ddot{x} + g(t)\dot{x} + x = 0;\ g(t+T) = g(t) \tag{2.56}$$

Damping $g(t)$ is an arbitrary periodic function. If $|g(t)| \leq 2\delta$, then all solutions are bounded if for some positive integer n:

$$2(n-1)\frac{\pi - \sin^{-1}\sqrt{1-\delta^2}}{\sqrt{1-\delta^2}} \leq T \leq 2n\frac{\sin^{-1}\sqrt{1-\delta^2}}{\sqrt{1-\delta^2}} \tag{2.57}$$

and

$$\int_0^T g(t)\mathrm{d}t \geq 0 \tag{2.58}$$

This criterion applies to a more general set of damping functions, useful for guaranteeing stability but does not guarantee instability if violated. Refer to reference [5] for a more in-depth treatment.

2.7 Disturbance rejection

The focus on regulating torques in PARITy mechanisms gives rise to another benefit, that is, rejection of external disturbances. The wings are large surfaces susceptible to flexing, vibration, and aerodynamic disturbances. While disturbances applied directly to the airframe will be experienced normally, PARITy mechanisms can reduce the impact on the airframe of disturbances applied to the wings.

In the Drag PARITy design, a torsion spring aligned with airframe roll is in series between the wings and the airframe. Any roll disturbance torques appearing on the wings, irrespective of their origin, appear on the airframe only after mediation by this second order linear system. The time-varying damping, however, complicates the analysis.

The desire to acquire straightforward analytical results motivate simplifying the model used in §2.6 even further to use a constant linear drag coefficient β^* to replace

$\beta(t)$. This allows the powerful tools of LTI system theory to be used. Providing credence for this simplification, a similar model has been shown to acceptably reflect device operation [14].

The system is then a classic second order system, with the following transfer function between airfoil roll disturbance torque τ_d and body roll torque τ:

$$\tau = \frac{\kappa_0}{s^2 + \beta^* s + \kappa_0}\tau_d \tag{2.59}$$

For values used in the Drag PARITy design evaluated in Chapter 3, the magnitude of this transfer function reaches 0.003 at 300Hz, meaning a disturbance torque applied to the wings at this frequency appears at 0.3% magnitude on the body.

The Dual PARITy design can be seen as mounting the airframe to the wings with a three-axis gimbal, providing multi-axis torque rejection. However, the rapid motion between wing frame and body frame prevents straightforward characterization and analysis of disturbance rejection in this design.

2.8 Conclusion

An argument for mechanical intelligence is essentially an argument to shift complexity and sophistication away from active control systems and into the mechanics of the device. This premise has one fundamental defect: manufacturing challenges at the millimeter-scale are immense. Though more sophisticated active control systems introduce their own manufacturing challenges in requiring integration of additional sensors and actuators, the advantage of simplifying electronics only to place even harsher performance requirements on an inadequate manufacturing process is not

clear. Manufacturing difficulties have been central both in restricting experimental investigation of mechanically intelligent structures at the millimeter-scale and in limiting adoption of these ideas in a wider variety of devices.

Chapter 4 resolves this defect conclusively by introducing PC–MEMS, a manufacturing process that greatly eases the accurate and repeatable production of millimeter-scale machines. Methods to create accurate mechanisms are fundamental to practical implementation of the mechanically regulated systems discussed in this chapter, and PC–MEMS helps tip the argument between mechanical and electronic complexity in favor of the PARITy methodology.

The next chapter will cover two experiments undertaken to verify performance of the Drag PARITy transmission. They have been undertaken to experimentally verify theoretical claims made in this chapter. However, as they rely on legacy manufacturing techniques, they serve also to motivate and highlight manufacturing improvements embodied by PC–MEMS.

Chapter 3

Experimental Case Studies

3.1 Introduction: experimental methods

This chapter describes two experiments undertaken both to investigate the validity of theoretical results presented in Chapter 2 and to provide a physical embodiment of mechanically intelligent drivetrains for FWMAVs. Both experiments involve the Drag PARITy drivetrain; §3.3 tests a simple system with fixed wing angles of attack, while §3.4 introduces passive wing rotation. Manufacturing difficulties greatly limit the scope of feasible experiments. These difficulties manifest not only in the fabrication of the flapping devices themselves, but also in the construction of sophisticated instrumentation to measure forces and torques. Measuring forces and torques in operating devices requires resolutions on the order of 10μN and 100μN·mm, respectively, at kilohertz bandwidths, performance specifications not currently met in off-the-shelf solutions.

The basic experimental methodology relies on an accurate numerical model (§3.2)

of the dynamic systems in question, both as a useful design tool and to reduce requirements on experiment instrumentation. Forces and torques in the experiment are then measured indirectly by accurate tracking of wing kinematics. The agreement between experimental and theoretical wing trajectories provides basic verification of the numerical model. Analysis of internal forces and torques, extracted from the numerical model, demonstrates mechanically intelligent behavior.

The fixed wing experiment of §3.3 focuses on *aerodynamic* drag torques produced by the wings. The aerodynamic drag torque results in a roll torque on the body, but consideration of the wings as external to the body requires that the inertial torques appearing from wing acceleration be included as well. The rotating wing experiment of §3.4, faced with complex inertial torques due to wing rotation, takes this more sophisticated approach considering regulation of the total (aerodynamic plus inertial) roll torque experienced by the body.

3.2 Numerical modeling

3.2.1 General objectives

The purpose of a dynamic model is to not only accelerate the design process by providing a tool to evaluate potential designs theoretically, but also to provide a more complete description of device dynamics than can be easily achieved through experiment alone. The dynamics of 100mg FWMAVs can be generally divided into two time-scales, the *wingbeat* timescale and the *body* timescale. This division recognizes that the wings typically weigh less than 1mg and operate at 100Hz or more,

while the body has 100 times the mass and will maneuver at timescales at least ten times longer. Furthermore, PARITy devices are advanced mechanisms to regulate wing flapping trajectories in response to imbalanced torques, and do not yet include elements that respond to motion of the body such as halteres or helicopter-style stabilizers. Thus, the simulation model focuses on wing dynamics under the assumption that motion of the body frame during flight will have a negligible impact.

The basic objective of the dynamic model is to capture the operation of various flapping-wing mechanisms, enabling evaulation of PARITy designs. However, the Microrobotics Lab produces a large variety of flapping wing mechanisms, and another objective of the dynamic model is the versatility to adapt to all of these designs. The effort has been successful: the dynamics software allows simulation of every single and multi-wing flapping device produced by this laboratory, and has been extended to legged devices as well.

3.2.2 Assumptions

The simulation model relies on several simplifying assumptions to decrease analytical complexity and computational requirements without unduly compromising accuracy:

1. *Fixed body frame.* This critical assumption is valid in free flight only if the motion of the body frame occurs on timescales much lower than the period of a wingstroke.

2. *Pseudo rigid body model.* Flexure-based joints in transmission linkages are perfect revolute joints without off-axis motion, while rigid links are infinitely

rigid [21]. Optimized 'castellated' flexure joint designs (Figure 4.25d) and stiff, low mass link materials justify this assumption.

3. *Linear elastic joints.* The joints themselves are lossless linear torsion springs, with spring constants derived from Euler beam bending theory. While valid for small deformations, this model is presumably inadequate for the large deformations exhibited by many devices, often exceeding the elastic limit of the flexure. However, the dynamics algorithms can easily incorporate nonlinear spring models and loss mechanisms should these be introduced in the future. Furthermore, the wings and the actuator are the dominant lossy and elastic elements, respectively, mitigating the impact of errors in modeling joint elasticity and energy loss.

4. *Zeroth-order actuator model.* The laminated piezoelectric actuator is modeled as a voltage proportional force in parallel with a linear spring. The dynamics simulation can accept more sophisticated actuator models.

5. *Massless mechanism.* The wings are the only inertias in the system as it dominates typical systems involving lightweight carbon fiber linkages and large transmission ratios between the actuator and wing. If necessary, the dynamic model can be expanded to include those systems where actuator or linkage mass contributes significantly to the dynamics.

6. *Blade-element model aerodynamics.* A blade element model (§3.2.4) with experimentally derived lift and drag coefficients approximates aerodynamics forces.

3.2.3 A first-principles mathematical approach

An Euler-Lagrange formulation of the equations of motion underlie the dynamic model. The fundamental mechanism under investigation is a wing driven through the spherical shoulder transmission described in §2.3.3. Though seemingly limited, these basic equations can be extended to encompass multi-wing flappers and span a wide range of devices including the HMF, Drag PARITy, Lift PARITy, and many others.

The spherical shoulder (including the passive wing hinge) is a three degree of freedom device. The three degrees of freedom are defined to be the wing rotation ψ and the two input angles of the spherical five-bar, ϕ and θ. If we define the three wing angles ψ_w, ϕ_w, and θ_w as the wing rotation, stroke angle, and deviation angles, respectively, we find that $\psi_w = \psi$, $\phi_w = \phi$, but $\theta_w = \theta_w(\phi, \theta)$. Depending on linkage design, θ_w can be approximately equal to θ over a large range of ϕ (see §2.3.3). The state vector $\vec{q}$ for this system has six elements, incorporating the three configuration angles and their time derivatives. The configuration vector $\vec{p}$ and the state vector $\vec{q}$ are defined:

$$\vec{p} \equiv \begin{pmatrix} \phi & \theta & \psi \end{pmatrix}^T \tag{3.1}$$

$$\vec{q} \equiv \begin{pmatrix} \vec{p} \\ \dot{\vec{p}} \end{pmatrix} \tag{3.2}$$

The wing inertia undergoing 3-DOF rotation about the spherical center is the only kinetic energy element in the system. The six dynamic joints within the spherical linkage, the actuator, and additional joints within any linkages used to drive spherical shoulder inputs store potential energy. The effect of the six spherical joints are integrated into the model. Since the form of additional linkages and the actuator

configuration can be variable, in practice these are accounted for in the most natural coordinate frame and then applied to the ϕ, θ, ψ coordinate frame through a Jacobian. The specific form of the dynamics equations are given in Appendix A.

All actuation forces and aerodynamic forces appear as generalized torques, converted into the correct coordinate frame with appropriate Jacobians. A voltage-proportional force, with proportionality constant derived from a laminate plate theory, describes piezoelectric actuation [42]. A blade-element model provides a state-based description of aerodynamic forces (§3.2.4) that are grounded in experiment. The final form of the equations of motion is:

$$\mathbf{M}(\vec{p}, \dot{\vec{p}})\ddot{\vec{p}} = \vec{f}(\vec{p}, \dot{\vec{p}}) + \vec{\tau}(\vec{p}, \dot{\vec{p}}, t) \tag{3.3}$$

In the preceding equation, $\mathbf{M}$ is a mass matrix, $\vec{f}$ arises from the linkage dynamics, and $\vec{\tau}$ encapsulates all generalized torques. Though this approach seems to be limited to single wing flappers with a specific configuration, a versatile system of applied constraints (§3.2.5) allows this core functionality to capture the behavior of all flapping wing devices produced to date in the Microrobotics Laboratory, and has been applied to leg driving structures for ambulatory robots as well.

3.2.4 Aerodynamics

A blade-element model describes aerodynamic effects, assuming a perfectly rigid wing planform. The wing coordinates ϕ_w, θ_w, and ψ_w, are not a natural coordinate system for expressing aerodynamic moments, as they are referenced to the body of the robotic insect. The aerodynamics equations use a new set of coordinates

based on the direction of relative wind, wind-relative stroke velocity $\dot{\phi}_{\text{rw}}$ and wind-relative rotation ψ_{rw}. The wind-relative stroke velocity combines stroke velocity $\dot{\phi}$ and deviation velocity $\dot{\theta}$ to express the total angular speed in the deviated stroke plane. The wind-relative rotation ψ_{rw} expresses wing rotation shifted such that $\psi_{\text{rw}} = 0$ corresponds to a wing perpendicular to the relative wind. Wind-relative rotation is an expression of the angle of attack α:

$$\alpha = \frac{\pi}{2} - \psi_{\text{rw}} \text{sgn} \dot{\phi}_{\text{rw}} \tag{3.4}$$

Note that in the absence of deviation during flapping ($\theta_w = \dot{\theta}_w = 0$), wind-relative coordinates are identical to their non-relative counterparts.

Under this blade-element model, lift and drag torques are proportional to $\dot{\phi}^2_{\text{rw}}$, the square of relative stroke velocity. An empirical model provides averaged lift and drag coefficients, strong functions of the angle of attack, relying on experimental data collected from dynamically scaled models of a fruit fly wing flapping in mineral oil [11]:

$$C_D = 1.92 - 1.55 \cos\left(2.04\alpha - 9.82^\circ\right) \tag{3.5}$$

$$C_L = 0.225 + 1.58 \sin\left(2.13\alpha - 7.20^\circ\right) \tag{3.6}$$

These lift and drag coefficients can be expressed as coefficients for forces normal (C_N) and tangential (C_T) to the wing by an appropriate coordinate transform. Rotational damping, proportional to $\dot{\psi}^2$, the square of wing rotational velocity, has been modeled in accordance with experimental and theoretical work on tumbling plates [1].

Calculation of wing rotational moments, important for realizing passive wing rotation, relies on additional experimental work quantifying a non-dimensional center

of pressure location $\hat{d}_{cp}$ as a function of angle of attack α in fruit fly wings [12, 39]:

$$\hat{d}_{cp} = \frac{0.82}{\pi} |\alpha| + 0.05 \tag{3.7}$$

The complete aerodynamic model can be distilled into the following four aerodynamic moments applied to the wing:

$$M_N = -\Omega_1 \text{sgn}(\dot{\phi}_{\text{rw}}) \dot{\phi}_{\text{rw}}^2 C_N(\psi) \tag{3.8}$$

$$M_T = -\Omega_1 \text{sgn}(\dot{\phi}_{\text{rw}}) \dot{\phi}_{\text{rw}}^2 C_T(\psi) \tag{3.9}$$

$$M_{rd} = -\Omega_2 \text{sgn}(\dot{\psi}_{\text{rw}}) \dot{\psi}_{\text{rw}}^2 C_{rd} \tag{3.10}$$

$$M_r = -\left(\Omega_3 \hat{d}_{cp}(\psi_{\text{rw}}) - \Omega_4\right) \text{sgn}(\dot{\phi}_{\text{rw}}) \dot{\phi}_{\text{rw}}^2 C_N(\psi) \tag{3.11}$$

In the previous set of equations, M_T acts about an axis perpendicular to the wing plane and is the result of aerodynamic forces acting in the wing plane. M_r and M_{rd} are the rotational and rotational damping moments, respectively, both acting on the wing around the wing hinge axis. M_N acts about an axis perpendicular to both the wing plane normal and the hinge axis, and results from aerodynamic forces normal to the wing. The three aerodynamic coefficients, related to tangential (C_T), normal (C_N), and rotational damping (C_{rd}) aerodynamic forces, are described in [39]. These four aerodynamic moments are treated in the dynamic model as generalized torques.

The parameters Ω_1, Ω_2, Ω_3, and Ω_4 have units of mg·mm^2 and can be calculated from the air density ρ and the specific wing morphology. For these integrals, the coordinate system origin is coincident with the spherical center of the wing; the wing planform lies in the zx-plane, with the z-axis aligned spanwise with the wing hinge and the x-axis extending chordwise (Figure 3.1). The quantity $c(z)$ is the chord length, measuring the distance between leading and trailing edge a distance z from

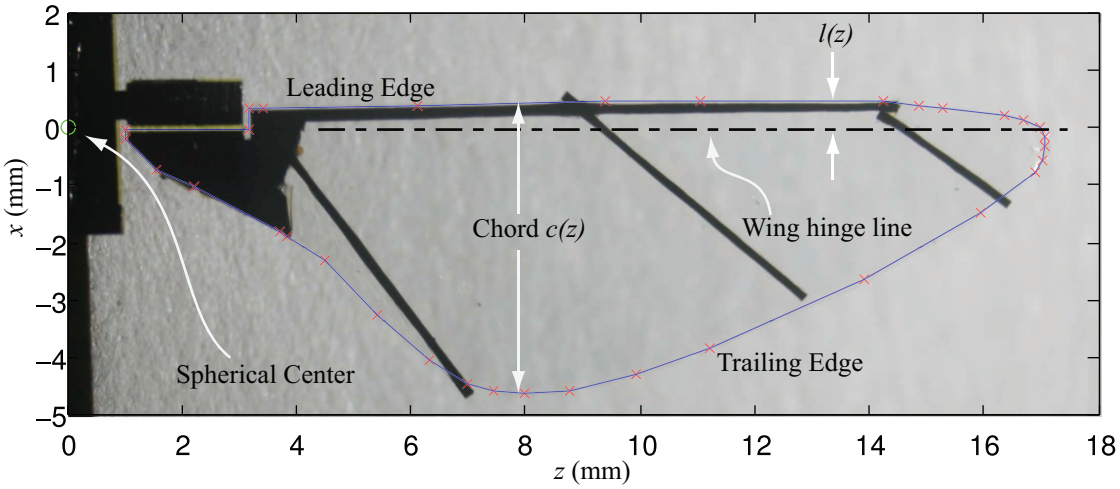

Figure 3.1: Definitions of wing planform for calculating relevant aerodynamics integrals.

the origin. The quantity $l(z)$ is the x-coordinate of the leading edge, that is, the distance from the leading edge to the hinge line, at a spanwise distance z. With double integrals taken over the wing planform area and single integrals taken along the entire span of the wing, the four parameters are:

$$\Omega_1 = \frac{1}{2}\rho \iint z^3 \mathrm{d}A \tag{3.12}$$

$$\Omega_2 = \frac{1}{2}\rho \iint \left|x^3\right| \mathrm{d}A \tag{3.13}$$

$$\Omega_3 = \frac{1}{2}\rho \int z^2 c(z)^2 \mathrm{d}z \tag{3.14}$$

$$\Omega_4 = \frac{1}{2}\rho \int z^2 l(z) c(z) \mathrm{d}z \tag{3.15}$$

All integrals can be pre-calculated, so this model allows computationally inexpensive determination of aerodynamic forces and torques. Experiments run by collaborator Peter Whitney provide experimental support that this aerodynamic model

adequately describes passive rotation of a single wing executing a predetermined stroke angle trajectory without deviation, along with generated lift forces [39]. This referenced work contains a detailed description of the aerodynamic model briefly summarized here.

3.2.5 Versatility through constraints

The core simulation of a single wing driven by a spherical shoulder can be applied to many different mechanisms by a methodology of simulating multiple systems that interact only through coupling constraint torques. A general formulation of this process will be described, accompanied by application to the specific case of simulating the HMF wing dynamics.

General formulation

Suppose a system has n wings. There are then n configuration vectors, one for each wing, of the form $\vec{p}_i$. The total configuration vector $\vec{p}$ is defined:

$$\vec{p} \equiv \begin{pmatrix} \vec{p}_1 \\ \vec{p}_2 \\ \vdots \\ \vec{p}_n \end{pmatrix} \tag{3.16}$$

These systems can easily be simulated independently. However, many useful systems do not have fully independent wings, and instead have linkage-based constraints between the wings. A subset of possible constraints can be captured by the following

linear constraint equation:

$$\mathbf{C}\vec{p} = \vec{c}_0 \tag{3.17}$$

The terms $\mathbf{C}$ and $\vec{c}_0$ are constants, and each row of $\mathbf{C}$ corresponds to a constraint. Introducing a vector of Lagrange multipliers $\vec{\lambda}$ results in a Lagrangian of the form $L = U - V + \vec{\lambda}^T(\mathbf{C}\vec{p} - \vec{c}_0)$. The Euler-Lagrange equations (3.3) take a modified form:

$$\mathbf{M}\ddot{\vec{p}} = \vec{f} + \vec{\tau} + \mathbf{C}^T\vec{\lambda} \tag{3.18}$$

Taking two derivatives of (3.17) gives $\mathbf{C}\ddot{\vec{p}} = \vec{0}$, allowing substitution into (3.18) to solve for $\vec{\lambda}$:

$$\vec{\lambda} = -\left(\mathbf{C}\mathbf{M}^{-1}\mathbf{C}^T\right)^{-1}\mathbf{C}\mathbf{M}^{-1}\left(\vec{f} + \vec{\tau}\right) \tag{3.19}$$

Substituting this solution for $\vec{\lambda}$ into (3.18) gives the modified equations of motion describing the dynamics of the constrained system:

$$\boxed{\ddot{\vec{p}} = \mathbf{M}^{-1}\left(\mathbf{I} - \left(\mathbf{C}\mathbf{M}^{-1}\mathbf{C}^T\right)^{-1}\mathbf{C}\mathbf{M}^{-1}\right)\left(\vec{f} + \vec{\tau}\right)} \tag{3.20}$$

Note that $\vec{c}_0$ does not appear in the equations of motion. Rather, initial conditions must ensure that $\mathbf{C}\vec{p}\,\big|_{t=0} = \vec{c}_0$ and $\mathbf{C}\dot{\vec{p}}\,\big|_{t=0} = 0$. The equations of motion (3.20) then ensure that $\mathbf{C}\vec{p} = \vec{c}_0$ for all t.

Specific configurations

The HMF is a two-winged flapper with three degrees of freedom. Using 'L' and 'R' superscripts to refer to the left and right wings, respectively, the configuration

vector $\vec{p}$ is:

$$\vec{p} = \begin{pmatrix} \phi^L & \theta^L & \psi^L & \phi^R & \theta^R & \psi^R \end{pmatrix}^T \tag{3.21}$$

The HMF uses a much simpler shoulder hinge that disallows any deviation from the stroke plane ($\theta^L = 0,\ \theta^R = 0$). The four bar wing transmission constrains the two stroke angles to be equal ($\phi^L = \phi^R$). These constraints can be collected into the single matrix equation of the form of (3.17):

$$\begin{pmatrix} 0 & 1 & 0 & 0 & 0 & 0 \\ 0 & 0 & 0 & 0 & 1 & 0 \\ 1 & 0 & 0 & -1 & 0 & 0 \end{pmatrix} \vec{p} = \begin{pmatrix} 0 \\ 0 \\ 0 \end{pmatrix} \tag{3.22}$$

This constraint equation defines the $\mathbf{C}$ matrix appearing in the constrained dynamics equations (3.20). This configuration (Configuration #1) and selected others are compiled in Table 3.1, along with their associated $\mathbf{C}$ matrices.

This methodology of applying constraints allows the simulation to be configured to reflect a large variety of devices. This simulation model will now be applied to several HMF and Drag PARITy configurations. Close correspondence of simulation results and real performance of selected physical implementations lend validity to this simulation model. Furthermore, numerical torque results provide insights into the mechanically regulated operation of PARITy designs.

Name	#	**C**	Wing rotation
HMF	1	$\begin{bmatrix} 0 & 1 & 0 & 0 & 0 & 0 \\ 0 & 0 & 0 & 0 & 1 & 0 \\ 1 & 0 & 0 & -1 & 0 & 0 \end{bmatrix}$	√
	2	$\begin{bmatrix} 0 & 1 & 0 & 0 & 0 & 0 \\ 0 & 0 & 0 & 0 & 1 & 0 \\ 1 & 0 & 0 & -1 & 0 & 0 \\ 0 & 0 & 1 & 0 & 0 & 0 \\ 0 & 0 & 0 & 0 & 0 & 1 \end{bmatrix}$	×
Drag PARITy	3	$\begin{bmatrix} 0 & 1 & 0 & 0 & 0 & 0 \\ 0 & 0 & 0 & 0 & 1 & 0 \end{bmatrix}$	√
	4	$\begin{bmatrix} 0 & 1 & 0 & 0 & 0 & 0 \\ 0 & 0 & 0 & 0 & 1 & 0 \\ 0 & 0 & 1 & 0 & 0 & 0 \\ 0 & 0 & 0 & 0 & 0 & 1 \end{bmatrix}$	×
Lift PARITy	5	$\begin{bmatrix} 0 & 1 & 0 & 0 & -1 & 0 \\ 1 & 0 & 0 & -1 & 0 & 0 \end{bmatrix}$	√
	6	$\begin{bmatrix} 0 & 1 & 0 & 0 & -1 & 0 \\ 1 & 0 & 0 & -1 & 0 & 0 \\ 0 & 0 & 1 & 0 & 0 & 0 \\ 0 & 0 & 0 & 0 & 0 & 1 \end{bmatrix}$	×
Dual PARITy	7	$\begin{bmatrix} 0 & 1 & 0 & 0 & -1 & 0 \end{bmatrix}$	√
	8	$\begin{bmatrix} 0 & 1 & 0 & 0 & -1 & 0 \\ 0 & 0 & 1 & 0 & 0 & 0 \\ 0 & 0 & 0 & 0 & 0 & 1 \end{bmatrix}$	×

Table 3.1: Various simulation configurations and the constraint matrices **C** that define them.

3.3 Drag PARITy with fixed wings

3.3.1 Study setup

The primary benefit of the PARITy drivetrain is its ability to passively compensate for asymmetric aerodynamic conditions. These can arise from factors external to the microrobotic insect, such as wind gusts or thermal variations, or they can arise from internal factors such as asymmetries due to fabrication variation or degradation during operation. Asymmetry of the wing membranes, accurately achievable in a laboratory setting, was used to assess the performance of the Drag PARITy in comparison to the baseline HMF drivetrain which exhibits no load balancing characteristics. A 'Control' simulation of the two drivetrains was conducted with symmetric wing parameters. Due to the absence of wing rotation, only a single aerodynamic pa-

Drivetrain	Trial	Ω^R ($mg{\cdot}mm^2$)	Ω^L ($mg{\cdot}mm^2$)	$\Delta\tau_{w,\text{drag}}{}^{\dagger}$ ($mN{\cdot}mm$)	$\tau^R_{w,\text{drag}}{}^{\dagger}$ ($mN{\cdot}mm$)	$\tau^L_{w,\text{drag}}{}^{\dagger}$ ($mN{\cdot}mm$)	**Drag Torque Imbalance** ***instantaneous***	***peak***
HMF	Control	31.3	31.3	0.00	12.42	12.42	**0.0%**	**0.0%**
	1-Cut	31.3	18.8	5.52	13.78	8.26	**40.1%**	**40.1%**
	2-Cut	31.3	13.2	8.32	14.35	6.03	**58.0%**	**58.0%**
PARITy	Control	31.3	31.3	0.03	12.46	12.47	**0.2%**	**0.1%**
	1-Cut	31.3	18.8	0.97	10.73	10.77	**9.0%**	**0.3%**
	2-Cut	31.3	13.2	1.46	9.56	9.46	**15.3%**	**1.0%**

† Peak magnitude over wingstroke.

Table 3.2: Simulation results comparing the displacement-balancing HMF drivetrain with the torque-balancing PARITy drivetrain.

rameter Ω_1, described in §3.2.4, is required. For the scope of this case study (§3.3), the subscript 1 will be dropped and this parameter will be referred to as the 'drag parameter.' A superscript indicates the left (L) or right (R) wing, and the subscript indicates the 'Control', '1-Cut,' or '2-Cut' trial. Since $\Omega^L_{\text{Control}} = \Omega^R$, both the HMF and the PARITy drivetrains produce balanced aerodynamic drag torques on each wing in the Control trial.

The simulation process consists of applying a sinusoidal voltage to the drive actuator and recording resulting wing stroke trajectories. The experimental setup reflects simulation configuration #4 from Table 3.1, whereas the baseline configuration reflects configuration #2. From a laminate plate theory analysis, the cantilever beam actuator has a linear spring constant of 467mN/mm, and exerts a 120mN amplitude sinusoidal force under a 100V amplitude sinusoidal drive signal [42]. The drive signal is applied at 110Hz, near mechanical resonance to increase stroke amplitude and limit reactive power.

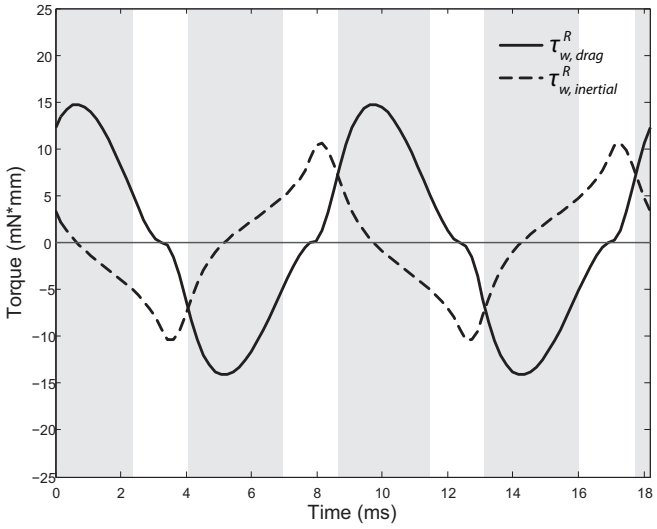

Figure 3.2: Theoretical torques $\tau^R_{w,\text{drag}}$ and $\tau^R_{w,\text{inertial}}$ applied by the right wing in a symmetric system. In shaded regions, $|\tau^R_{w,\text{drag}}| > |\tau^R_{w,\text{inertial}}|$.

Removing a section of the wing membrane effectively reduces the area of the wing planform. If the left wing is altered in this manner, its drag parameter Ω^L will be smaller than Ω^R of the unaltered right wing. The HMF drivetrain will always produce symmetric trajectories for the wings, meaning that their angular velocities are constrained to be equal and opposite. If membrane removal from the left wing results in its drag parameter being 59.9% of the drag parameter of the right wing, we expect that use of the HMF drivetrain will result in the drag torque experienced by the left wing to be 59.9% of that experienced by the right wing at every point in time. The condition $\Omega^L_{\text{1-Cut}} = 0.599 \cdot \Omega^R$ will be called the '1-Cut' trial, and the drag torques experienced by each wing using the HMF drivetrain are illustrated in Figure 3.3a. The results of a second trial, the '2-Cut' trial, in which the left wing's drag parameter has been reduced to 42.0% of that of the right wing ($\Omega^L_{\text{2-Cut}} = 0.420 \cdot \Omega^R$)

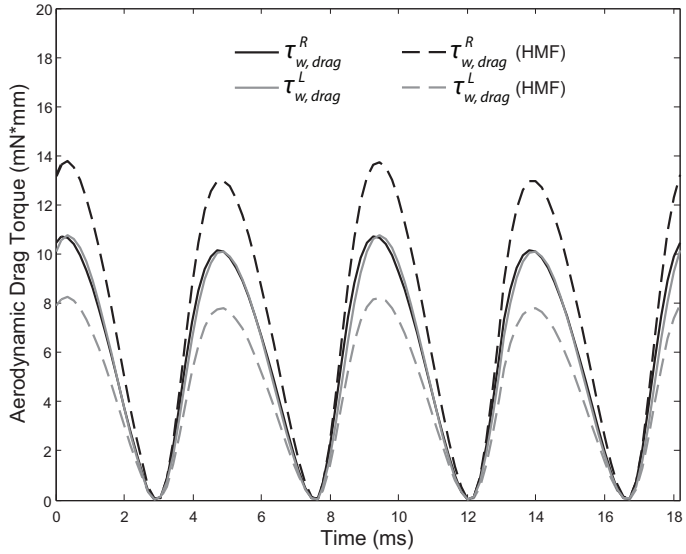

(a)

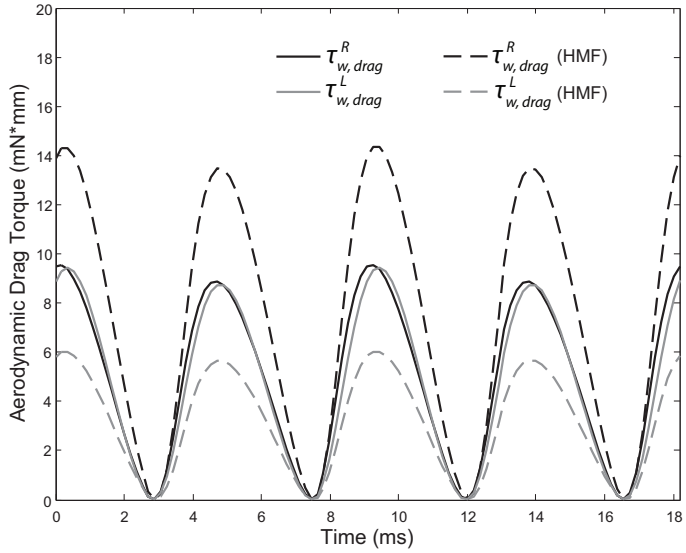

(b)

Figure 3.3: Simulated drag torques. For both results, the right wing has a torque parameter $\Omega^R = 31.3\,\text{mg}{\cdot}\text{mm}^2$. The left wing drag parameter Ω^L has been reduced to (a) $0.599 \cdot \Omega^R$ and (b) $0.420 \cdot \Omega^R$.

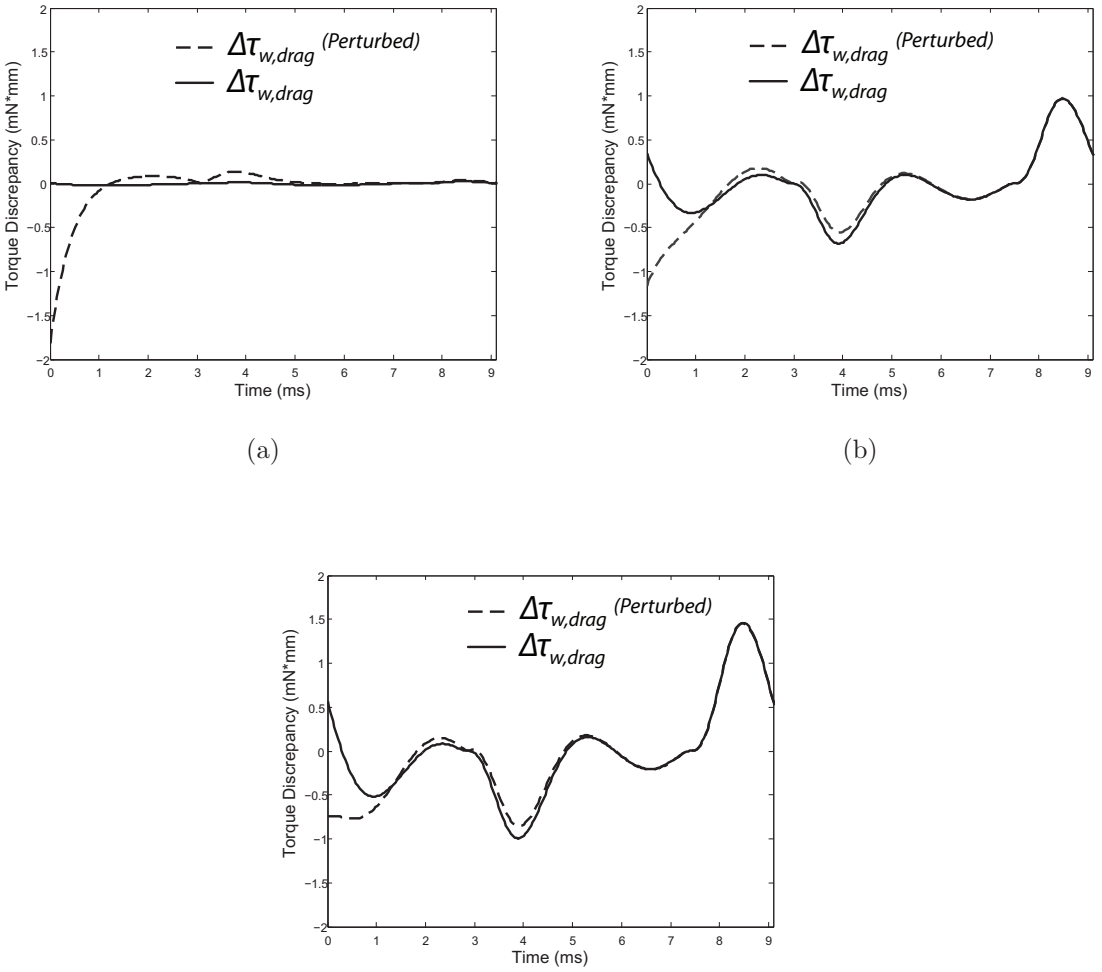

(a)

(b)

(c)

Figure 3.4: Solid lines indicate the instantaneous torque discrepancy $\Delta\tau_{w,\mathrm{drag}}$ between wings over a single cycle when (a) $\Omega^L_{\mathrm{Control}} = \Omega^R$, (b) $\Omega^L_{\text{1-Cut}} = 0.599 \cdot \Omega^R$, and (c) $\Omega^L_{\text{2-Cut}} = 0.420 \cdot \Omega^R$. Dashed lines describes the recovery of the torque imbalance from a 2 radian per second perturbation applied to the balance beam rotational velocity $\dot{q}_2$ at time $t = 0$.

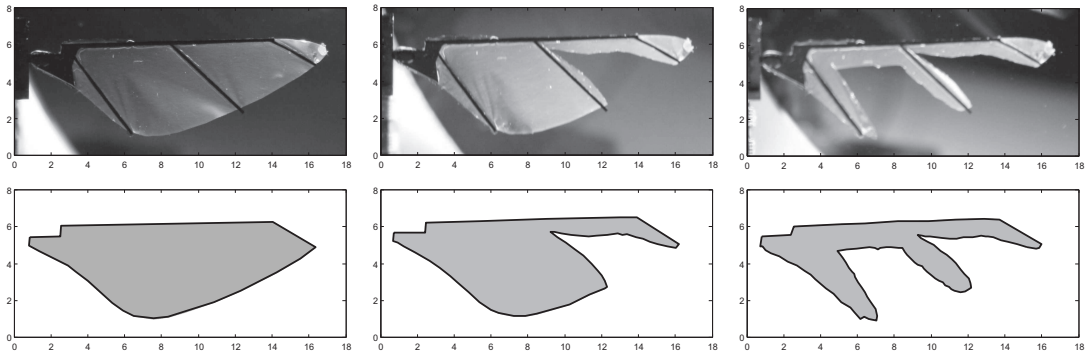

(a) (b) (c)

Figure 3.5: Images of left wing membrane as used for each trial, along with the associated planforms used to calculate the drag parameter Ω^L using the blade element model. Units are in millimeters. (a) Control Trial, $\Omega^L_{\text{Control}} = 31.3\,\text{mg}\cdot\text{mm}^2$. (b) 1-Cut Trial, $\Omega^L_{\text{1-Cut}} = 18.8\,\text{mg}\cdot\text{mm}^2$. (c) 2-Cut Trial, $\Omega^L_{\text{2-Cut}} = 13.2\,\text{mg}\cdot\text{mm}^2$.

are shown in Figure 3.3b. The system parameters for these two trials are chosen to correspond with that realized by the experimental procedure (§3.3.2).

In contrast with the HMF drivetrain, the PARITy drivetrain does not constrain the wing stroke angles to have symmetric trajectories. The load balancing characteristics of the transmission act to match the aerodynamic drag torques even in the presence of drastically asymmetric drag parameters. Figure 3.3 illustrates that with the use of the PARITy drivetrain, the aerodynamic drag torques experienced by both the left and right wings have been passively balanced by the system dynamics.

To quantitatively evaluate the simulated performance of the PARITy drivetrain relative to the baseline HMF drivetrain, two metrics have been defined, relevant once periodic operation has been established. The first is the *peak* drag torque imbalance, defined as the difference between the maximum drag torque magnitudes experienced

by each wing over a cycle. The second is the *instantaneous* drag torque imbalance, defined to be the maximum value of the torque discrepancy $\Delta\tau_{w,\text{drag}}$ over a cycle. Both metrics are normalized to the maximum drag torque experienced by the right wing over a cycle. The drag torque discrepancy $\Delta\tau_{w,\text{drag}}$ is defined:

$$\Delta\tau_{w,\text{drag}} \equiv \tau^{L}_{w,\text{drag}} + \tau^{R}_{w,\text{drag}} \tag{3.23}$$

Note that when the drag torques on the wings are balanced, $\Delta\tau_{w,\text{drag}} = 0$. Table 3.2 summarizes the performance of the HMF and PARITy drivetrains in the Control, 1-Cut, and 2-Cut trials.

The peak drag torque imbalance metric compares the amplitudes of the drag torques while ignoring their phase relationship. In the 1-Cut trial, the HMF drivetrain exhibits a peak drag torque imbalance of 40.1%, expected due to $\Omega^{L}_{\text{1-Cut}} = 0.599 \cdot \Omega^{R}$. Use of the PARITy, however, reduces this peak drag torque imbalance to 0.3%. In the 2-Cut trial, the peak torque imbalance of 58% exhibited by the HMF drivetrain is reduced to 1.0% with use of the PARITy drivetrain. Performing remarkably well, the PARITy drivetrain reduces the peak drag torque imbalance by a factor of 133 in the 1-Cut trial and a factor of 58 in the 2-Cut trial.

The instantaneous drag torque imbalance metric reports the maximum drag torque discrepancy $\Delta\tau_{w,\text{drag}}$ experienced during a wingstroke, relative to the peak drag torque magnitude of the unaltered wing. For the 1-Cut trial, an instantaneous drag torque imbalance of 40.1% exhibited by the HMF drivetrain is reduced to 9.0% by the PARITy drivetrain. For the 2-Cut trial, the HMF drivetrain's instantaneous drag torque imbalance of 58% is reduced to 15.3% by the PARITy drivetrain. Though the PARITy drivetrain still performs well, a slight phase shift between the drag torques on

each wing impacts its performance under the instantaneous drag torque metric. The drag torque discrepancy $\Delta\tau_{w,\text{drag}}$ is plotted over a single wingstroke in Figure 3.4.

In order to investigate the damping properties and time response of the torque balancing feedback loops, a perturbation was applied to the system in the form of a step change in $\dot{q}_2$ of 2 radians per second. This perturbation roughly corresponds to a 0.36 mN·mm·ms angular impulse applied to both wings. The impulse upsets the normal operation of the PARITy drivetrain, and the dashed lines in Figure 3.4 illustrate the recovery of $\Delta\tau_{w,\text{drag}}$. The drivetrain returns smoothly to periodic operation, regaining much of its steady state character with a time constant on the order of 1ms. For all trials, the perturbed performance is indistinguishable from that of the unperturbed system in less than one wingstroke (9.1ms).

3.3.2 Experimental setup

In order to experimentally verify the theoretical performance of the PARITy drivetrain design, an at-scale PARITy has been fabricated using SCM fabrication techniques [41]. The drivetrain is a symmetric structure consisting of links of the following lengths:

L_0	L_1	L_2	L_3	L_4
5000μm	2500μm	800μm	400μm	800μm

These values produce a PARITy drivetrain that maps a $\pm 200\mu$m actuation stroke into an approximately $\pm 35^\circ$ wing stroke. This is smaller than the wingstroke amplitude used to demonstrate a lift force greater than aeromechanical system mass [40]. However, reducing wing membrane area is expected to increase wing amplitude, and

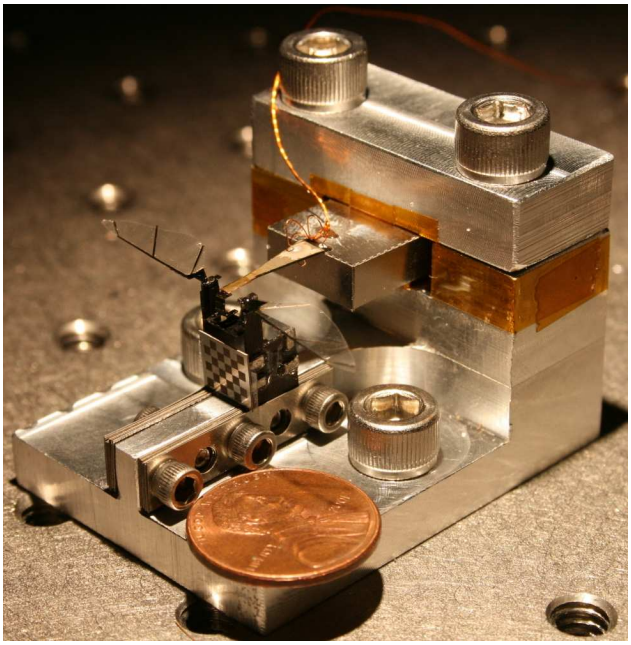

Figure 3.6: The experimental test structure.

a conservative baseline stroke amplitude is required to accommodate the extreme removal of wing membrane tested in the 2-Cut trial.

The transmission and actuator were mounted into a high-stiffness test structure (Figure 3.6) forming a nearly ideal mechanical ground. Two wings identical to within manufacturing tolerances were fabricated using structural carbon fiber spars and a 1.5μm thick polyester wing membrane. As fabricated, these wings, shown in Figure 3.5, have a mass of 834 μg and a moment of inertia around the wing pivot equal to 29.0mg·mm^2. The wings extend 16.0mm beyond the wing pivot, with an effective planform area of 51.4mm^2 (Figure 3.5a). Using integrals given in §3.2.4, the drag parameters Ω^R and $\Omega^L_{\text{Control}}$ were both calculated to be 31.3mg·mm^2 for the Control trial.

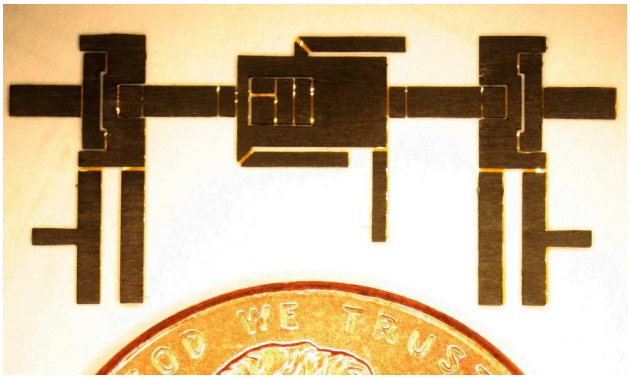

(a)

(b)

Figure 3.7: The PARITy drivetrain (a) before and (b) after folding.

A 110Hz sinusoidal drive signal with a constant 200V peak-to-peak amplitude was applied to the piezoelectric bimorph actuator. Wing trajectories were recorded using a high-speed video camera operating at 10,000 frames per second, approximately 91 frames per wingstroke. Wing angles were extracted from the video stream with image analysis software, producing about 91 data points per wingstroke over 10 wingstrokes for the Control trial.

For the 1-Cut trial, the data collection process was repeated after removing a section of the left wing membrane, reducing the wing planform area to 84.3% of its area in the Control trial. The drag parameter was recalculated, resulting in a modified drag parameter $\Omega^L_{\text{1-Cut}} = 18.8\text{mg}\cdot\text{mm}^2$, or 59.9% of Ω^R. The moment of inertia I^L of the left wing is not appreciably changed by the removal of wing membrane mass. For the 2-Cut trial, an additional section of wing membrane was removed, leaving 56.8% of the original wing planform resulting in $\Omega^L_{\text{2-Cut}} = 13.2\text{mg}\cdot\text{mm}^2$, or 42.0% of Ω^R. Again, I^L remains effectively constant due to the negligible contribution of the wing membrane mass to the moment of inertia. The wing planforms for all three trials are displayed in Figure 3.5.

Elastic deformation of the wings resulted in a discrepancy of as much as 8° between the angle of the distal end of the leading wing spar and the angle of the proximal end at the output of the PARITy drivetrain. In order to minimize the impact of this elastic deformation, wing stroke angles were extracted by tracking points on the leading wing spar extending no more than 5mm from the drivetrain output.

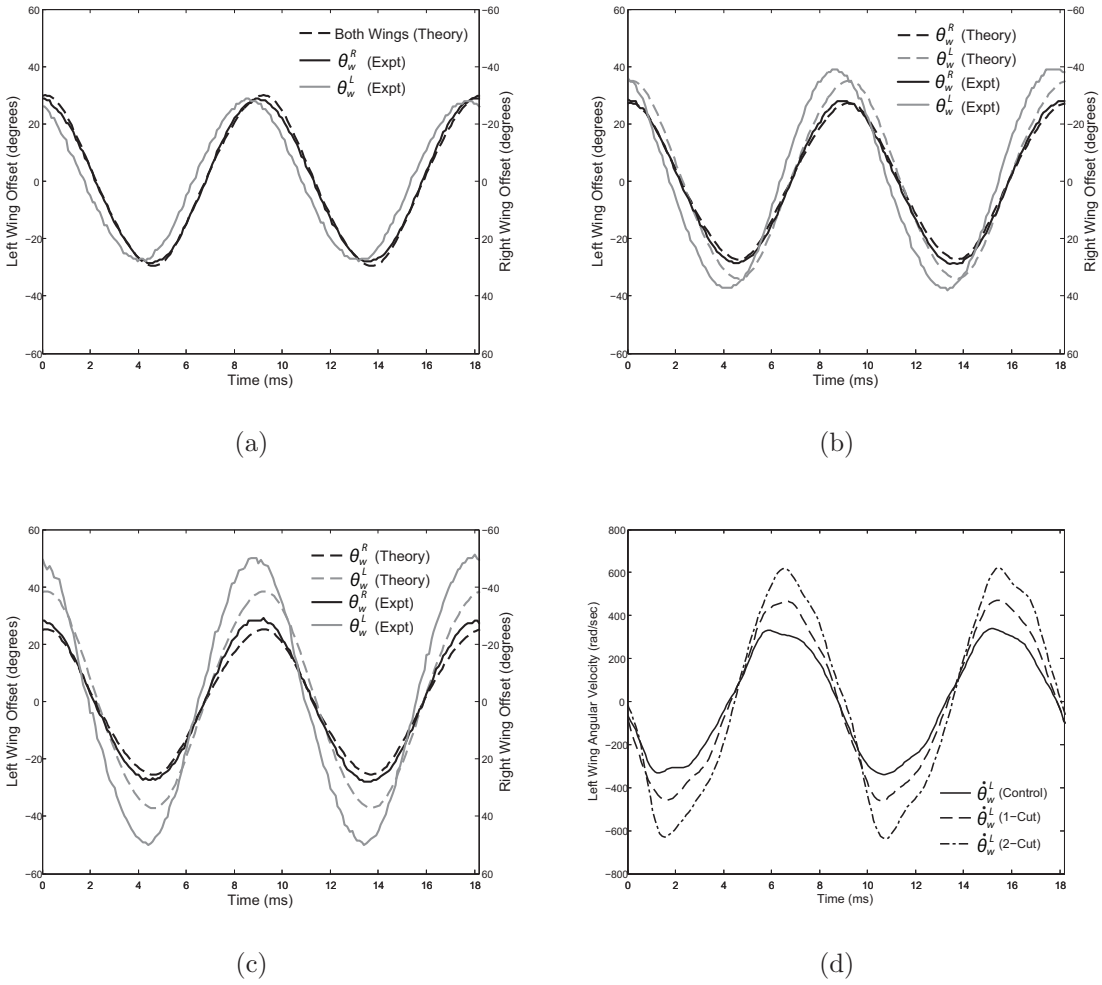

Figure 3.8: Theoretical predictions versus experimental wing trajectories for (a) the Control trial, (b) the 1-Cut trial, and (c) the 2-Cut trial. (d) Experimentally observed left wing velocities, low-pass filtered with an 800Hz cutoff frequency.

3.3.3 Results

The experimental wing trajectories for the Control, 1-Cut, and 2-Cut trials are plotted in Figures 3.8a, 3.8b, and 3.8c, along with the trajectories predicted by simulation. It is important to note that the phase relationship between the drive signal itself and the wing trajectory data from the video stream was not experimentally recorded. The theoretical predictions were aligned in time with experimental data by matching the phase of the fundamental 110Hz components of predicted and experimental wingstroke trajectories. This technique does not allow verification of the predicted phase shift between drive signal and wing trajectory, but it allows verification of the relative phase shift between the trajectories of the left and right wings.

In the Control trial, the symmetry of the system demands symmetric wing trajectories. However fabrication tolerances have created measurable errors. Two such effects are readily apparent in the experimental data:

1. The mean right wing stroke angle is $-9.5°$ while the mean left wing stroke angle has a magnitude of less than $0.5°$ (both removed from Figure 3.8).

2. The fundamental 110Hz oscillation of the left wingstroke leads that of right wingstroke by 0.45ms, a phase difference equal to 5.0% of a full flapping cycle.

Simulation of the Control trial produces mean stroke angles of less than $0.5°$ in magnitude. The observed mean right wing stroke angle of $-9.5°$ in the experimental trial can be attributed to an offset in the minimum potential energy configuration of the experimental test structure, likely caused by fabrication error. The exact cause of this offset could not be isolated, and it has been removed from plots of experimental

data.

The removal of the mean stroke angle is expected to have only a minor impact on the predicted wing trajectory because, when the wing is less than 40° from horizontal, the transmission ratio is relatively insensitive to wing angle. However, the 2-Cut experimental trial has a stroke amplitude approaching ±50°, so the non-zero mean stroke angle may contribute to the discrepancy between theory and experiment in this trial.

The phase difference of wing trajectories in the Control trial can be seen in Figure 3.8a. A symmetric system should not exhibit any phase difference but there are many possible asymmetries which can cause it. A difference between torsion spring constants in the transmission can lead to phase errors, as can mismatched wing inertias or transmission ratios caused by fabrication variation.

However, these asymmetries aside, Figures 3.8b and 3.8c provide clear evidence that the PARITy drivetrain manages the distribution of actuator power to compensate for asymmetric loading torques. The stroke amplitude of the left wing is increased in the 1-Cut trial to compensate for its reduced membrane area. It is larger still in the 2-Cut trial, where even more membrane area has been removed. The predicted wing trajectories demonstrate close, if not perfect, agreement with the experimental data. The increase in wing velocity as membrane is removed can be seen more clearly in Figure 3.8d.

The experimental wing trajectories correspond well with theoretical predictions of the simulation model. The theoretical model slightly underestimates the stroke amplitude increase of the altered wing in both the 1-Cut and 2-Cut trials, an effect

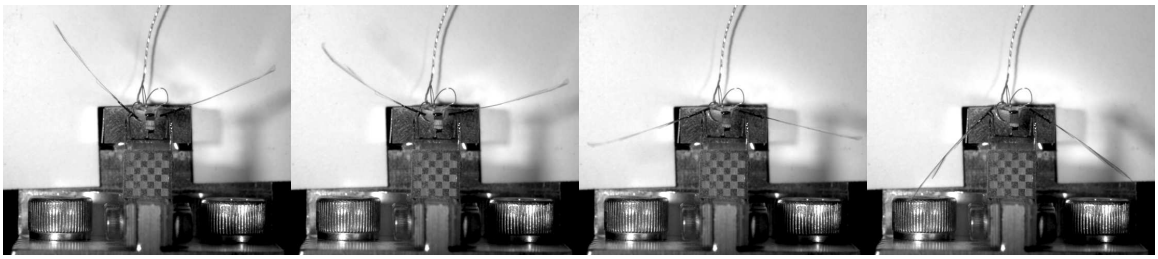

Figure 3.9: Image sequence from the '2-Cut' trial high speed illustrating increased amplitude of the left wing as compared to the right wing From left to right, elapsed time between adjacent images is 1.5 milliseconds. The checkerboard contains 1mm×1mm squares and is used for scale.

which can be attributed to overestimation of the drag parameters assigned to the complex altered wing planforms used in these trials. Though the drag torques were not directly measured in this test setup, the increased stroke amplitude of the wing with a reduced planform area is indirect evidence of the drag torque balancing nature of the PARITy drivetrain. Using a passive mechanism, the PARITy distributes power from the actuator in a manner that compensates for the altered wing's reduced capacity to induce aerodynamic drag torques.

3.4 Drag PARITy with rotating wings

In the preceding experiment, wings maintain an orientation perpendicular to the relative wind; the consequence of this simplicity is the failure of this system to generate any aerodynamic lift. Lift generation is critical for any viable transmission design for a flapping wing air vehicle. To address this issue, another experiment has been conducted by affixing wings capable of passive rotation to the outputs of the Drag

Wing	Left	Right	Right	Right
Trial	*All*	*Uncut*	*1-Cut*	*2-Cut*
I_{xx}	49.0	47.1	40.6	32.8
I_{yy}	50.5	48.6	42.0	34.1
I_{zz}	1.56	1.49	1.43	1.29
I_{xz}	4.20	3.87	3.38	2.97
Ω_1	46.8	38.2	28.7	21.2
Ω_2	0.587	0.438	0.419	0.387
Ω_3	17.5	13.5	10.6	9.10
Ω_4	0.712	0.952	0.787	0.691

Table 3.3: Inertial and aerodynamic parameters used for the left and right wings for the Uncut, 1-Cut, and 2-Cut trials. All values have units of mg·mm^2. The coordinate frame for inertial components is described in Figure 3.10, while aerodynamic parameters are described in §3.2.4.

PARITy transmission.

The resulting system has four degrees of freedom, compared to the two degree of freedom system of the preceding section. The Drag PARITy transmission contains two degrees of freedom, while the two wings each add a degree of freedom from their respective wing hinges. The orientation of each wing can be fully described by the angle of the corresponding transmission output (the 'stroke angle' ϕ) and the deflection angle of the wing hinge (the 'rotation angle' ψ), illustrated for the right wing in Figure 2.11c.

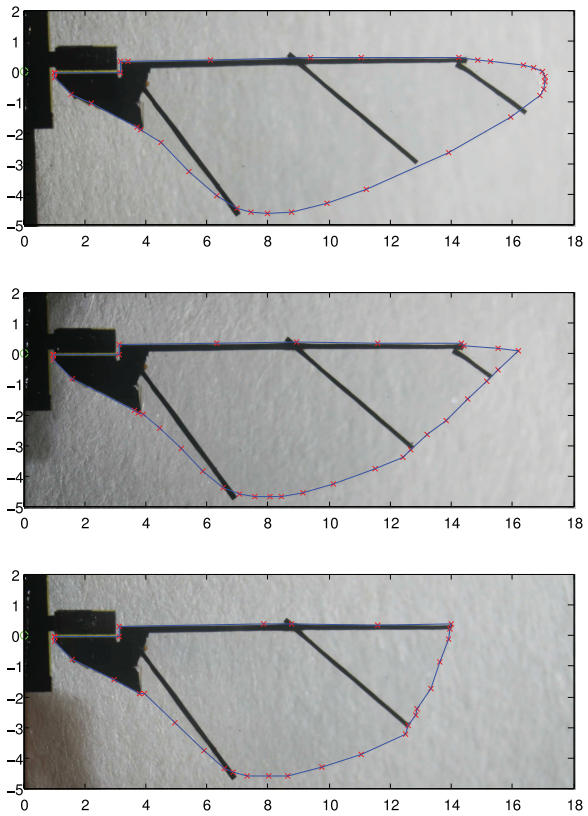

Figure 3.10: The wing with membrane outline indicated for the Uncut, 1-Cut, and 2-Cut trials, from top to bottom. Axis units are in mm. To properly orient inertial components from Table 3.3, the z and x coordinate axes correspond to horizontal and vertical image axes, respectively.

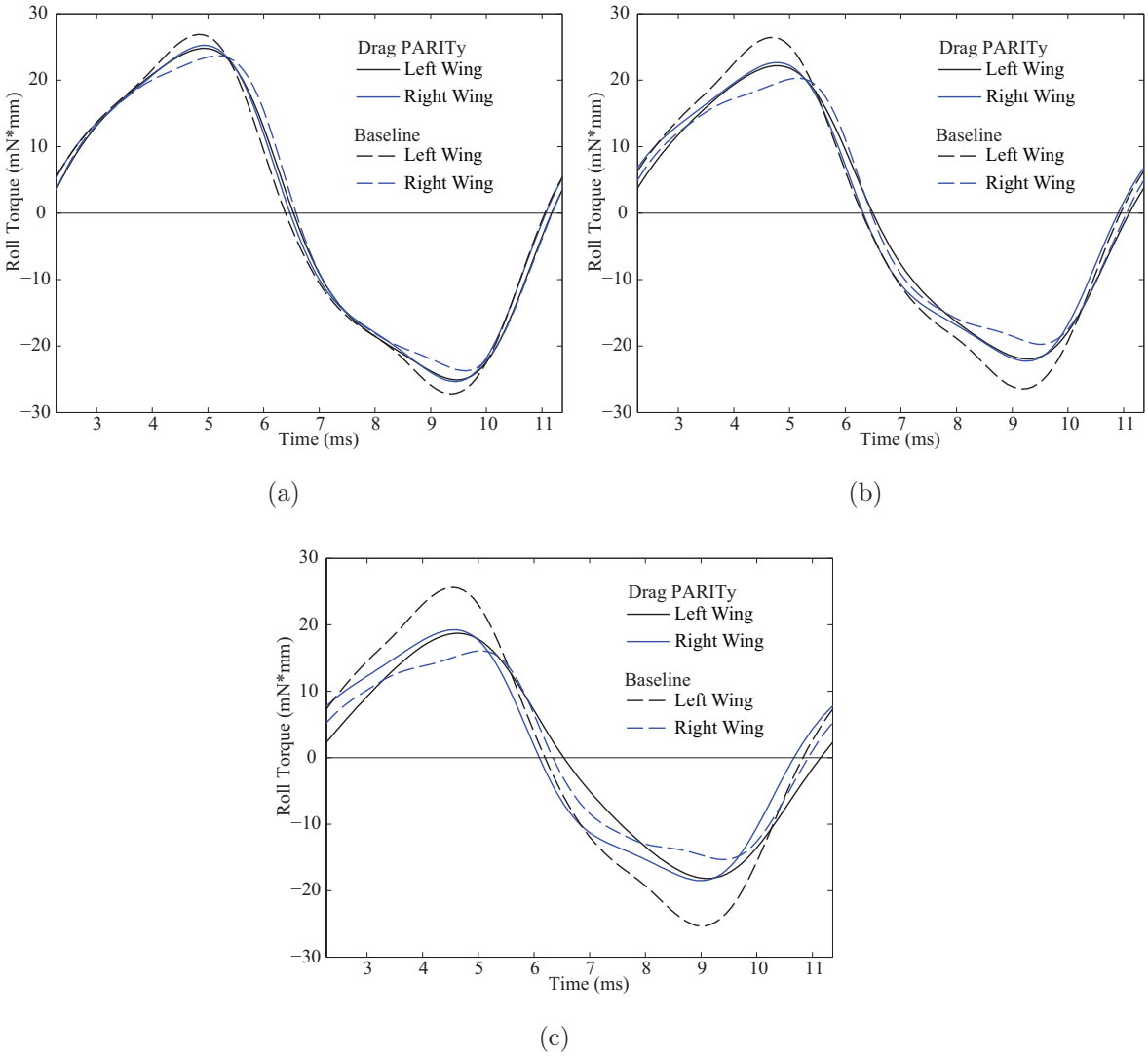

Figure 3.11: Theoretical roll torque imparted to the airframe by each wing in the (a) Uncut, (b) 1-Cut, and (c) 2-Cut trials. The difference between the roll torques imparted by the left and right wings appears as a net body torque on the airframe.

The theoretical dynamics model has been used to investigate the reaction torque regulating properties of the system in response to wing asymmetry. The system (#3 in Table 3.1) was compared with a baseline design in which the Drag PARITy transmission has been replaced with a conventional transmission characterized by fully actuated wing stroke angles. This baseline design, #1 in Table 3.1, is realized by freezing the degree of freedom q_2 of the Drag PARITy to $q_2 = 0$ (equivalent to the constraint $\phi^L = \phi^R$).

A control trial, which will be called the 'Uncut' trial, was simulated using a structure mechanically and aerodynamically symmetric to the tolerances achievable with the SCM manufacturing process. Two additional trials were undertaken with intentionally asymmetric wing parameters, realized by removing successive amounts of planform area from the distal extent of the right wing. These trials will be called the 1-Cut and 2-Cut trials, respectively. Images of the right wing planform for all three trials are shown in Figure 3.10. The left wing is nominally identical to the Uncut right wing for all three trials.

The wing parameters for the 'Uncut' trial were chosen to imitate those proven to enable tethered take-off in [40]. Since neither wing fabrication, mounting, nor the removal of wing area were precision processes, all wing parameters were measured directly from wings in situ on the experimental test structure. Inertia tensors for the wing were constructed using a baseline mass measurement coupled with a photogrammetric process to determine the spatial distribution of wing mass. Aerodynamic parameters for the wings were calculated using the photogrammetrically determined wing planform areas shown in Figure 3.10. Fabrication variation has

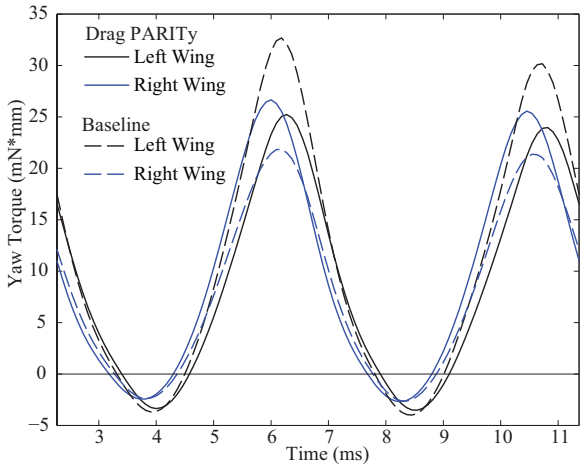

Figure 3.12: Yaw torque in the 1-Cut Trial.

resulted in measurable asymmetry even in the Uncut case, apparent in theoretical and experimental results. See Table 3.3 for all calculated inertial and aerodynamic parameters.

In all trials, the Drag PARITy design is observed to execute stable wing trajectories qualitatively similar to those executed by biological insects. Wing stroke angles ϕ^L and ϕ^R oscillate over approximately 100° with rotation angles ψ^L and ψ^R oscillating ±60°, approximately 90° out of phase. These rotation angles correspond to an angle of attack $\alpha = 90°$ at stroke extents and $\alpha = 30°$ midstroke. Significant yaw torques (Figure 3.12) result largely from aerodynamic lift, demonstrating Drag PARITy operation on a lift-generating platform. Theoretical wing trajectories are plotted in Figures 3.13a and 3.13c.

3.4.1 Experimental results

After acquiring data for the Uncut trial, the right wing was cut in situ to conduct the 1-Cut and 2-Cut trials without perturbing the alignment of the wing on the transmission output. As previously mentioned, all dynamic wing parameters were measured without disturbing the device and are presented in Table 3.3.

Two high speed video cameras were positioned such that each obtained a clear view of both wings over the entire flapping motion. Prior to acquiring video, the cameras were calibrated using routines from the Caltech Camera Calibration Toolbox for MATLAB [4]. Once calibrated, the toolbox allows reconstruction of three dimensional coordinates of points identified in both camera views.

A 110Hz 200V (peak to peak) sinusoidal voltage was applied to the power actuator and synchronized high speed video was acquired from both video cameras at 10,000fps, or 91 frames per wingstroke period. Sample still frames are shown in Figure 3.15.

Three easily distinguished features of the wing venation pattern were manually tracked across 300 frames for each trial. Identification of all three points in two camera views allows stereophotogrammetric reconstruction of the full wing orientation. The sinusoidal drive voltage applied to the actuator has been recorded and digitized at 5kHz, synchronized with the high speed video stream.

The observed stroke and rotation angles are plotted as a function of time in Figure 3.13, along with predictions produced by the theoretical model. Time synchronization has been achieved by aligning the theoretical and experimental drive signals, omitted from the plots for clarity. The functional form of the applied voltage signal

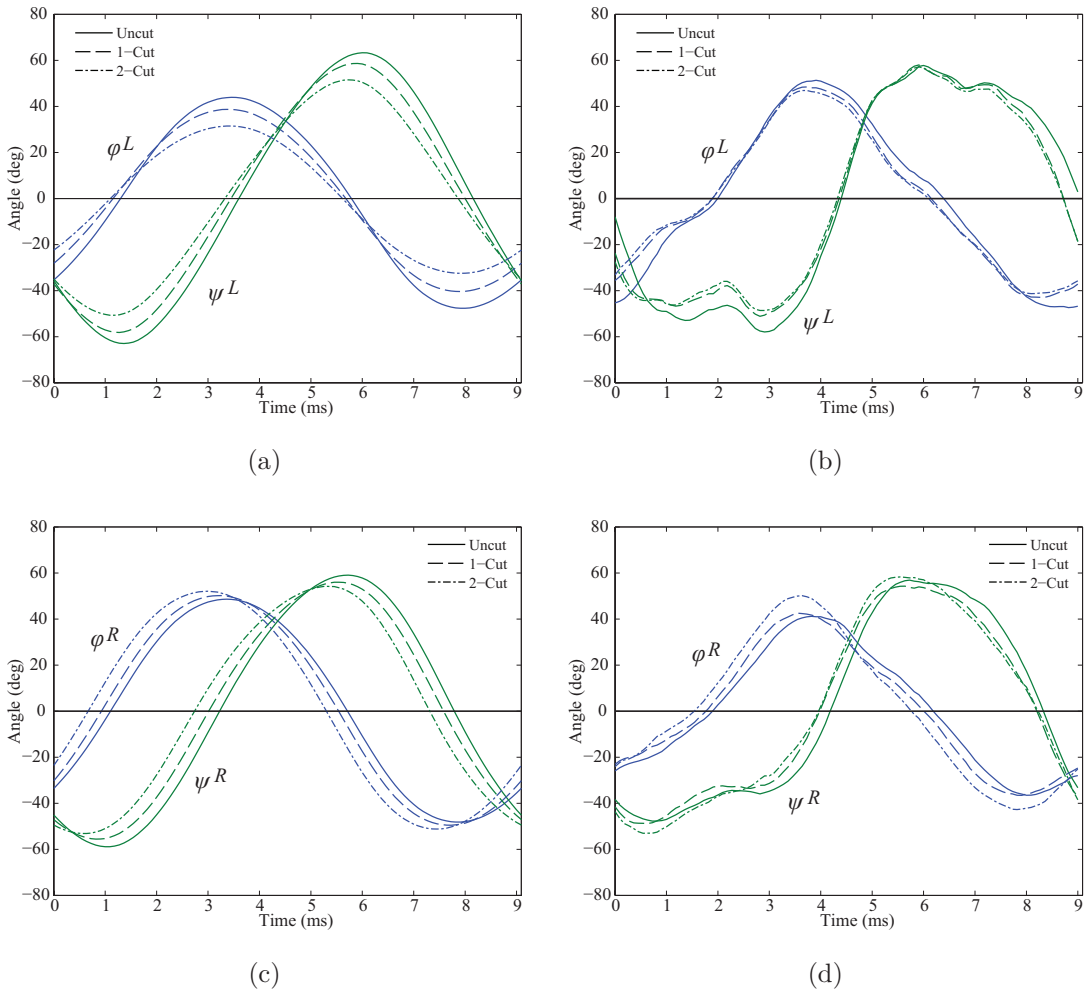

Figure 3.13: Left wing trajectories (a) predicted by theory and (b) observed experimentally, along with (c) theoretical and (d) experimental right wing trajectories. Wing stroke angle trajectories ϕ^L and ϕ^R adapt to compensate for asymmetric wing parameters; rotation angles ψ^L and ψ^R are also impacted.

as a function of time (in seconds) is:

$$V(t) = 100V + 100V \cdot \sin\left(110 \cdot 2\pi t\right) \tag{3.24}$$

From Figure 3.13, it is immediately apparent that the theoretical model accurately captures qualitative characteristics of the experimental model, with rotation angle ψ exhibiting an approximately 90° phase lag behind the stroke angle ϕ. Furthermore, the theory also accurately predicts oscillation amplitudes from applied drive voltage, no small achievement considering the complexity of this nonlinear dynamic system.

Theoretically predicted trends in wing trajectories as the right wing planform is altered are apparent in experimental data. The model predicts a monotonic increase in $\phi^R(t)$ amplitude as planform area is successively removed from the right wing, coupled with an associated decrease in the amplitude of $\phi^L(t)$. This trend is reflected in the experimental data as the Drag PARITy transmission passively diverts additional power to the underperforming right wing. The model also predicts a successive decrease in the amplitudes of both wing rotations $\psi^L(t)$ and $\psi^R(t)$ as wing membrane is removed. This trend is apparent in the observed trajectory of $\psi^L(t)$, though somewhat ambiguous in the observed trajectory of $\psi^R(t)$.

Among features not predicted by this simulation model are the square-wave appearance of observed wing rotations and the complex non-sinusoidal details of stroke angle trajectories. In future work, it is hoped that these discrepancies will be reduced by a more detailed theoretical model including, for example, mechanical loss mechanisms and nonlinear descriptions of polymer flexures to better predict dynamic characteristics at large joint angles. The transmission design itself will be refined to limit unintended and difficult to model behavior. For example, one source of error in

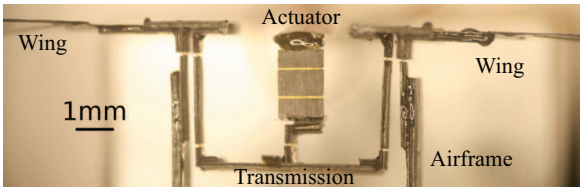

Figure 3.14: Front view of the experimental device.

this experimental trial was off-axis transmission compliance, resulting in measurable deviation of the wings from their mean stroke planes.

3.4.2 Passive body torque regulation

The Drag PARITy design distinguishes itself from the baseline design in the theoretical roll torques imparted by the flapping wings on the airframe. The Drag PARITy is designed to balance the roll reaction torques imparted by both the left (τ^L) and right (τ^R) wings during flapping. Figure 3.11 plots the theoretical roll torques experienced by the body of a FWMAV using a Drag PARITy transmission compared to that experienced by a FWMAV using a conventional baseline transmission described previously. Note that these torques are nominally opposing and that it is their difference, $\tau^L - \tau^R$, that is experienced by the body as a net roll torque. In all three trials, it is apparent that the Drag PARITy transmission has succeeded in balancing the roll torques experienced by the body due to each wing. The results are especially striking in the Uncut trial (Figure 3.11a), where the transmission has passively compensated for fabrication and assembly error present in the nominally symmetric structure.

In the 2-Cut trial, the Drag PARITy can be seen to produce a visible roll torque imbalance. The cause of this imbalance is the existence of a small spring torque within

the transmission which opposes differences in wing stroke angles $\phi^L - \phi^R$. In normal operation, this torque prevents slow drift of the wing stroke midpoint. However, the stroke amplitude difference in the 2-Cut trial is large enough such that this spring torque appears as a net roll torque imbalance on the airframe. The magnitude of this spring torque is an important design consideration, and further details are given in [34].

Another interesting result of this theoretical study is the indirect balancing of yaw torques. Yaw torques, referring to Figure 2.10, result from aerodynamic lift generated by the wings along with inertial coupling due to wing rotation; no yaw torques were generated in previous work incorporating fixed wing rotation [34]. The results for the 1-Cut trial are presented in Figure 3.12. In the drastically asymmetric 1-Cut and 2-Cut trials, use of the Drag PARITy design reduces the large average yaw torque imbalance imparted on the airframe by 71% and 72% respectively. However, in the nominally symmetric Uncut case, the Drag PARITy did not reduce the small average yaw error torque.

This case study has presented further evidence supporting the utility of passive underactuated mechanisms in FWMAVs. The load balancing Drag PARITy transmission has been shown to be compatible with longitudinally compliant wing hinges allowing passive variation of wing angle of attack. The resulting singly actuated four degree of freedom system has been shown to execute stable qualitatively biomimetic flapping wing trajectories well described by the associated theoretical model. Furthermore, the Drag PARITy transmission maintains its load balancing capabilities, passively altering wing trajectories so as to balance roll torques experienced by the

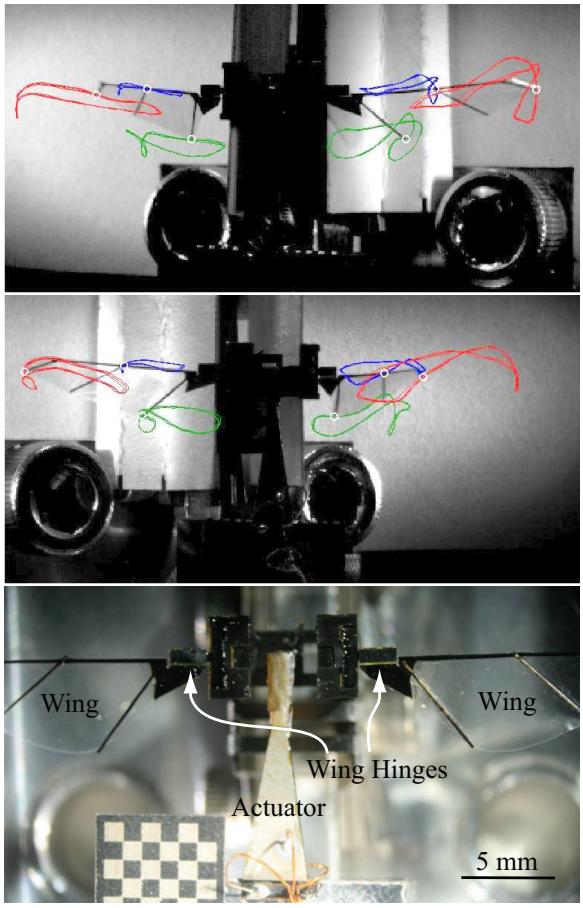

Figure 3.15: Upper images are synchronized frames from the two cameras during the Uncut trial. Tracked points are indicated along with their trajectories over the course of the video. Lower image illustrates the test structure.

FWMAV airframe.

3.5 Conclusion

Two experiments evaluating Drag PARITy performance have been described in this chapter. The first involves the planar two degree of freedom system of a Drag PARITy transmission driving wings with fixed angles of attack, and demonstrates regulation of aerodynamic drag torques. The second allows wing angle of attack to vary, adding two degrees of freedom and demonstrating mechanical regulation of body roll torque on a lift generating FWMAV platform. These experiments rely on an accurate first-principles numerical model of flapping wing dynamics, revealing an ability to operate and evaluate PARITy drivetrain designs.

The manufacturing challenge of building millimeter-scale FWMAV drivetrains using the SCM process not only limits the scope of feasible experiments, however, but also erodes the validity of the underlying claim that active control sophistication should be moved into mechanical and dynamic sophistication. The next chapter addresses these manufacturing challenges by introducing the PC–MEMS manufacturing process. The magnitude of this improvement, discernible through a simple comparison of the mechanisms presented in this chapter to those of the next, allows straightforward implementation of a variety of sophisticated mechanical systems.

Chapter 4

Printed Circuit MEMS

4.1 Introduction: the challenges of mesoscale manufacturing

Complex mechanism designs driven by the desire to incorporate mechanically intelligent features into flapping wing drivetrains lead naturally to practical concerns regarding their manufacture. Modern industry has developed a vast array of conventional techniques to produce machines at the familiar scales of centimeters to meters, often from assembly of large numbers of constituent parts. However, reliance on assembly discourages manufacturing of machines at smaller scales where manipulation becomes burdensome. Recent decades have also seen rapid development in the manufacture of microelectromechanical systems (MEMS), mostly based on silicon wafer processing techniques, with characteristic length scales of millimeters to nanometers and manufactured monolithically. Numerous commercially successful MEMS devices

exist, ranging from accelerometers to pressure sensors to displays, and more intricate devices such as electrostatic motors and miniaturized gas turbines have been created in the laboratory [29, 24, 37, 16]. However, standard MEMS techniques are often inappropriate for producing machines larger than a few millimeters in linear dimension, and cannot easily create complex three dimensional geometries nor integrate a broad palette of materials. Devices with characteristic scales of about a millimeter to a centimeter are difficult to manufacture, existing in the mesoscale gap between conventional manufacturing and MEMS.

One approach to fill this gap is to extend MEMS techniques to larger scales. An autonomous microrobot (Figure 4.1) shows one such attempt, but also serves to illustrate some problems [20, 19]. Materials choice is highly restricted, limiting the performance of mechanical elements. Also, attaining a wide range of three dimensional topologies is difficult, requiring in this case device components to be arranged laterally in plane, increasing device size. Finally, economically efficient production of MEMS devices requires many devices per wafer; an increase in size to the mesoscale erodes manufacturing cost advantages. Figure 4.2 provide examples of mesoscale MEMS devices that experience similar problems.

Another approach to fill the mesoscale gap is to extend conventional techniques to smaller scales. These conventionally manufactured devices can use a wide array of materials in complex topologies. While individual components can be constructed with innovative or MEMS-inspired processes, the assembly process is a manual one. This is the approach taken, for example, both by many mechanical watch developers and by the legacy Smart Composite Microstructure (SCM) techniques to build

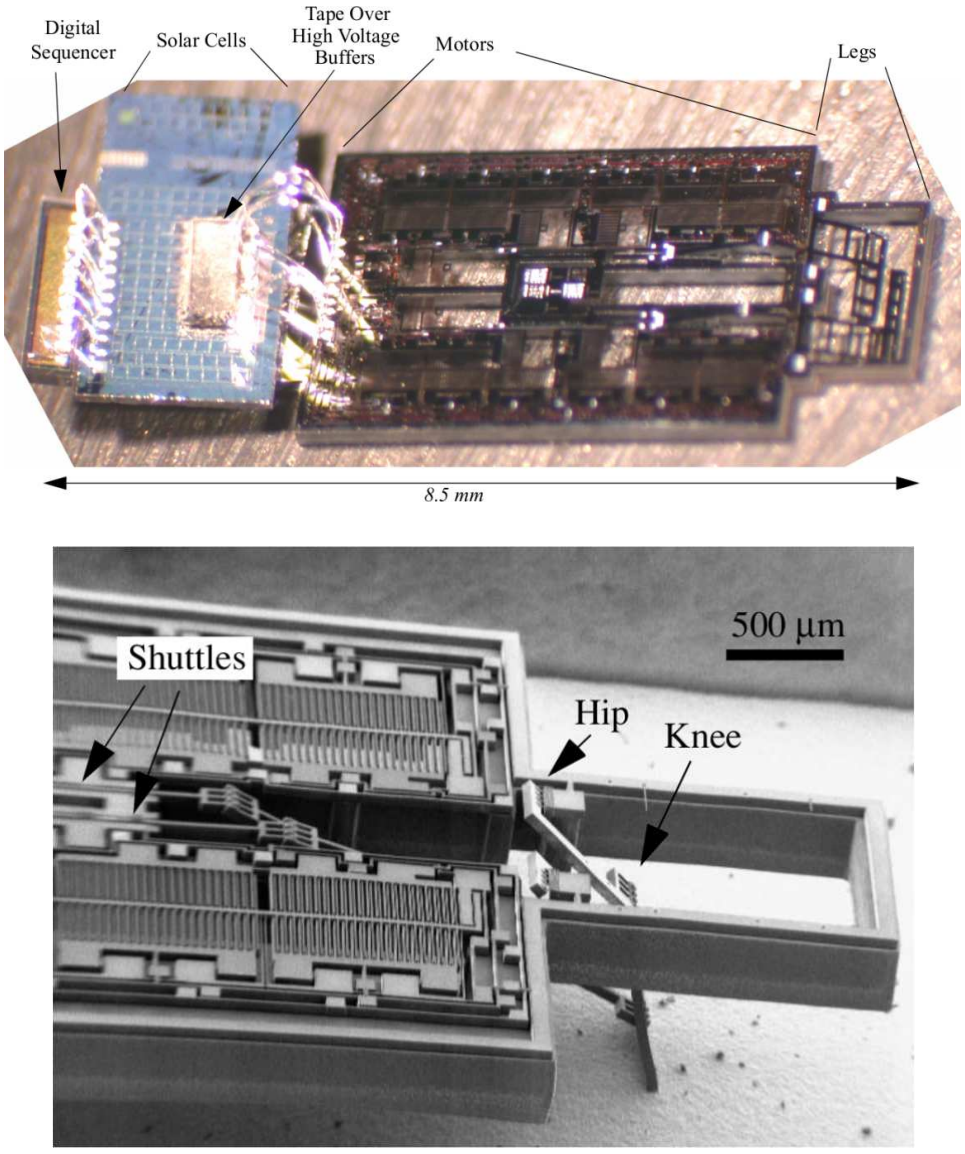

Figure 4.1: A MEMS project to create an autonomous solar-powered Silicon microrobot. Fully three-dimensional topologies are difficult, leading to a large, flat design. [19, 20].

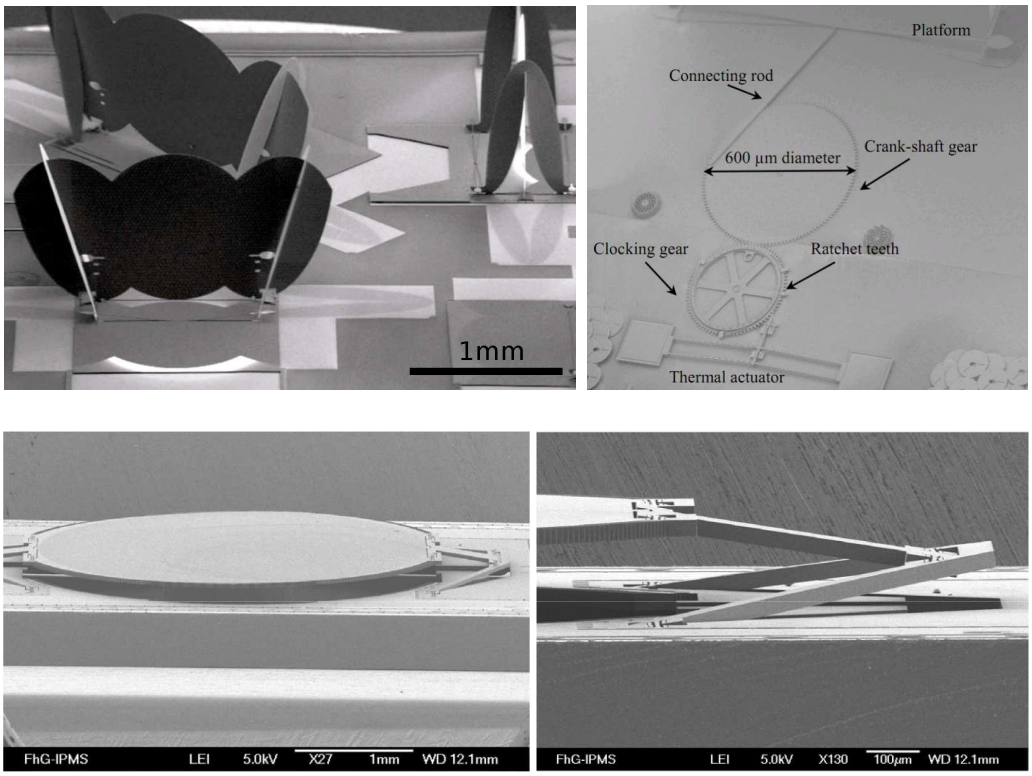

Figure 4.2: MEMS projects to create mesoscale FTIR spectrometers. Tilt-up mirrors (top left) and geared systems driven by a thermal actuator (top right) are key features of this design [10]. (bottom) A project to create a mirror piston motion exceeding 1mm [26].

mesoscale robots [41, 13, 40]. In the case of SCM, accurate device assembly can take months to learn and years to perfect, with a large variance in abilities between individuals. Even for the best assemblers, resulting devices are "artisan" robots, each performing differently from the next.

The overall goal is to create large numbers of 100mg flapping wing robotic insects incorporating complex and accurate mechanically intelligent structures. This requires a mesoscale manufacturing process able to integrate advanced structural materials, actuators, and topologies typical of conventionally manufactured devices with precision more closely associated with MEMS. These challenges could not be met by any existing manufacturing technology, necessitating development of a bulk-machined MEMS process, termed Printed Circuit MEMS (PC–MEMS), for creating mesoscale machines up to several centimeters in dimension. In contrast with conventional MEMS techniques, which arose from integrated circuit fabrication technology, PC–MEMS draws inspiration from printed circuit board (PCB) manufacturing.

4.2 General PC–MEMS capabilities

PCB-inspired lamination has proved to be an effective underlying fabrication process for creating mesoscale MEMS devices such as RF switches [31]. Researchers have also created devices comparable to canonical flat MEMS devices, such as two-axis micromirrors and pressure sensors, at larger scales on laminated substrates [2, 27]. PC–MEMS greatly extends these techniques to incorporate pick-and-place components, 'locking' through wave soldering, scaffold-assisted three dimensional assembly, self-assembly, increased material variety, and integrated actuation, resulting in a manufac-

turing process capable of realizing actuated, fully three dimensional millimeter-scale machines.

PC–MEMS machines can incorporate micron-scale mechanical features, piezoelectric actuators, integrated circuitry, and a wide variety of materials in true three-dimensional topologies. The Harvard Monolithic Bee (Mobee), an exemplary PC–MEMS machine, is a 90mg flapping-wing robotic insect with a 39mm wingspan, a length of 18mm, and an out-of-plane height of 2.4mm. Mobee emerges from the manufacturing process as an actuated, three degree of freedom mesoscale machine. In this section, Mobee's example will illustrate general PC–MEMS capabilities; a detailed description of Mobee manufacturing appears in §4.4

The manufacturing process begins with material layers typically 1μm to 250μm thick and consists of four basic operations: additive lamination, subtractive micromachining, folding, and locking (Figure 4.3). A fifth operation, pick-and-place, allows inclusion of discrete components, such as sensors, actuators, integrated circuits, and other MEMS or PC–MEMS devices, that do not topologically form full layers.

Figure 4.3 provides a schematic overview of the PC–MEMS process, which combines these basic operations with a special attention to controlling mechanical degrees of freedom. A sequence of micromachining and lamination steps fabricates flat multilayer laminates from individual material layers while ensuring that layers and sublaminates remain contiguous for effective alignment during lamination. Combining rigid and flexible materials enables flexure-based mechanical joints for articulated machine components and folding assembly, but these must remain constrained during fabrication. The final fabrication micromachining step releases all folding joints,

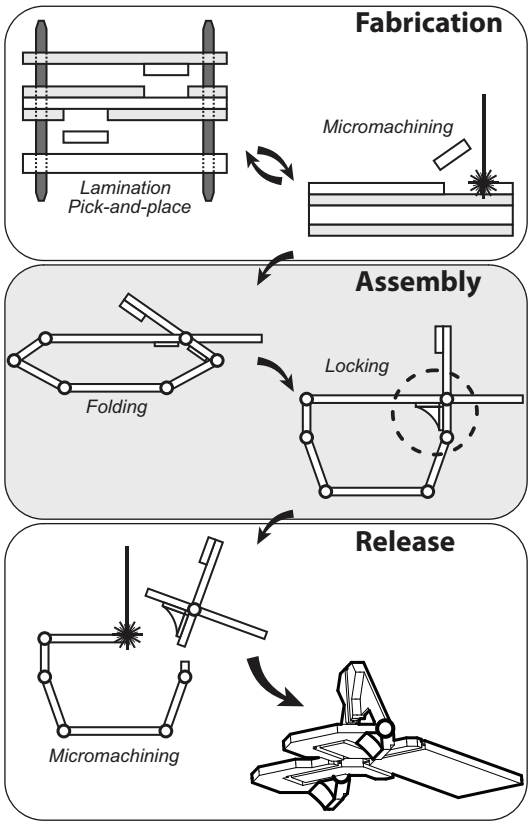

Figure 4.3: A schematic representation of the PC-MEMS process illustrates how the basic operations of micromachining, lamination, pick-and-place, folding, and locking are arranged to manufacture PC-MEMS machines.

which are coupled into a single assembly degree of freedom, allowing three dimensional machines to rise through precise 'pop-up' assembly. Subsequent locking bonds assembled machine components together, removing this degree of freedom and completing assembly. Lastly, micromachining releases all active degrees of freedom of the articulated machine. This methodology allows for parallel manufacture and straightforward assembly of complex three dimensional machines.

A wide variety of materials including metals, plastics, ceramics, and composites are compatible with PC–MEMS. Mobee uses five layers of 100μm carbon fiber reinforced plastic (CFRP) for high stiffness and low mass structural components, one layer of 50μm titanium alloy for finely-featured, high strength wings, and two layers of 7.5μm polyimide film for resilient flexure joints. Two 12.5μm brass layers are involved in the locking process, while two discrete 127μm lead zirconate titanate (PZT) piezoelectric ceramic plates form a bimorph actuator. Other devices have successfully used fiberglass composites, other metals such as steel, copper, and aluminum, and polymer films as thin as 1.5μm. The ability to use a diverse array of bulk high performance materials instead of only those that can be deposited, sputtered, or plated is a key advantage of PC–MEMS. The full gamut of compatible materials depends on the chosen interlayer adhesive and has not yet been determined.

4.2.1 Fabrication

Fabrication begins by processing source material layers with a series of micromachining and lamination operations. Though many micromachining and lithographic techniques are applicable, currently a diode pumped solid state (DPSS) laser micro-

machines individual source material layers, creating complex in-plane features as small as 10μm. To realize out-of-plane mechanical features, a stack of micromachined structural layers are interleaved with similarly processed adhesive layers (Dupont Pyralux FR1500 12.5μm sheet adhesive) for lamination. Inspired by PCB techniques, precision dowel pins provide persistent lateral alignment while heat and pressure applied in a platen press cures the adhesive, creating a multilayer laminate [38]. The resulting laminates may themselves be treated as source material layers, undergoing further micromachining and inclusion as structural layers in subsequent lamination steps.

In contrast with highly serial existing MEMS processes, a large variety of devices can be constructed using only a single additive lamination step. Typically, layers are micromachined individually, laminated in parallel, and the resulting laminate is micromachined again to prepare for folding assembly. Devices with ten structural layers laminated in parallel have been demonstrated, though process limitations on layer count have not been determined. However, printed circuit boards with sixty copper layers are commercially available, implying parallel lamination of more than one hundred structural layers.[1]

Sequential lamination steps can produce a different layer stack at different regions of a final laminate; shown schematically in Figure 4.3, a raised region of one sub-laminate can be inserted into a corresponding pocket in an adjacent sub-laminate. In addition, sequential lamination eases the problem of clearing chips from internal layers after micromachining. By laminating sequentially, these internal layers can be

[1]Sixty layer printed circuit boards can currently be purchased as standard products from Viasystems Group, Inc. of St. Louis, MO, USA and from DDi Corp. of Anaheim, CA, USA, among others.

exposed on the surface of an intermediate sublaminate for simplified micromachining. The preferred Mobee manufacturing process (§4.4) uses two sequential lamination steps to take advantage of both features.

The pick-and-place process extends the capabilities of lamination by allowing inclusion of discrete components and materials unsuited for pin alignment. Two structural layers of Mobee incorporate large pockets bordered by quasi-kinematic mating features and an in-plane flexure spring (Figure 4.30). Discrete PZT plates inserted into these pockets are held in alignment during lamination, resulting in a high power density bimorph actuator [42]. PC–MEMS is compatible with more conventional pick-and-place techniques from the PCB industry, allowing populated circuit boards to be integrated into the mechanical structure (see [7]). This compatibility with PCB techniques parallels the CMOS compatibility of some silicon-based MEMS processes [6].

Incorporation of both flexible and rigid structural layers in a multilayer laminate allows creation of mechanical joints, components commonly used in conventional MEMS [30]. These flexure-based joints enable articulated PC–MEMS machines; Figure 4.5a depicts a four-bar linkage with three flexure joints, used as a transmission to couple the power actuator with Mobee's wings. Figure 4.5d depicts a castellated 'folding joint,' a variant engineered to approximate an ideal revolute joint.

4.2.2 Assembly

After fabrication, the resulting multilayer mechanical structures have intricate in-plane features, but remain flat with limited out-of-plane complexity. This restriction is widespread throughout MEMS; techniques to create truly three dimensional

structures include vastly increasing layer number (3D printing), assembly through origami folding, and various self-assembly techniques [8, 22, 36]. PC–MEMS takes an origami folding approach to assemble three dimensional machines from flat multilayer laminates using a single 'pop-up' degree of freedom.

To minimize the impact of single degree of freedom assembly on the device itself, all mechanical elements that drive assembly are collected into a co-fabricated assembly scaffold surrounding one or more unfolded machines. The assembly scaffold is a mechanical transmission constructed of rigid links and folding joints that couples all necessary assembly folds into a single degree of freedom, which is released by the final fabrication micromachining step. The use of an assembly scaffold eliminates vestigial assembly mechanisms in the final device and allows the creation of structures beyond those highly tailored for 'pop-up' assembly, such as the up-pop prism (§4.3.4) and the Wright Flyer (§4.3.3). Figures 4.5b–c illustrate the functioning of Mobee's assembly scaffold, highlighted in false color in Figure 4.4a.

Mobee's assembly scaffold is based on a Sarrus linkage: two parallel plates surround the device and can be separated in a single translational degree of freedom. Interior linkages, driven by the separating plates, create all necessary assembly trajectories. Though Mobee contains only 90° folds, altering the kinematics of these interior linkages can result in a wide range of folding angles in assembled devices. Figures 4.5b–c also demonstrate a more complex assembly trajectory: the wing translates along a circular arc without rotation. Mobee and its assembly scaffold together contain 137 folding joints linked into one assembly degree of freedom. Twelve additional joints that form a three degree of freedom power transmission mechanism must

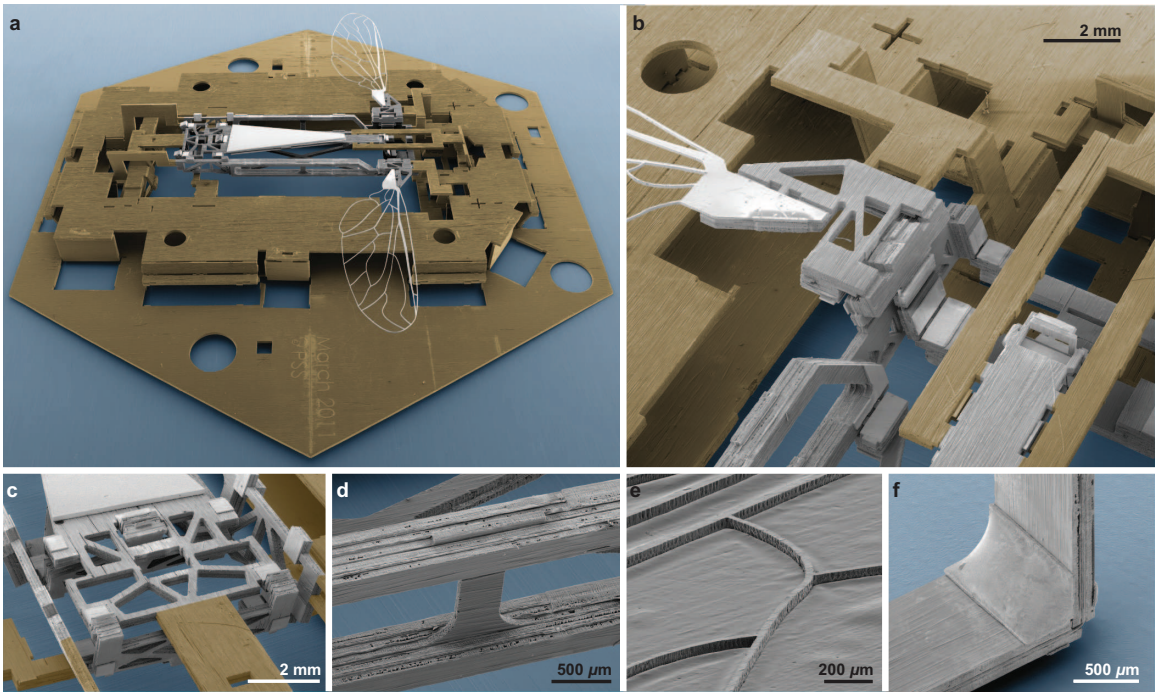

Figure 4.4: Scanning electron microscopy of PC-MEMS structures. All images are presented in false color, used to distinguish the background (blue), the assembly scaffold (gold), and the core machine (greyscale). (a) Mobee in its assembly scaffold after partial pop-up assembly. The hexagonal base has 25mm edges. PC-MEMS devices can have three dimensional, complex topology (b) and incorporate optimized mechanical structures such as (c) box trusses and (d) I-beams. (e) Titanium wing spars support a wing membrane. (f) A solder fillet locks a folding joint.

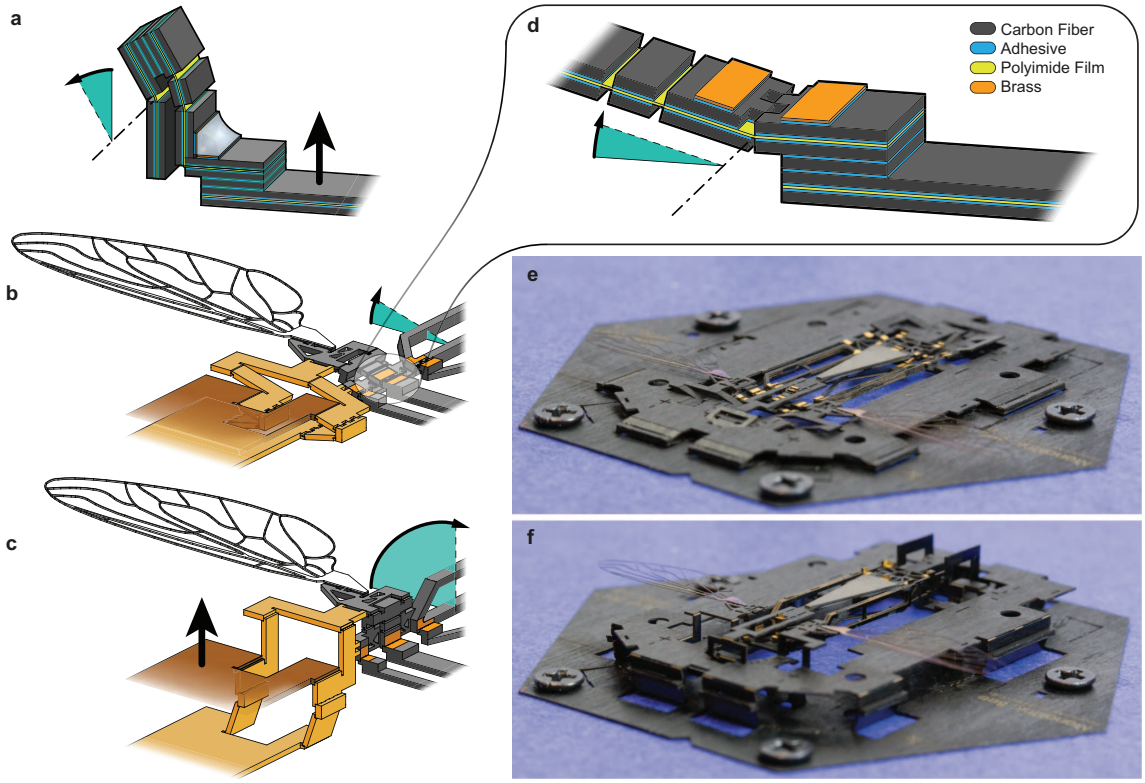

Figure 4.5: Topology and folding assembly of PC-MEMS devices. (a) A four-bar linkage containing three active joints used as a transmission, turning linear actuation into rotational wing motion. (b) Schematic representation of Mobee prior to and (c) after folding assembly, illustrating how the assembly scaffold (gold) drives assembly folds with a single degree of freedom. (d) Castellated folding joints enable precision folding. (e) Mobee prior to and (f) after folding assembly.

remain mechanically constrained during assembly.

Separating the assembly scaffold plates with an external force initiates pop-up folding. Various mechanical parts interfere to form a joint stop, halting motion once folding is complete. Thus, assembly actuation need not be precise, and inclusion of material layers with stored elastic energy has already demonstrated self-assembly of a simple PC–MEMS device (the Up-pop Prism of §4.3.4).

A wide variety of mechanical structures are available to folded PC–MEMS machines. The wing veins (Figure 4.4e) are unsupported titanium beams, some of which have a 30μm$\times 50\mu$m cross section and extend over 7,000μm in length. A box truss (Figure 4.4c) supports the base of Mobee's actuator and twin I-beams (Figure 4.4d) form the airframe; these optimized mechanical structures are usually available only in larger, conventionally manufactured machines.

Folding accuracy fundamentally depends on the determinism of folding joint motion and the stiffness of mechanical elements in resisting torques arising from flexure-based joints. Figure 4.5d illustrates a 'folding joint,' a flexure joint designed to minimize axis drift. Reducing flexure joint stiffness combats deformation of mechanical elements, and joint stops combined with slight overactuation of the assembly scaffold can also aid folding accuracy. Photogrammetric measurement of the box truss of a completed Mobee revealed the assembly fold angle to be 3.7° below its intended value of 90°.

Once the mechanism is folded, removing the assembly degree of freedom through locking completes machine assembly. Various mechanical latching mechanisms have been demonstrated in MEMS folding, but again taking inspiration from PCB manu-

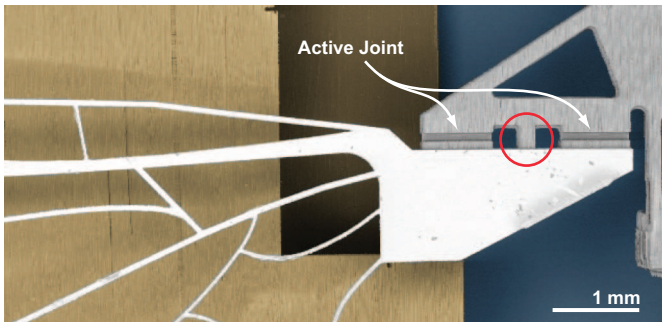

Figure 4.6: Mobee's wing is mounted in series with an active joint. The circled strut mechanically constrains this joint to ensure precision single degree of freedom assembly. This strut is one of several removed by micromachining during release to enable Mobee's three active degrees of freedom. Image presented in false color.

facturing, we have chosen a wave soldering approach [36]. Mobee contains two brass layers forming 52 solder pads. After folding, these pads align at 24 bond points, each consisting of two or three pads meeting at right angles. The entire device is submerged in flux (Superior No. 30) and then in a molten tin-lead eutectic solder. The solder bonds selectively to the brass pads, creating fillets at all bond points in parallel (Figure 4.4f). These solder fillets eliminate the assembly degree of freedom, completing machine assembly.

4.2.3 Release

A final micromachining step releases the machine, concluding a typical PC–MEMS process. Though a PC–MEMS machine can have many active degrees of freedom, the assembly scaffold along with supplemental internal mechanical connections eliminate those degrees of freedom during fabrication and assembly. Figure 4.6 depicts an active

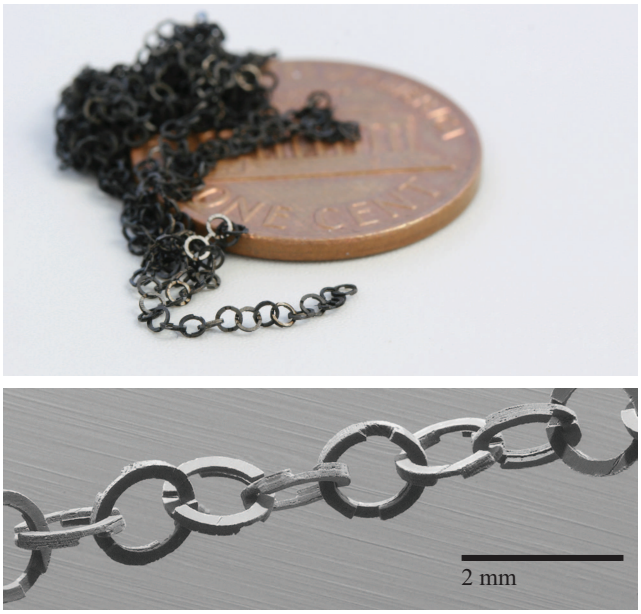

Figure 4.7: A 549 link chain manufactured without assembly.

degree of freedom in Mobee's transmission mechanism constrained by an internal strut. During release, micromachining severs all connections between the assembly scaffold and the machine and removes all internal struts that constrain active degrees of freedom. Mobee has three active degrees of freedom, and the removal of three internal struts allows it to operate as a fully functional micromachine (Figure 4.34).

4.3 Canonical examples

4.3.1 The chain: superplanar topology

The legacy SCM process relies on the adhesive matrix in uncured composite sheets to provide interlayer bonding. Due to the inability to separately pattern the adhesive, SCM laminates are essentially planar objects even though they are constructed from

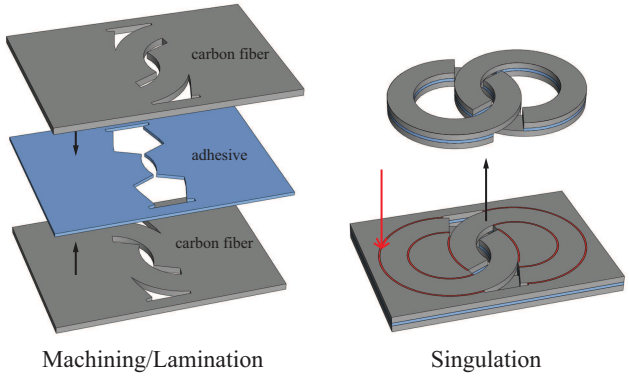

Figure 4.8: The three layer layup used to create the superplanar topology.

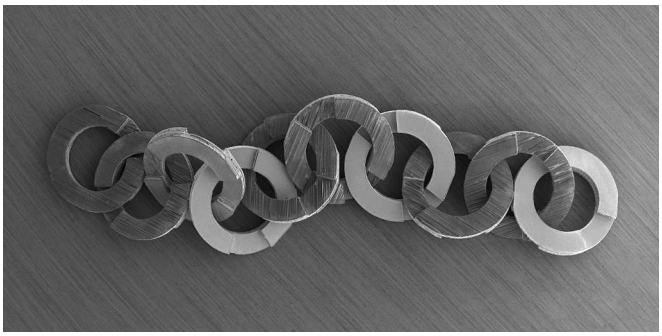

Figure 4.9: A chain constructed from layers of steel and carbon fiber.

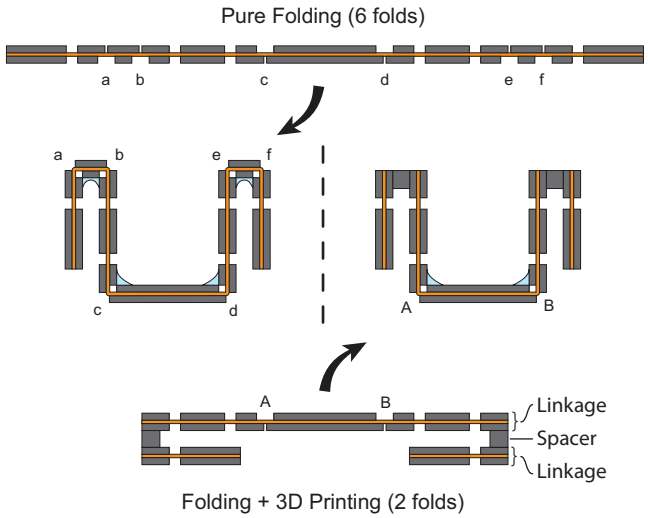

Figure 4.10: (top) A single linkage sublaminate requires six folds to form the transmission linkage. (bot) An improved design uses two linkage sublaminates separated by a spacer, creating a kinematically identical linkage with only two folds.

multiple layers. The layering serves to pattern mechanical stiffness in-plane, but an axis normal to the manufacturing plane will never intersect more than one mechanical element, since all constituent layers must be bonded together.

PC–MEMS introduces a separately patternable adhesive sheet. This allows the ability to create so-called "super planar" topologies, that is, mechanical elements on multiple planes with selective bonding between planes. A monolithically fabricated linked chain is a simple demonstration of the expanded space of accessible topologies.

Figure 4.8 illustrates how a three layer laminate of two structural layers with a single layer of adhesive can form a linked chain by patterning the adhesive layer. Figure 4.7 shows a 549 link chain constructed from carbon fiber. Figure 4.9 illustrates further capabilities of the process through a chain constructed from a seven layer laminate: two layers of steel, two layers of carbon fiber, and three layers of adhesive.

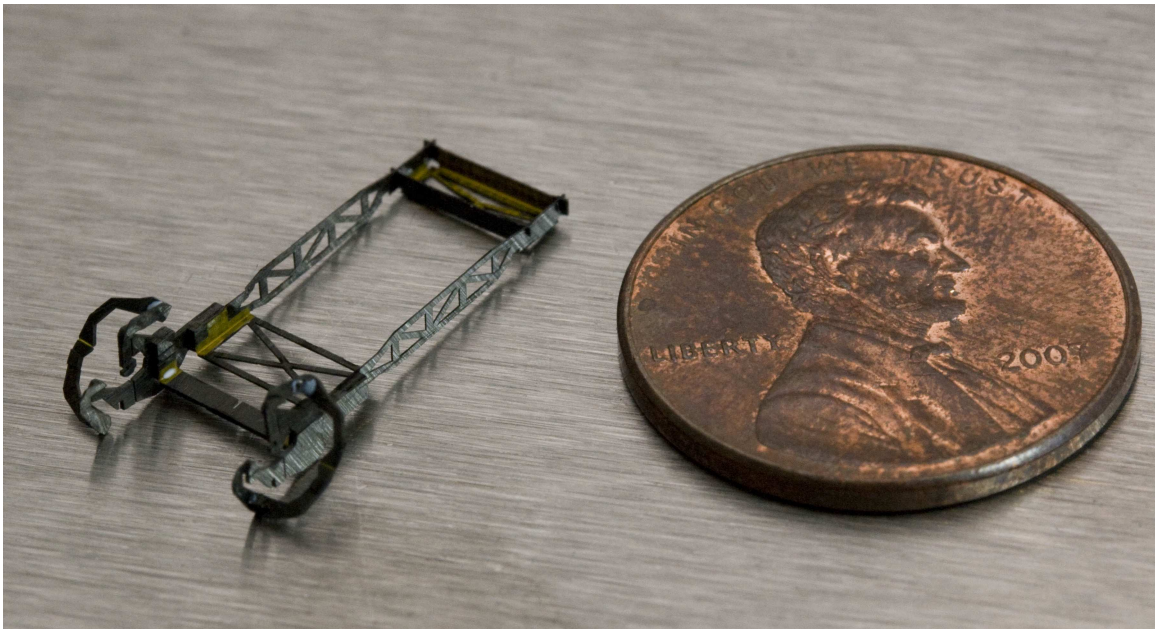

Figure 4.11: Integrated transmission and airframe

Each link in the chain is a laminate of steel and carbon fiber such that steel is exposed on one side of the link and carbon is exposed on the other.

4.3.2 The integrated transmission airframe: simplified assembly

In the legacy SCM process, three-dimensional complexity in a single part could only be obtained through folding. Selective adhesion creating superplanar structures introduces a supplemental technique to achieve three-dimensional complexity within the laminate itself. By vastly increasing layer number, three-dimensional structures can be achieved without folding, the approach taken by 3D-printing technology.

In practice, the ability to both fold and 3D-print allows for more flexibility than reliance on either technique in isolation. Figure 4.10 demonstrates how embedding

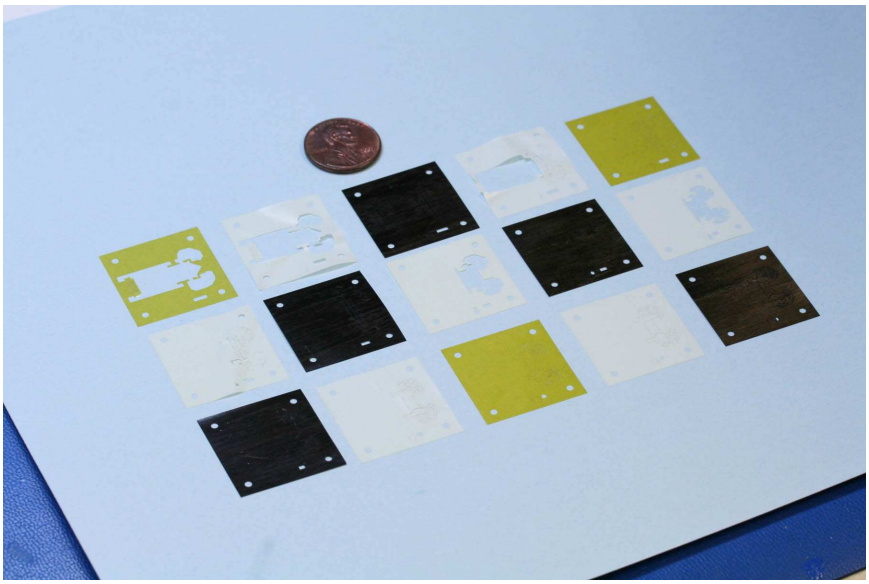

Figure 4.12: The layers used to manufacture the integrated transmission and airframe device.

structure into the laminate itself allows the six folds necessary in an SCM transmission to be reduced to two folds.

Furthermore, the complete device (Figure 4.11) integrates two spherical shoulders of the form of §2.3.3, using the one-fold superplanar design covered in §4.3.7. This device is an early implementation of the Lift PARITy and Dual PARITy designs (see §2.5 for details). Each transmission output drive the wingstroke input of each spherical linkage through the 'drag coupler'. The other spherical inputs, driving wing deviation, contain mating features for a supplemental linkage to form a mechanical structure sensitive to the lift torque imbalance. Further mating features exist to mount wings on spherical outputs.

This integrated transmission design has two primary advantages. First, the transmission itself has greater accuracy: unlike the six-fold design, the two-fold design

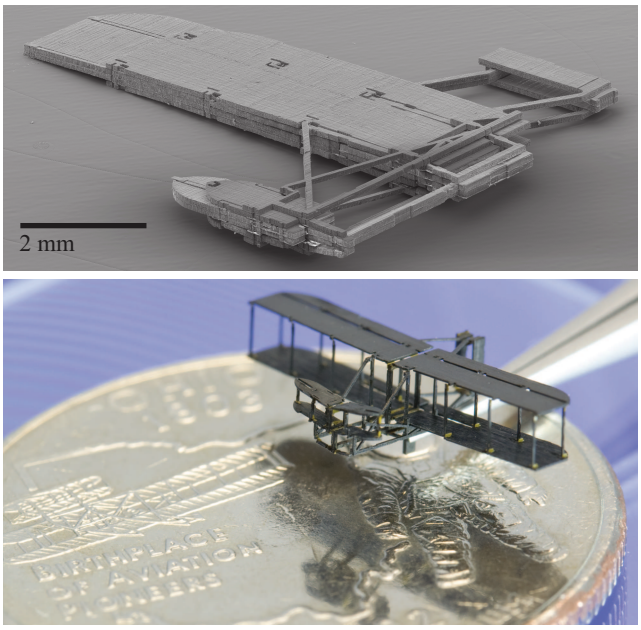

Figure 4.13: The Wright flyer before (top) and after (bot) pop-up assembly.

has a transmission ratio insensitive to folding accuracy, depending instead on the highly deterministic thickness of the central "spacer" layer. Second, the simplified folding allows the transmission to be integrated with the airframe. The integrated system has six assembly folds, but requires external components including wings and an actuator. By combining multiple system components and simplifying folding, the integrated transmission airframe is the first step towards a fully monolithic device.

4.3.3 The Wright flyer: complex topology and tack bonding

The Wright flyer is a demonstration of topological complexity. Furthermore, it uses a rotational degree of freedom for assembly, directly analogous to the pop-up books that inspire single degree of freedom assembly. The device technically has two degrees of freedom, as it is two independent single degree of freedom halves joined at

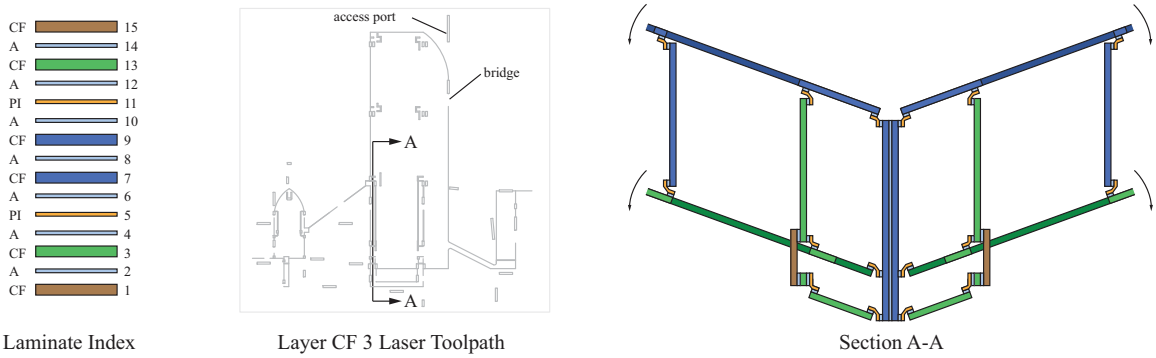

Figure 4.14: Folding in a single motion in the Wright flyer. The structure is two independent halves, each with a single degree of freedom.

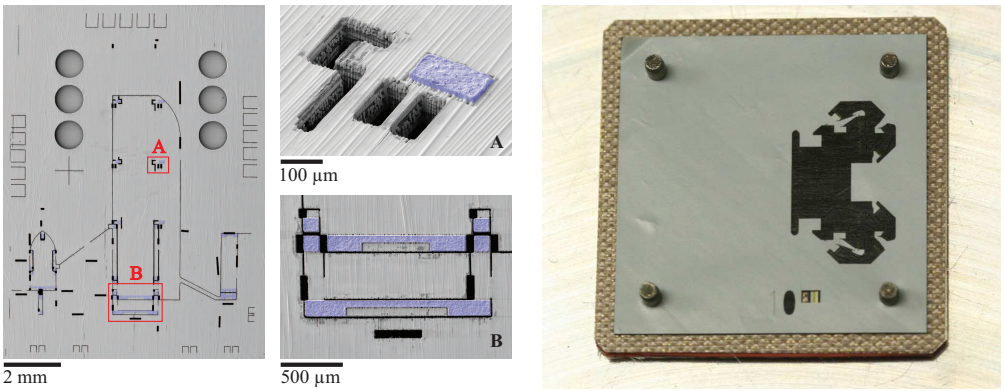

Figure 4.15: (left) A single layer of the Wright flyer with false color tack-bonded adhesive. Insets show an island of adhesive (A) and large rectangular holes called access ports (B). (right) A single adhesive layer in the layup for the device described in §4.3.2 with many cantilevered regions of adhesive, motivating tack bonding.

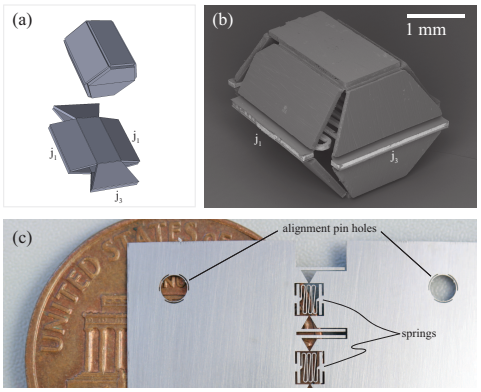

Figure 4.16: (a) A schematic diagram of the up-pop prism folding and (b) an SEM of the up-pop prism. (c) The spring steel layer that is extending during layup, storing elastic energy in the laminate and driving self-assembly. Figure credit: J. P. Whitney

the central plane.

The Wright flyer also demonstrates tack bonding of a sheet adhesive layer. Tack bonding refers to any method that machines the adhesive layer on a supporting carrier. There are two primary methods of tack bonding:

1. The sheet adhesive is machined on a separate carrier with selective laser settings that leave the backing undamaged. Alignment holes laser machined into the carrier allow pin-alignment with a pre-machined material layer. A brief application of heat under pressure causes the adhesive to transfer onto the material layer, allowing the backing to be removed.

2. The sheet adhesive is transferred from a carrier or as a free sheet onto a pre-machined material layer by a brief application of heat under pressure without alignment. Selective laser settings machine the adhesive directly on the material layer.

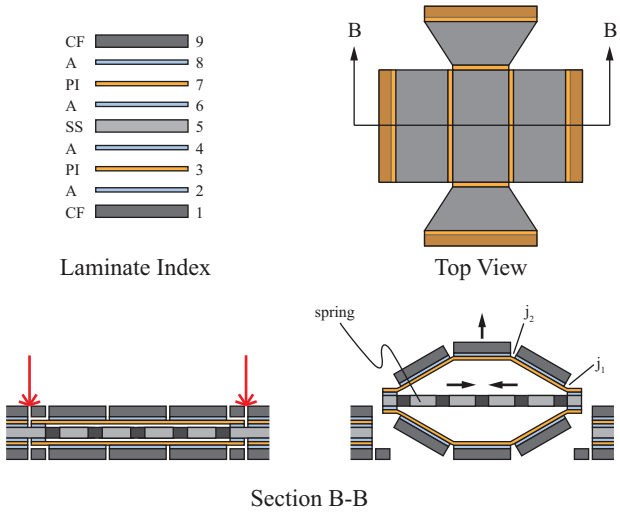

Figure 4.17: The layer stack and cross sections depicting the topology of the up-pop prism. Figure credit: J. P. Whitney

Method 2 requires cumbersome laser realignment and works on a limited selection of material layers as it requires selective machining of adhesive on a material layer. Method 1 is preferred as it machines adhesive on a standard carrier for which selective laser settings are known, uses robust pin alignment, and allows parallel tack bonding of many layers simultaneously. Machining of adhesive on a carrier or on a material layer can either occur by cutting outlines and manually peeling or by rastering.

Figure 4.15 depicts a tack bonded false-color adhesive on a carbon fiber material layer. The isolated islands of adhesive are not possible using pin-aligned free sheet adhesives. Figure 4.15A reveals that Method 2 has been used, as laser machining of the adhesive tacked onto the material layer has slightly damaged the region surrounding the adhesive. Figure 4.15B also reveals access ports, which are the large rectangular holes. These holes allow laser access for micromachinining bridges on internal layers after lamination.

Though assembly is theoretically possible in a single motion, it is extremely difficult as a single hand tremor will destroy the device. The "Biden" fly discussed below shares a similar issue, largely attributable to both of these devices preceding the invention of the robust castellated joint (see Figure 4.25). All joint designs preceding the castellated joint lack robustness in that they easily delaminate and/or only crudely approximate revolute joints with high susceptibility to off-axis motion and axis drift.

The Wright flyer is primarily the work of colleagues J. P. Whitney and K. Y. Ma, with whom the author collaborated.

4.3.4 The "Up-pop" prism: self-assembly

All other devices described here require some form of external actuation for assembly. An interesting consequence of maintaining persistent layer alignment during lamination is the ability to store elastic energy within the layup for self-assembly. In one embodiment, alignment hole locations in a spring steel layer are shifted when compared to their locations in other layers, causing planar springs patterned into this layer to precisely stretch during layup (Figure 4.16c). After release, the device self-assembles into a three dimensional configuration driven by this stored elastic energy. However, due to the singular kinematic configuration during lamination, random noise introduced by ultrasonic cleaning initiates assembly.

The Up-pop prism is primarily the work of colleague J. P. Whitney, with whom the author collaborated.

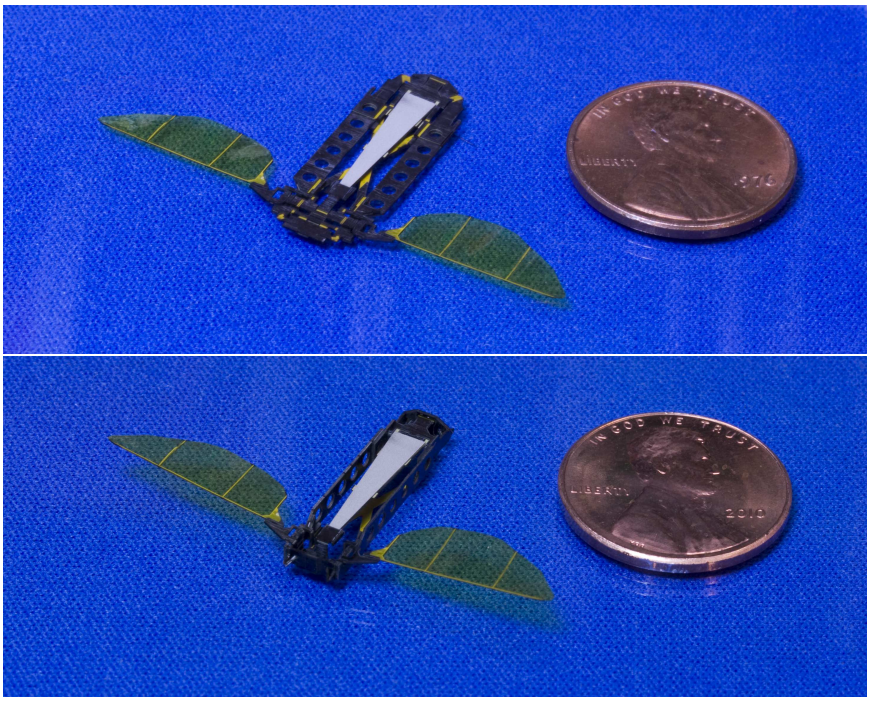

Figure 4.18: Single degree of freedom folding in the Biden fly.

4.3.5 The "Biden" fly: monolithic fabrication and pop-up assembly

The Biden fly is the first prototype deserving of the title "monolithic bee." It incorporates all major aeromechanical components, including an airframe, the actuator, various transmission linkages, and wings, in a single process. Furthermore, all folds within the device are nominally coupled into a single degree of freedom.

The Biden fly is designed around a simple serial folding sequence involving six folds. Small linkages are distributed throughout the interior of the airframe, coupling these folds together. That is, executing one fold would drive the next fold through an internal linkage, which would in turn drive the next fold in a serial manner.

This approach has had only limited success. The small coupling linkages can be

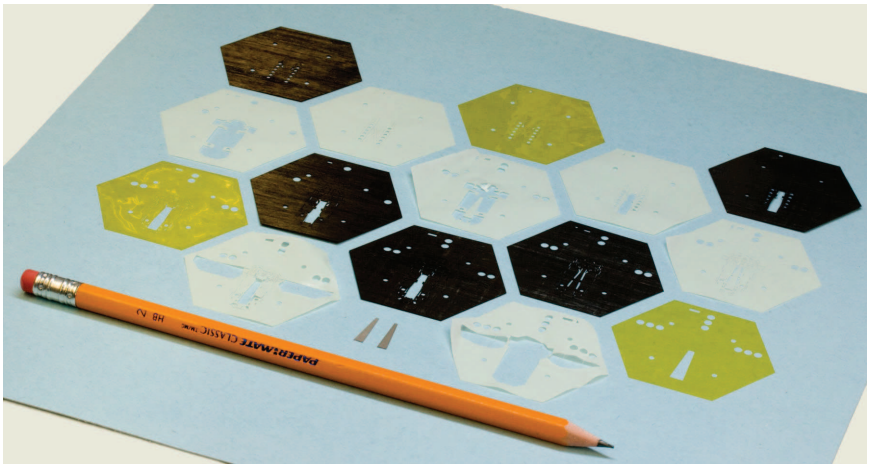

Figure 4.19: The layers used to manufacture the Biden fly.

thought of as an internal assembly scaffold, contrasted with the standard external scaffolds used in subsequent devices. The internal scaffold has competing concerns: robust folding requires scaffold elements to be large, but some vestigial elements cannot be removed from the device after folding necessitating that they be as small as possible. The design also struggles with kinematic singularities: in-plane folds have to assume a specific arrangement of "mountain" and "valley" folds. However, many have equal propensity for either configuration and have to be manually biased before initiating folding. Furthermore, the serial nature of linked folds causes joint compliance errors to accumulate along the kinematic chain. As this design preceded the invention of robust castellated folding joints (Figure 4.25), folding errors were significant.

Internal scaffolding has some potential advantages. Elements are much smaller than their external counterparts, so it provides a solution in cases where material waste is a concern. Robust castellated joints mitigate accuracy concerns. The internal scaffold approach has largely been superseded by the external assembly scaffold,

though potential remains to combine internal and external scaffolding to reduce total device complexity.

Folding the Biden fly is a skill intensive process due to the weakness of internal scaffold elements. The single degree of freedom is an extremely difficult to actuate degree of freedom, requiring several points throughout the device be simultaneously supported to avoid delamination of joints. Furthermore, beads of glue must be manually applied in a microsurgical process to lock the device together after folding. Though much improved over legacy techniques, the process used to manufacture the Biden fly does not achieve precision independent of artisan talent and still relies on some techniques not scalable to large production volumes. All of these problems are solved in the Monolithic Bee prototype, which demonstrates the full PC–MEMS process.

4.3.6 The Icosahedron: assembly scaffolds and complex folding

All other devices described here use relatively simple folding schemes to achieve their final shape. In general, all folds are to 90° and folding joints remain parallel to the planes in which they are fabricated. There are some deviations: the up-pop prism has several 60° folds and the joints in spherical internal scaffold linkages of the Biden fly intersect with their fabrication plane after popup and fold to various angles.

In exploring the capabilities of the PC–MEMS process, questions regarding the space of accessible device topologies arise naturally. Such questions in and of themselves form a full research field related to the mathematical study of origami and will

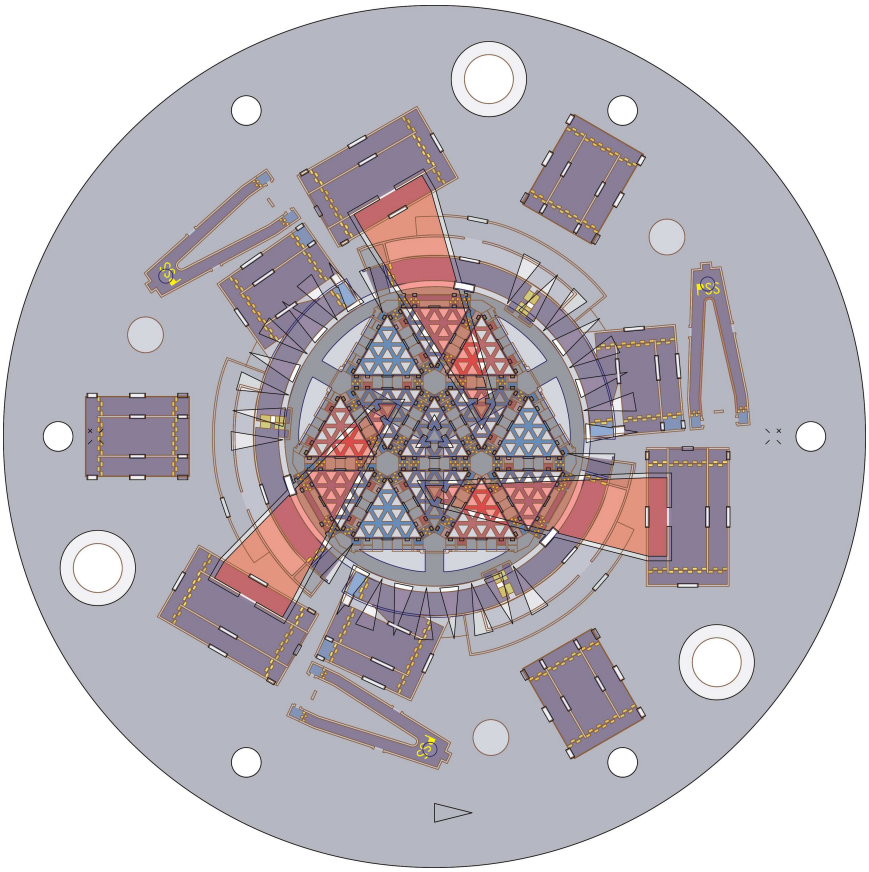

Figure 4.20: CAD design of the Icosahedron.

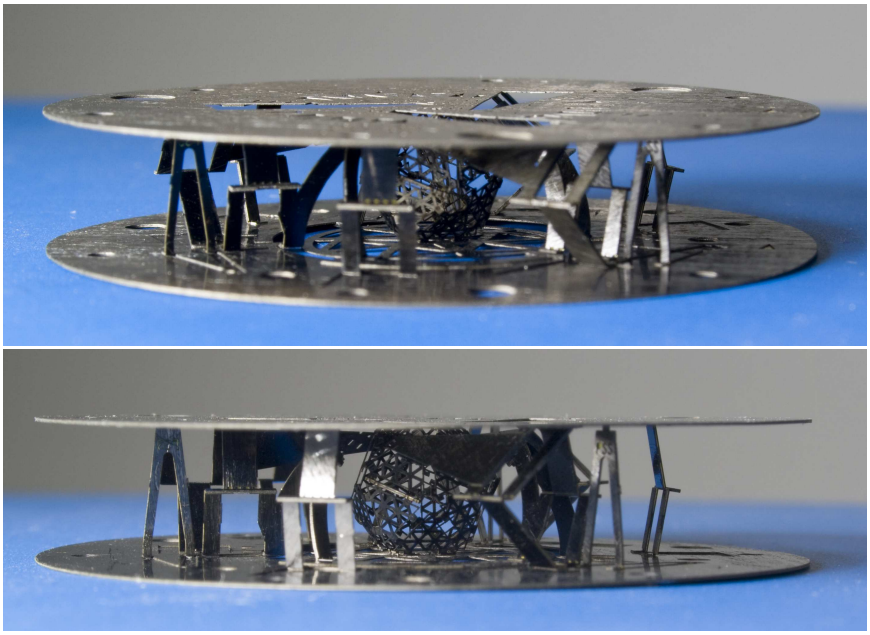

Figure 4.21: A popup icosahedron (top) before and (bottom) after single degree of freedom assembly.

not be addressed in depth in this dissertation. However, successfully completing the complex topological task of folding a spherical shell from a flat laminate suggests a broad underlying capability.

A true cylinder or sphere requires non-localized deformation of mechanical elements, a fertile area for future PC–MEMS research. As the largest platonic solid, an icosahedron serves as a sphere simulant whose structure inspires many conventionally manufactured trussed domes. A PC–MEMS popup icosahedron accomplishes the original goal of demonstrating folding complexity.

The icosahedron is formed from a single linkage layer with a supplemental structural layer adhered to each side, resulting in a nine layer laminate. The linkage layer consists of two rigid layers, but patterned omission of the interlayer adhesive allows

this layer to be split into independent rigid "feature layers." By such splitting, each of these two feature layers form ten single-layer triangular links that form the 20 faces of the icosahedron. The in-plane regions between the triangles contain joints formed from the full linkage layer. In-plane spatial multiplexing allows triangles from each feature layer to be jointed independently, eliminating the need for a second linkage layer.

In the flat configuration after fabrication, two central triangular elements are aligned in-plane, one on each feature layer. Six additional triangles form an eight link kinematic chain connecting one central triangle to the other. Replicating this structure on each of three sides of the central triangular elements creates a 20-link parallel linkage formed from three eight-element serial links sharing their proximal and distal elements. Examining more closely a single kinematic chain formed from the two central triangles and six additional ones, three of the additional triangles extend from the central triangle on each feature layer, creating two independent spherical kinematic sub-chains. These two sub-chains are joined at their distal link through a single non-spherically aligned joint. With one triangle secured, the entire structure has nine degrees of freedom.

In contrast with the small internal elements relied upon for the Biden fly, the popup icosahedron relies on a robust external assembly scaffold. The assembly scaffold constrains the six rigid body degrees of freedom of one central triangle with respect to the other throughout the assembly motion. With the central triangle positions specified, each of the three kinematic chains has one additional degree of freedom bringing the total to nine. The assembly scaffold connects to and determines a folding

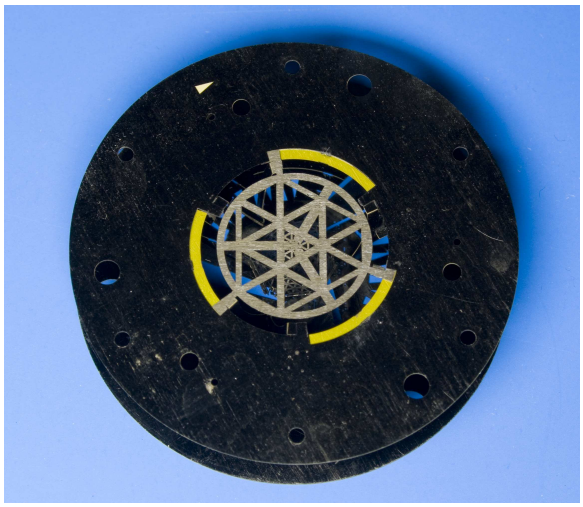

Figure 4.22: Linear bearings incorporated into the layup.

angle for one triangle in each of the three chains, thus fully specifying the kinematic configuration throughout assembly.

The two central triangles remain parallel and centered on an axis through their centers of mass, determining four degrees of freedom. The following assembly trajectories occur in the remaining five degrees of freedom to form an icosahedron of side length s:

1. One central triangle rotates 60° in-plane with respect to the other.

2. The central triangles separate by a distance $1.51s$.

3. A joint proximal to a central triangle in each of the three kinematic chains folds to 41.8°.

The assembly trajectory determined by the assembly scaffold has been carefully designed so as to remain within the configuration space of the kinematic structure. For example, the device is manufactured flat in a singular configuration that allows

no rotation of the central triangle; the assembly scaffold produces the majority of this rotation near the end of the assembly trajectory where it is kinematically acceptable. Candidate trajectories for assembly were chosen heuristically and then verified against a kinematic model of the icosahedron; a successful trajectory formed the basis for the assembly scaffold design.

Design of assembly trajectories and associated assembly scaffolds is not trivial. Ideally, more systematic algorithms will replace the heuristic techniques used here, and eventually become the basis for assistive software tools to support PC–MEMS device design. This work, however, is beyond the scope of this dissertation.

The pop-up folding of the icosahedron also demonstrates that assembly scaffolds not only ease the manual assembly process, but they can execute some assembly trajectories that are not feasible manually. Manual folding of the icosahedron would require anchoring one triangle and grasping four others, driving them simultaneously through independent paths to the final shape. Furthermore, any significant deviation from these paths would exit the configuration space of the linkage and destroy the device. The assembly scaffold creates the necessary assembly trajectories automatically.

4.3.7 The spherical shoulder: robust mass-production

While Figure 4.10 provides a schematic view of the simplified folding afforded by PC–MEMS compared to legacy SCM, the spherical shoulder of §2.3.3 provides a physical demonstration. SCM relies on the adhesive infused in uncured composites to provide interlayer bonding; Figure 4.23 displays a device using a slightly improved

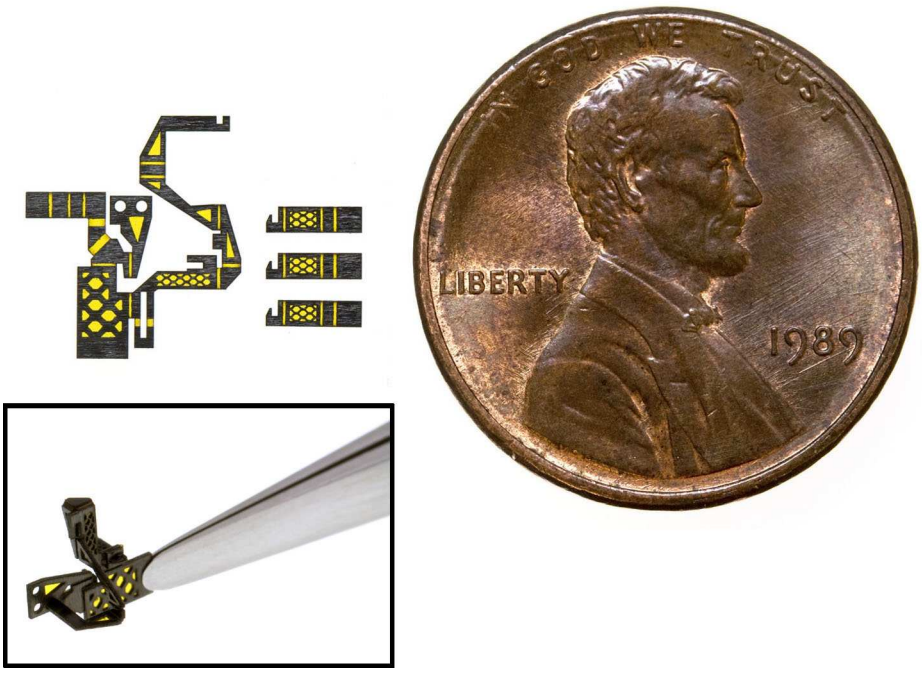

Figure 4.23: A spherical shoulder constructed by manual folding.

method. This improved method uses cured composite layers, shifting the burden of interlayer bonding onto layers of adhesive pre-applied to the surfaces of the central flexible polyimide film layer, typically thermoplastic FEP in the case of heat-sealable films or acrylic in the case of a bond-ply. This technique allows PC–MEMS style pin alignment, an improvement over SCM, but lacks the ability to separately pattern adhesive layers, thus limiting it to the same planar (contrasted with super-planar) topologies accessible by SCM.

The fabricated structure of Figure 4.23 requires three folds for the spherical linkage to assume its final assembled state, shown in inset. Two of these folds have critical accuracy requirements in that inaccuracies of these folds lead to linkage joints no longer intersecting in a point, eliminating all linkage degrees of freedom (seizing the

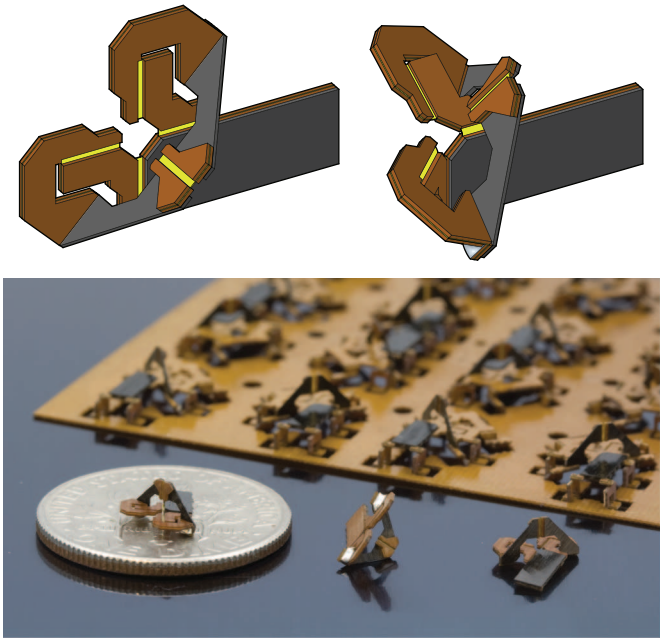

Figure 4.24: (top) A schematic representation of a spherical five-bar linkage in neutral and bent configurations. (bot) Three completed spherical five-bar linkages in front of a larger panel used to mass produce them. A US dime provides scale.

joint). These concerns lead to many tab-and-slot style mating features to ensure accurate folding.

Figure 4.24 shows mass production of a PC–MEMS implementation of the same joint. Here, mechanical features exist on multiple layers demonstrated by differing materials, and a single fold allows the joint to attain its final assembled configuration. Furthermore, this single fold occurs on an axis that also intersects the spherical center, meaning that folding accuracy is not critical: it impacts the kinematic mapping function, but can not cause the joint to seize. The integrated transmission device of §4.3.2 incorporates two of these single-fold spherical joints on transmission outputs.

4.4 The monolithic bee (Mobee)

The Harvard Monolithic Bee (Mobee) is a tethered millimeter-scale robotic insect consisting of a rigid airframe, a piezoelectric actuator, a single degree of freedom power transmission, and two wings. Mobee has a 39mm wingspan, an 18mm length, and an out-of-plane height of 2.4mm. The Harvard Microrobotic Fly (HMF) is a similar aeromechanical system that has demonstrated liftoff under external power [40]. A variety of mesoscale robots, including the HMF, have been created with manufacturing processes reliant on manual folding, assembly, and gluing under a microscope [13, 3, 18]. By contrast, Mobee demonstrates the increased complexity and ease of manufacture afforded to devices constructed using the PC–MEMS process.

Mobee manufacturing is an embodiment of a complete PC–MEMS process, shown schematically in Figure 4.3. Devices are first fabricated from source material layers by a sequence of laser micromachining and lamination steps, the latter able to incorporate discrete pick-and-place components. Articulated flexure joints, created by combining rigid and flexible material layers, form linkages and origami folding elements for assembly. All assembly folds are coupled into a single 'pop-up' degree of freedom, which is locked in place by a soldering process. Finally, micromachining releases the machine by removing the assembly scaffold and all struts that constrain active degrees of freedom.

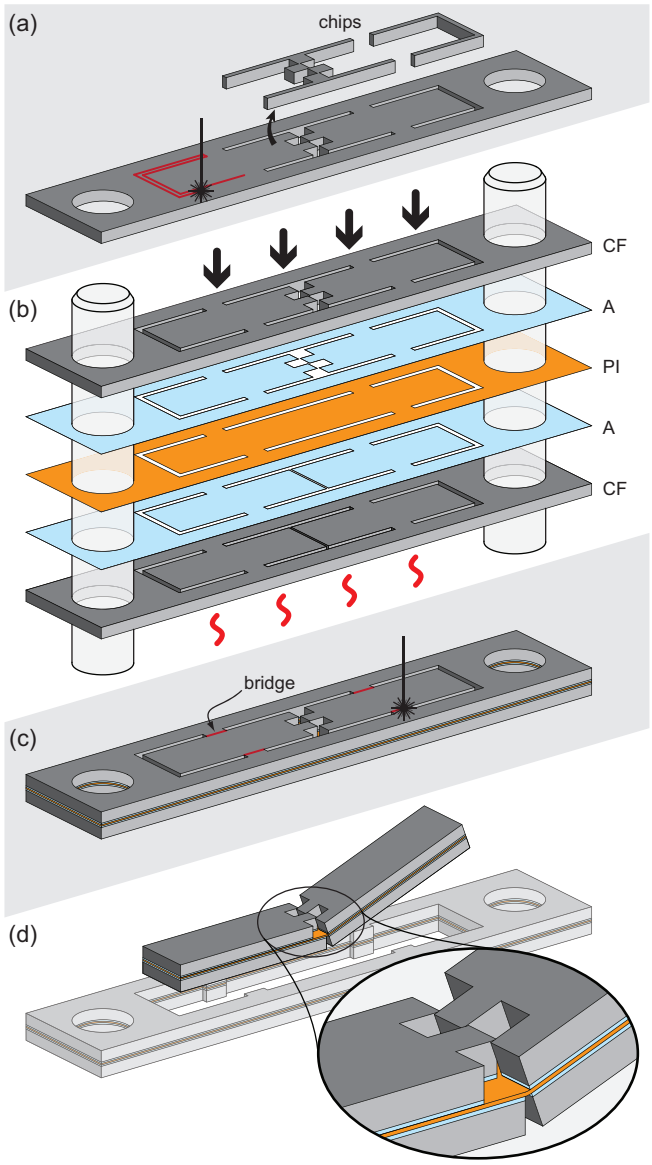

Figure 4.25: Fabrication of folding joints. (a) Individual material layers are micromachined. (b) During lamination, dowel pins align material layers under heat and pressure. Two rigid carbon fiber (CF) layers bonded to a flexible polyimide film (PI) layer with adhesive (A) form a 'linkage sublaminate.' (c) Micromachining cuts mechanical bridges that constrain individual elements. (d) The castellated pattern allows this completed folding joint to approximate an ideal revolute joint.

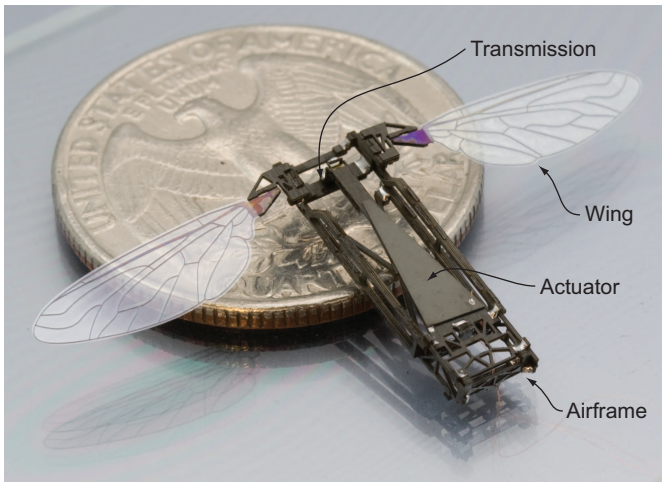

Figure 4.26: A completed Monolithic Bee, with a US quarter providing scale.

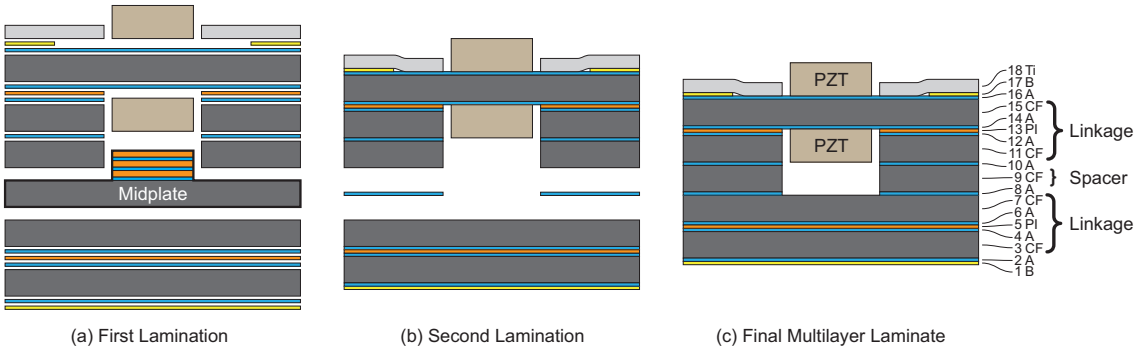

Figure 4.27: Two sequential lamination steps (a) and (b) produce an 18 layer laminate during Mobee fabrication. The midplate is removed after the initial lamination for reuse. (c) Carbon fiber reinforced polymer (CF), polyimide film (PI), Pyralux acrylic sheet adhesive (A), brass (B), and titanium (Ti) form the material layers. Two discrete lead zirconate titanate (PZT) plates are included as pick-and-place components to form an actuator.

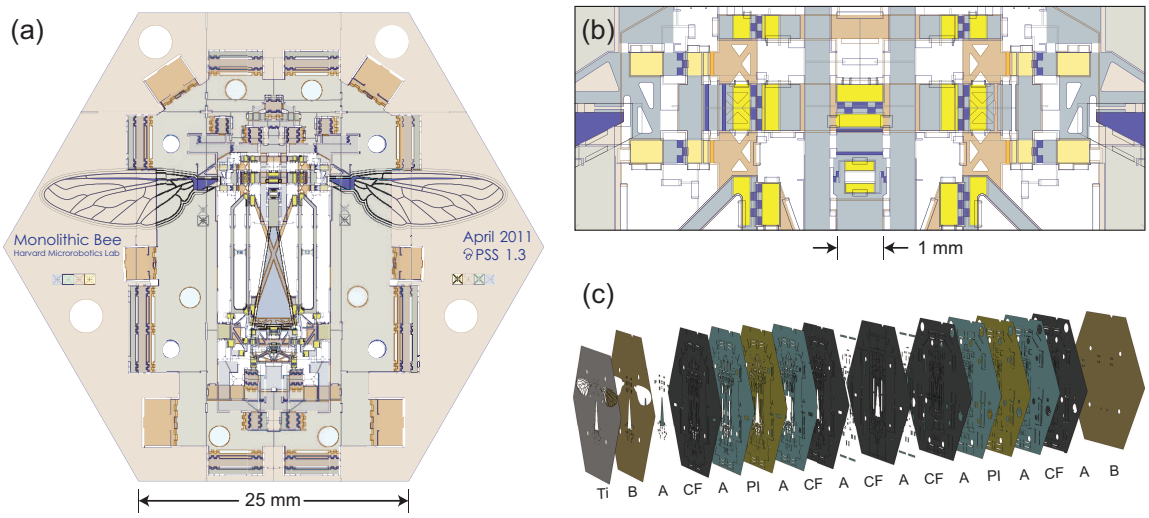

Figure 4.28: (a) Mobee's 18 layer CAD design and an enlarged inset (b) of the transmission region, included to illustrate the complexity attainable by PC–MEMS devices. (c) An illustration of the 18 layer stack, with materials labeled as in Figure 4.27.

4.4.1 Mechanical design

Monolithic manufacturing

The HMF contains eight separate subcomponents: the actuator, airframe, slider-crank, transmission, two wing hinges, and two wings. In total, these subcomponents contain ten active joints to create machine linkages and many folding joints for assembly. Using the Smart Composite Microstructure (SCM) fabrication technique, these eight subcomponents are manufactured separately and individually folded and glued into three dimensional configurations using tweezers under a microscope [41]. The folded subcomponents are then glued together, another manual process requiring skilled artisans.

By contrast, Mobee demonstrates monolithic PC–MEMS manufacturing, relying

only on process steps expected to scale readily to larger volumes. The eight MAV subcomponents are co-fabricated in a single multilayer laminate, integrating a diverse palette of materials including carbon fiber reinforced polymer (CF), polyimide film, piezoelectric lead zirconate titanate (PZT) ceramic, brass, and titanium. Furthermore, the parallel processes of 'pop-up' folding and dip-solder locking replace the manual folding, assembling, and gluing necessary for HMF production. Elimination of all skilled manual steps makes panelized mass production of Mobee a possibility.

Linkage sublaminates

Articulated joints are critical mechanical features, enabling both folding assembly and a power transmission linkage. Two rigid CF layers adhered to a central flexible polyimide film layer form a five layer sublaminate, referred to as a 'linkage sublaminate,' that is capable of realizing flexure-based mechanical joints. Figure 4.25 illustrates the fabrication of articulated joints using a linkage sublaminate. A linkage sublaminate can realize planar arrangements of rigid links connected by flexure joints. These linkages are not necessarily planar linkages, defined to be those in which all joint axes are parallel. Rather, joint axes must be coplanar as fabricated but can be non-parallel, a modified restriction that allows for non-planar linkages such as spherical joints. Mobee incorporates two linkage sublaminates both to support all articulated components and to simplify folding assembly.

The PC–MEMS process provides two methods for realizing three dimensional geometry: layer stacking and folding. Three-dimensional printing and many silicon MEMS techniques rely entirely on the former, while the legacy SCM process, limited

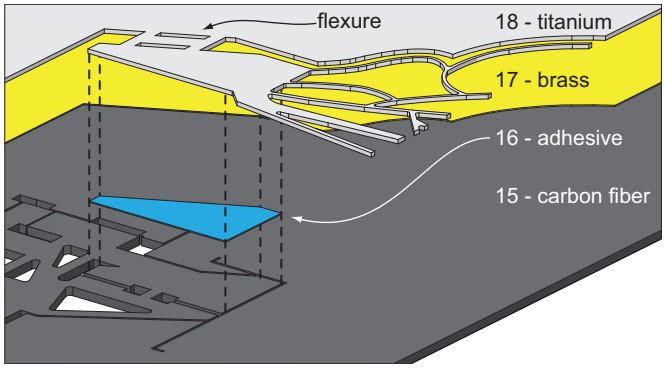

Figure 4.29: An illustration of layer sharing. The titanium flexure bends during lamination, allowing the wing to descend into a hole cut into the underlying brass layer. Thus, titanium and brass share a single layer, each bonding directly to the carbon fiber.

to one linkage sublaminate, relies entirely on the latter. Examples of SCM folding for microrobot manufacturing as well as MEMS layer stacking can be found in related literature [41, 24]. Mobee uses a combination of folding and layer stacking to realize three dimensional structures in a simpler fashion than can be attained by either method alone. For example, the HMF's SCM transmission uses six assembly folds. However, by stacking two linkage sublaminates, two folds result in Mobee's kinematically identical mechanism (Figure 4.10). Conversely, a pure three-dimensional printing approach requires a high layer count, can be wasteful in creating open trusses, and may struggle with structural anisotropy. Combining folding and layer stacking is not a unique capability of PC–MEMS: existing silicon MEMS techniques also incorporate folding for three dimensional assembly [30].

Optimized structures

Mass is critical concern for MAVs, requiring Mobee to contain optimized mechanical structures normally available only in larger scale machines. Trusses are particularly straightforward to construct using PC–MEMS, allowing Mobee to achieve a total system mass of 90mg. Referring to Figure 4.26, a box truss supports the base of the actuator, containing mechanical elements on all six faces. Twin I-beams extend from this truss to support the transmission ground, a geometry that maximizes airframe stiffness under mass constraints. Other trusses reinforce the wing mounting area against flight forces.

Unsupported titanium beams as small as 20μm wide and 50μm thick extend up to 7,000μm to form a venation structure supporting Mobee's wings. The vein pattern mimics that of the bee fly (family *Bombyliidae*), though no profound aerodynamic understanding underlies this choice. Similar to those of biological fliers, these biomimetic wings have varying stiffness across their area, providing a potentially useful platform for the study of aeroelasticity in flapping wing flight.

4.4.2 Fabrication

Source Material Layers

Mobee contains eight adhesive layers and ten structural layers, constituting 18 distinct material layers (Figure 4.27). Five 100μm layers of CF are the primary structural material for its high stiffness to weight ratio. Each CF layer is itself a cured three layer stack of unidirectional carbon fiber pre-impregnated sheets (Tencate XN-50A-RS3C), aligned in a 0-90-0 layup. Two 7.5μm polyimide film layers allow

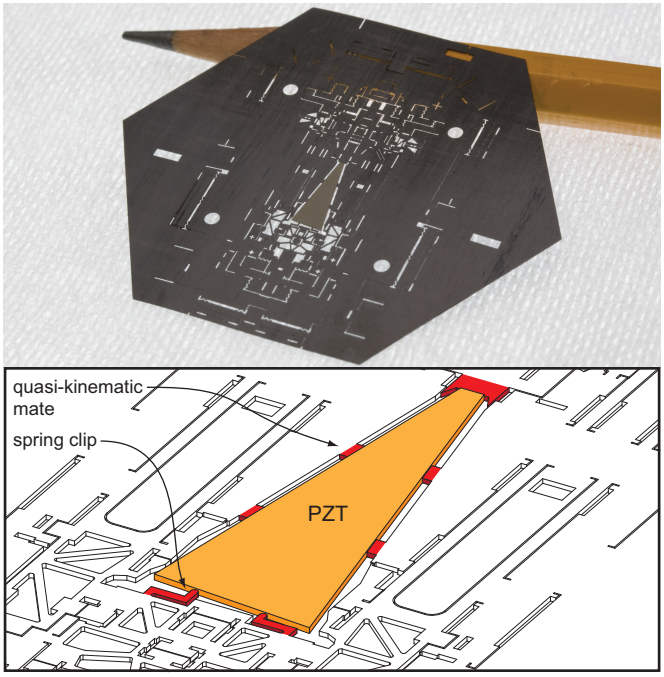

Figure 4.30: (top) Carbon fiber layer 15 after micromachining. Four circular holes accept alignment pins, and a centrally located pick-and-place piezoelectric plate is held in alignment. A wooden pencil provides scale. (bot) Quasi-kinematic mating features and planar spring clips machined into the carbon fiber material layer hold the PZT plate in alignment.

resilient flexures for mechanical joints, while solder pads, important for assembly, are created from two layers of 12.5μm brass. A single layer of 50.8μm grade 9 Titanium alloy layer enables biomimetic, high strength wing venation patterns. The remaining eight layers are DuPont Pyralux FR1500 12.5μm acrylic sheet adhesive.

Using a diode pumped solid state laser, all structural layers are micromachined with complex cut patterns as well as precision alignment holes (see Figure 4.30). The cut patterns ensure that all layers remain contiguous, and that each mechanical feature maintains a robust connection to the surrounding alignment holes. This is typically accomplished by leaving all mechanical elements in a layer attached to the surrounding bulk material by small 'bridges' that will be severed in post-lamination micromachining (Figure 4.25). Structural layers are ultrasonically cleaned and then exposed to an oxygen plasma to promote bonding during lamination. In addition, the titanium foil is clamped flat and stress relieved at 550°C for one hour, a post-processing step that eliminates curvature induced by micromachining.

Similar to the structural layers, the adhesive can be micromachined as a free sheet (layers 4, 6, 12, and 14), but it must likewise remain contiguous. Alternatively, the adhesive can be micromachined after being tacked directly onto a structural layer (layers 8 and 10) or onto a temporary backing and subsequently transferred (layer 2), allowing arbitrary disjointed adhesive patterns [38]. Adhesive layers are interleaved with structural layers and laminated in a heated platen press (200°C at 340kPa for 1 hour) to create a multilayer laminate. Similar to PCB fabrication, precision dowel pins provide persistent lateral alignment during lamination.

Figure 4.27 provides a cross-sectional view of Mobee's multilayer laminate after

fabrication. Mobee's core mechanical structure consists of two linkage sublaminates (layers 3–7 and 11–15) bonded to a central 'spacer' layer (layer 9), which provides a well-defined separation between the two linkage planes. Two brass layers (layers 1 and 17) allow solder pads to be created on the external faces of the two linkage sublaminates.

A final structural layer of titanium (layer 18) forms the wing venation, but lacks an underlying adhesive layer. Demonstrating a 'layer sharing' technique, the titanium venation structure is cantilevered across an aperture in the underlying copper layer (layer 17), and engages with adhesive layer 16 to bond directly to CF layer 15 (Figure 4.29). Layer sharing is one of several techniques used to alter the layering composition across regions of a multilayer laminate.

Pick-and-place

Another such technique is the pick-and-place process, allowing the inclusion of discrete piezoelectric plates that are too brittle for effective pin alignment as a full layer. These plates form Mobee's actuator, which is a bimorph cantilever consisting of two 127μm nickel-plated lead zirconate titanate (PZT) piezoelectric plates (PSI-5H4E, Piezo Systems, Inc.) bonded to a central CF layer. Though created by substantially different manufacturing processes, the resulting actuator is similar to those created by [42], differing only in that Pyralux acrylic replaces a cyanate ester for interlayer bonding.

Discrete plates are laser-cut from the source PZT sheet, which has first been sputter coated with a thin layer (approximately 350nm) of chromium to provide protection

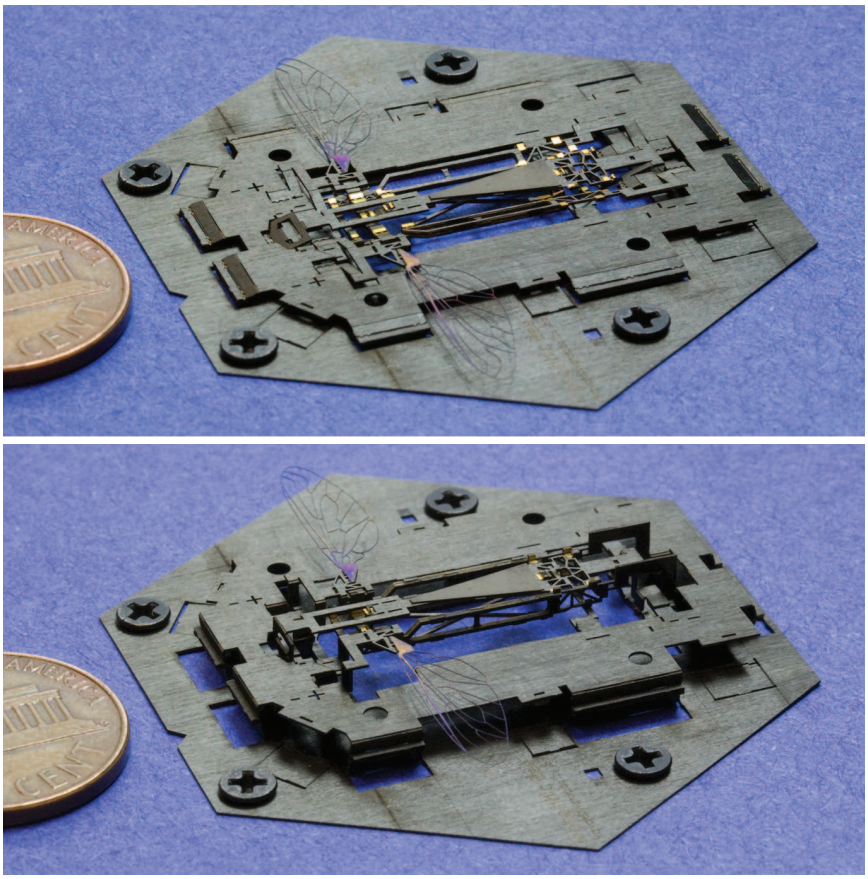

Figure 4.31: Pop-up assembly. Mobee is flat after fabrication (top). Separating the assembly scaffold plates (bot) executes pop-up assembly. A US penny provides scale.

during the downstream locking process. Cutouts micromachined into successive material layers create two internal cavities within the layup into which these discrete plates are placed while the layers are stacked for lamination. Quasi-kinematic mating features and planar spring clips in CF layer 11 and titanium layer 18 hold each plate in alignment during lamination, accommodating small mismatches in thermal expansion (Figure 4.30).

Sequential lamination

Though a single step lamination process has been demonstrated, a process with two sequential lamination steps is preferred for two reasons: it is a third technique for altering layering composition and it eases the problem of chip removal. A separate PC–MEMS structure called the 'midplate' is included to alter the layer stack underneath the PZT plate during initial lamination then removed, allowing precise accounting for the plate's thickness (Figure 4.27). The corresponding single step process requires discrete shims underneath the PZT plate to accomplish this. In addition, machining steps often create unwanted material regions, or 'chips,' which must be physically removed (see Figure 4.25). When the spacer layer 9 is micromachined after initial lamination, all chips from micromachining can easily be removed from the exposed surface. Post-lamination machining in a single step process results in trapped chips that must be highly engineered to enable physical removal from the internal spacer layer.

Referring to Figure 4.27, all layers and the discrete PZT plates are stacked and laminated save for adhesive layer 8, which is replaced by the midplate. The midplate

is a simple reusable PC–MEMS laminate consisting of a flat CF plate containing alignment holes and a central polyimide film boss designed to support the lower PZT plate. This initial lamination results in two sublaminates, the lower sublaminate consisting of layers 1–7, and the upper sublaminate consisting of layers 9–18 and two PZT plates. Adhesive layer 8 is tacked to the lower sublaminate and micromachined, while the upper sublaminate is micromachined to sever mechanical bridges on spacer layer 9. After chips are removed from layer 9, these two sublaminates are stacked and laminated together. A subsequent micromachining step on the final 18 layer laminate removes all remaining bridges, preparing the structure for assembly.

Post-lamination micromachining creates the need for another feature called an 'access port.' Machining a bridge on an internal layer requires a method of accessing that internal feature for micromachining. In its simplest form, the access port is simply a small horizontal region devoid of important features on all material layers between the internal bridge and an external surface of the laminate, with the understanding that micromachining will not only destroy the bridge, but all material between the bridge and the surface as well. In the case of a micromachining system with limited penetration, the access port is a physical opening in all material layers between the internal bridge and the surface, allowing access for the micromachining system to surgically remove the internal bridge through this stack of physical openings.

4.4.3 Assembly

Pop-up folding

As fabricated, Mobee is a flat multilayer laminate with limited three dimensional structure. Its components must undergo a variety of assembly trajectories to realize the final fully three dimensional topology. A co-fabricated mechanical transmission called an 'assembly scaffold' couples all of these assembly trajectories into a single degree of freedom. Mobee emerges from the manufacturing process as a three degree of freedom machine, but internal mechanical connections eliminate these active degrees of freedom during assembly. The resulting mechanism uses 137 folding joints to assume a fully three dimensional topology in one motion, similar to those created by paper folding in pop-up books (Figure 4.31).

Mobee's assembly scaffold consists of two parallel plates, one constructed from each linkage sublaminate, coupled mechanically to form a Sarrus linkage. These plates surround Mobee's mechanical components and are constrained to a single linear degree of freedom separating the plates along their normal axes. Interior linkages, driven by plate separation, are connected to each of Mobee's core components to realize all desired assembly trajectories (Figure 4.5b-c). The Sarrus linkage assembly scaffold provides a versatile framework to produce diverse assembly motions coupled together into a single degree of freedom. Rotations to a wide range of angles about any axis in a linkage plane can be achieved through an appropriately designed interior linkage. Mobee also incorporates more complex interior linkages to translate the wings and the actuator along three separate arcs without rotation during folding assembly.

One plate of the assembly scaffold is secured to an external jig, which drives six

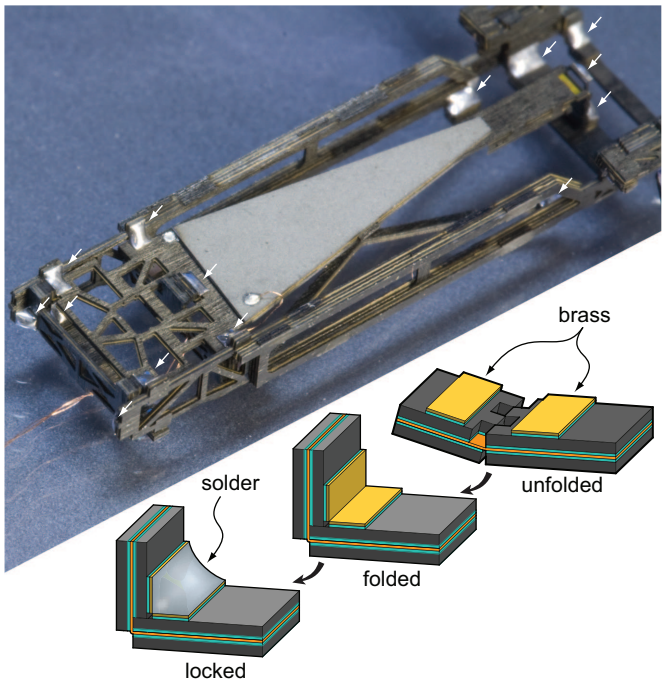

Figure 4.32: (top) A close-up of Mobee with locked bond points indicated with arrows. (bot) Folding and locking of a simple folding joint.

dowel pins through clearance holes in the secured plate to separate the opposing plate. Separating the scaffold plates initiates single degree of freedom folding assembly, causing Mobee's components to assemble into their final three-dimensional configuration. Various mechanical elements interfere upon completed folding, creating a joint stop. Tabs in one scaffold plate are folded manually and inserted into slots in the opposing plate, creating support pylons that hold the assembly scaffold in its folded state, allowing it to be removed from the external jig.

Folding accuracy using these techniques has not been precisely quantified. Mobee uses castellated patterns, illustrated in Figure 4.25, to limit the length of the flexure joint to 20-40μm. A short flexure length limits rotational axis drift as well as off-axis motion, at the cost of increased material stress. A contributor to folding inaccuracy is bending of nominally rigid mechanical elements under torque generated by the folding joint flexures, especially under the magnified forces experienced near kinematic singularities. Special care has been taken to move Mobee's fully folded configuration away from kinematic singularities. In addition, the use of joint stops allows the assembly scaffold to be slightly overactuated to ensure complete folding.

Locking

Mobee contains 52 brass pads distributed across outer surfaces of its linkage sublaminates. After folding, pads on disparate links align into 24 'bond points,' consisting of either of two pads meeting at right angles or three pads forming the corner of a cube. The structure, held in its folded state, is submerged in a water soluble flux (Superior Supersafe No. 30) and then pre-heated in an oven at 100°C for 10 minutes.

It is then submerged in 260°C tin-lead eutectic solder for approximately 1 second. Finally, the structure is ultrasonically cleaned in distilled de-ionized water to remove the water-soluble flux residue. The result of this soldering process is the formation of solder fillets at all bond points, eliminating the assembly degree of freedom and locking all disparate machine components together (see Figure 4.32).

Partial release

Referring to Figure 4.4a, the surrounding assembly scaffold connects to the centrally located robot in eleven locations, all exposed for micromachining. Severing all connections between the assembled machine and the scaffold releases Mobee. The assembly scaffold is then discarded.

However, in addition to assembly scaffold connections, Mobee contains three internal struts that constrain its three active degrees of freedom. A typical release step entails the removal of these struts, but Mobee is only partially released, allowing these struts to remain in place. By grounding the transmission mechanism, these struts constrain Mobee to be a rigid object, able to be precisely aligned as a pick-and-place component.

4.4.4 Second pass

After the first PC–MEMS manufacturing pass, Mobee has two titanium wing venation patterns that are missing wing membranes. Wing membranes are not included during initial fabrication due to the difficulty in manufacturing a lightweight membrane capable of withstanding substantial forces and temperatures typical of dip-

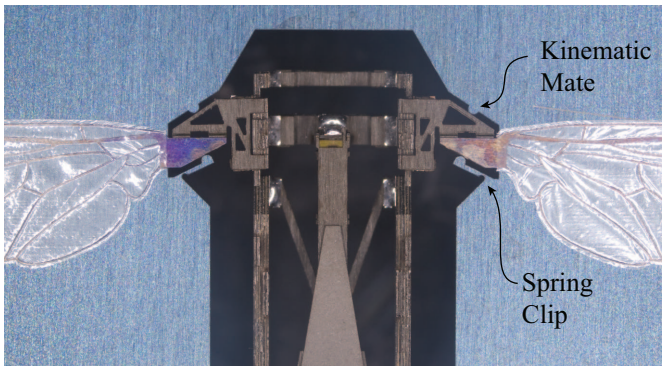

Figure 4.33: Spring clips in a spring steel plate align an entire PC–MEMS structure as a pick-and-place component. This allows wing membranes to be applied to Mobee's wing venation patterns in a second manufacturing pass.

soldered locking. The solution is a second PC–MEMS manufacturing pass, omitting assembly, to apply membranes onto the wing veins.

A new lamination stack accepts the fabricated, assembled, and partially released Mobee as a discrete pick-and-place PC–MEMS device, analogous to the inclusion of discrete piezoelectric plates in the initial manufacturing pass. A micromachined 76.2μm spring steel shim (Figure 4.33) incorporates kinematic mating features that engage with geometry near Mobee's wings, holding the discrete PC–MEMS device in alignment. The lamination stack places Mobee's wing venation patterns between two layers of micromachined 1.5μm polyester film. This lamination step does not use separate adhesive layers; instead, the thermoplastic properties of the polyester film causes them bond together during lamination (120°C, 340kPa, 15mins).

A final micromachining step cuts the outline of the wing membrane, completing wing fabrication. In addition, this step fully releases the device by removing the three internal struts that constrain Mobee's three active degrees of freedom.

4.4.5 Operation

After the manual attachment of three wires to the piezoelectric actuator, Mobee is ready to operate. Applying an oscillating voltage to the piezoelectric actuator causes reciprocating flapping motion of the wings (Figure 4.34). As a completed machine, Mobee is constitutively identical to the HMF; it distinguishes itself primarily by the precision and scalability of the manufacturing process used to produce it.

Though Mobee's manufacturing precision exceeds the manually assembled HMF, design issues limit Mobee's operational performance, preventing it from replicating the HMF's liftoff demonstration. The largest problem is Mobee's resonant operating frequency of 30Hz, far less than the 100Hz HMF operating frequency. This problem can be attributed to several design parameters including wing size and inertia, kinematic transmission ratio, and actuator performance. In addition, poor understanding of the limits of the PC–MEMS manufacturing process led to conservative design decisions; a more aggressive mechanical design has the potential to significantly reduce Mobee's mass. Achieving tethered liftoff, however, was only a peripheral goal of this initial Mobee design: flight capability has already been demonstrated by the closely related HMF.

4.5 Challenges

4.5.1 Chip removal

Chip removal is the largest fundamental challenge limiting the PC–MEMS process. Reliable bonding requires near-uniform application of pressure during lamina-

Figure 4.34: A completed Mobee (top) on a US penny and a composite image (bot) demonstrating flapping motion under an applied sinusoidal voltage to the piezoelectric actuator.

tion. Thus, removal of large regions of source material layers during micromachining must be avoided without careful evaluation of its impact on pressure transmission through the laminate. These large scrap regions, or chips, must often be removed after lamination. If the chips are on exposed surfaces, removal normal to the surface is straightforward. However, chips on internal layers can become mechanically trapped and are difficult to remove.

Three dimensional printing solves a similar problem using a 'support material' that is designed to be easily deformed and removed. This technique is not directly adaptable to PC–MEMS, but a similar approach can mechanically weaken chips by patterned micromachining. Ultrasonic agitation could then cause chips to selectively disintegrate into an easily removable granular medium. Other solutions include:

1. Design devices to have minimal need for scrap chip removal.
2. Highly engineer devices to allow mechanical removal of internal chips.
3. Divide lamination into multiple sublamination steps, allowing simplified chip removal after each lamination (used in Mobee).
4. Investigate introducing a release material.

The lack of a robust framework for handling chip removal limits the design of highly multilayer devices.

4.5.2 Improved locking

The current solder-based locking process has several undesirable features. Locking places selectivity constraints on Mobee's design: the actuator plates must be chrome

plated to protect the solderable exposed nickel electrodes. Also, wing membranes require a second manufacturing pass due to the inability of thin polymer membranes to survive the hydrodynamic and thermal stresses of high temperature solder. Furthermore, lead-based solders are dense: a simple model predicts that solder bond points constitute 12.5% of Mobee's 90mg mass.

A more serious issue, unpredictable solder flow results in reliability problems such as non-uniform fillet shapes and, in extreme cases, total failure of fillet formation. Though locking reliability has not been optimized or explored with statistical significance, the dip-soldering locking technique used for Mobee creates variable fillet shapes with approximately one bonding failure per 20 bond points. Reliability problems have been solved in industrial wave soldering processes, though the complex topologies used in Mobee and other PC–MEMS devices may present a more difficult problem.

4.5.3 Thermal concerns

Some care must be taken to when laminating large regions of materials with dissimilar coefficients of thermal expansion. Without proper design, resulting laminates can assume significant curvature. Though a lesser problem on smaller substrates, thermally-induced curvature of asymmetric layups will be a large concern for mass production using much larger substrates. Symmetric layups, local pin-alignment, and mechanical strain relieving features may combat these thermal issues.

4.5.4 Design software

Improvements in manufacturing come at the cost of design complexity. PC–MEMS combines three-dimensional mechanical engineering found in solid modeling CAD packages with the need to simultaneously create features on many layers underlying PCB design software. All devices presented in this chapter have been designed by directly drawing laser tool paths in 2D sketching software. The requirements are immense; Mobee requires thousands of laser cuts on each of its eighteen design layers. Furthermore, features on internal layers can impact other layers by, for example, requiring access ports. These access ports, numbering in the hundreds, have been created and managed manually.

While an engineer could draft laser cut patterns for HMF components in hours, Mobee's 18-layer monolithic design required three months of effort. The fundamental engineering design work for Mobee occurred over a period of two and a half weeks; labor intensive manual sketching of laser tool paths consumed the balance of time. A lack of tailored design software is at fault, and Mobee's design process was tantamount to designing printed circuit boards before the advent of electronic design automation software. A rudimentary CAD package should easily reduce the latter period to days or hours. A much more sophisticated software system may reduce the former period by aiding the conceptual design of linkages and scaffolds, further reducing the design cycle.

4.6 Conclusion

Concerning the primary goal of improving upon legacy SCM manufacturing techniques, the PC–MEMS process described in this dissertation is a success. The PC–MEMS process bridges the mesoscale gap in manufacturing techniques, providing a versatile framework to produce machines at the millimeter to centimeter scales. PC–MEMS devices are produced monolithically in parallel, an advantage shared by many MEMS processes. This feature promotes mass production, which can be seen in Figure 4.24 depicting the parallel manufacture of 16 PC–MEMS spherical five-bar linkages. In addition, the highly parallel nature of lamination allows shorter lead times; Mobee has been manufactured within 24 hours using academic research facilities. Other features such as material variety and topological complexity bring elements of conventional manufacturing to a MEMS process.

PC–MEMS replaces every manual, skill-intensive SCM step; the resulting process is one that expected to scale readily to larger volumes. PC–MEMS lead times also compare favorably to conventional silicon MEMS, with Mobee manufacturing requiring approximately one day using academic research facilities. The lead time advantage of printed circuit board manufacturing techniques is reflected in industry, with same-day 60-layer printed circuit board prototypes contrasted with the several months typical for MEMS prototyping[2].

Though developed to enable production of millimeter-scale robotic systems, the underlying manufacturing process will have a wide impact beyond the field of robotics. The potential for these larger, more versatile MEMS devices may extend into a diverse

[2]See Rush PCB Inc. of Milpitas, CA and MEMSCAP Inc. of Durham, NC

collection of fields such as medical robotics, power electronics, sensing, spectroscopy, metamaterials, and others.

Chapter 5

The future

5.1 PARITy

Future work exploring the PARITy methodology will proceed along several tracks:

1. Demonstrating long timescale control mechanisms

2. Expanding passive regulation to larger subsets of body forces and torques

3. Incorporating ground-referenced mechanisms

As described in Chapter 2, long timescale control in PARITy enabled FWMAVs will be achieved not by direct modulation of wing kinematic trajectories, but by active modification of system dynamics. For example, the Drag PARITy transmission exhibits short timescale dynamics that balance roll torques from each wing. An active control input could be introduced to bias these dynamics such that they passively regulate the ratio of roll torques τ^L and τ^R from the left and right wings, respectively,

to a specified set point q_3:

$$\tau^L/\tau^R = q_3 \tag{5.1}$$

Note that q_3 is fixed at unity for the simple Drag PARITy transmission. A variety of dynamic parameters within the transmission, such as spring constants and link lengths, can be actively modulated at long timescales to realize this biased short timescale behavior. The potential for simple control relationships such as (5.1), bypassing wing kinematics to directly concern airframe forces and torques, is an exciting result of the PARITy methodology. Demonstration of such control features will motivate one track of future work.

A second research track involves introducing alternative or additional passive degrees of freedom to an FWMAV drivetrain to regulate different or expanded subsets of the body forces and torques produced by the wings. The Drag PARITy drivetrain is a mechanically intelligent device that has demonstrated regulation of body roll torques, arising in part from aerodynamic drag. The Lift PARITy concept is a nascent concept for extending these techniques to lift-aligned torques on the body. The design space of such mechanically intelligent structures is vast, and future work will attempt to produce a variety of force and torque regulating FWMAV structures.

A final track extends body referenced mechanisms to include those responding directly to motion of the body itself in the external frame. A motivating structure is the helicopter Bell stabilizer, essentially a gyroscope that responds to body motion. The analogue for reciprocating system is the bio-inspired haltere [43]. Though generally applied solely as a sensor, a properly designed haltere may be a critical component in a mechanically regulated flapping wing system.

5.2 PC–MEMS

The challenges listed in §4.5 motivate improvement of core PC–MEMS processes. Assembly accuracy needs both optimization and full characterization. Wave solder locking imposes thermal requirements and selectivity constraints, and requires careful attention to solder flow around complex topologies, limitations that motivate investigation of solder masks, solder reflow, and solderless locking in PC–MEMS. The need for physical chip removal and the lack of design software impede the development of devices with extremely high layer counts, also motivating future development.

A desire for increased capabilities is another driving force behind continuing PC–MEMS research. A concrete demonstration of PC–MEMS compatibility with PCB manufacturing should appear in the near future; this expected compatibility provides an avenue to integrate electronics and circuitry directly into the mechanical structure of millimeter-scale machines, greatly expanding their capability. Building off of the successful integration of titanium in Mobee, a fully bio-compatible process would allow entry into medical applications such as surgical tool manufacture. Furthermore, novel integrated mechanisms such as tendons, pick-and place rotational bearings, and MEMS-inspired electromechanical sensors are also topics of research.

A final research objective is the implementation of dedicated mass production facilities for PC–MEMS devices. Panelized Mobee mass production, which may entail tens or even hundreds of individual robots sharing a single assembly scaffold, requires investment in industrial-grade equipment. Investment from the industrial sector awaits only development of PC–MEMS device with commercial value, but raises further questions such as cost of goods optimization, scrap material handling,

roll-to-roll alignment techniques, and other general production line development issues. For a facility focused on the research community, questions about a 'multi-user' process such as MUMPS (Multi-User MEMS Process) must be addressed. Scaling of PC–MEMS production depends fundamentally on demand from scientists and engineers for the novel mesoscale machines it enables.

Bibliography

[1] A. Andersen, U. Pesavento, and Z.J. Wang. Unsteady aerodynamics of fluttering and tumbling plates. *J. Fluid Mech.*, 541:65–90, 2005.

[2] M. Bachman and G. P. Li. MEMS in laminates. In *IEEE Electronic Components and Technology Conf.*, pages 262–267. IEEE, 2011.

[3] A. Baisch and R. J. Wood. Design and fabrication of the harvard ambulatory micro-robot. In *Robotics Research*, volume 70, pages 715–730. Springer, 2011.

[4] J. Y. Bouguet. Camera calibration toolbox for matlab. http://www.vision.caltech.edu/bouguetj/calib_doc/index.html, 2008.

[5] R. W. Brockett. Variational methods for stability of periodic equations. In J. Hale and J. Lasalle, editors, *Differential Equations and Dynamical Systems*, pages 299–308. Academic Press, New York, 1967.

[6] J.M. Bustillo, R.T. Howe, and R.S. Muller. Surface micromachining for microelectromechanical systems. *Proc. IEEE*, 86(8):1552–1574, 1998.

[7] S.P. Chang and M.G. Allen. Demonstration for integrating capacitive pressure sensors with read-out circuitry on stainless steel substrate. *Sensors and Actuators A: Physical*, 116(2):195–204, 2004.

[8] A. Cohen, G. Zhang, F.G. Tseng, U. Frodis, F. Mansfeld, and P. Will. Efab: rapid, low-cost desktop micromachining of high aspect ratio true 3-d mems. In *IEEE Int. Conf. Micro Electro Mech. Syst.*, pages 244–251. IEEE, 1999.

[9] X. Deng, L. Schenato, and S. Sastry. Flapping flight for biomimetic robotic insects: Part ii-flight control design. *IEEE Trans. Rob.*, 22(4):789–803, 2006.

[10] E.R. Deutsch, D. Reyes, E.R. Schildkraut, and J. Kim. High resolution miniature ftir spectrometer enabled by a large linear travel mems pop-up mirror. In *Proc. of SPIE Vol*, volume 7319, pages 73190J–1, 2009.

[11] M. H. Dickinson, F. O. Lehmann, and S. P. Sane. Wing rotation and the aerodynamic basis of insect flight. *Science*, 284:1954–1960, 1999.

[12] W. B. Dickson, A. D. Straw, C. Poelma, and M. H. Dickinson. An integrative model of insect flight control. In *Proc. AIAA Aerospace Sciences Meeting and Exhibit*, Reno, NV, January 2006.

[13] R. S. Fearing, K. H. Chiang, M. H. Dickinson, D. L. Pick, M. Sitti, and J. Yan. Wing transmission for a micromechanical flying insect. *J. Micromechatronics*, 1(3):221–237, 2001.

[14] B.M. Finio, N.O. Perez-Arancibia, and R.J. Wood. System identification and linear time-invariant modeling of an insect-sized flapping-wing micro air vehicle. In *Intelligent Robots and Systems (IROS), 2011 IEEE/RSJ International Conference on*, pages 1107–1114. IEEE, 2011.

[15] B.M. Finio, J.K. Shang, and R.J. Wood. Body torque modulation for a microrobotic fly. In *Robotics and Automation, 2009. ICRA'09. IEEE International Conference on*, pages 3449–3456. IEEE, 2009.

[16] L.G. Fréchette, S.A. Jacobson, K.S. Breuer, F.F. Ehrich, R. Ghodssi, R. Khanna, C.W. Wong, X. Zhang, M.A. Schmidt, and A.H. Epstein. High-speed microfabricated silicon turbomachinery and fluid film bearings. *J. Microelectromech. Syst.*, 14(1):141–152, 2005.

[17] M. Groen, B. Bruggeman, B. Remes, R. Ruijsink, BW Van Oudheusden, and H. Bijl. Improving flight performance of the flapping wing mav delfly ii. In *International Micro Air Vehicle Conference and Flight Competition, Braunschweig, Germany*, 2010.

[18] Katie Hoffman and Robert Wood. Myriapod-like ambulation of a segmented microrobot. *Autonomous Robots*, 31:103–114, 2011.

[19] S. Hollar, S. Bergbreiter, and KSJ Pister. Bidirectional inchworm motors and two-dof robot leg operation. In *TRANSDUCERS, Solid-State Sensors, Actuators and Microsystems, 12th International Conference on, 2003*, volume 1, pages 262–267. IEEE, 2003.

[20] S. Hollar, A. Flynn, C. Bellew, and KSJ Pister. Solar powered 10 mg silicon robot. In *Micro Electro Mechanical Systems, 2003. MEMS-03 Kyoto. IEEE The Sixteenth Annual International Conference on*, pages 706–711. IEEE, 2003.

[21] L. L. Howell. *Compliant Mechanisms*. John Wiley and Sons, Inc., 2001.

[22] E.E. Hui, R.T. Howe, and M.S. Rodgers. Single-step assembly of complex 3-d microstructures. In *IEEE Int. Conf. Micro Electro Mech. Syst.*, pages 602–607. IEEE, 2000.

[23] W. Johnson. *Helicopter theory*. Dover Pubns, 1994.

[24] J.W. Judy. Microelectromechanical systems (MEMS): fabrication, design and applications. *Smart Mater. Struct.*, 10:1115, 2001.

[25] M. Keennon, K. Klingebiel, H. Won, and A. Andriukov. Development of the Nano Hummingbird: A Tailless Flapping Wing Micro Air Vehicle. In *50th AIAA Aerospace Sciences Meeting*, volume 0588, 2012.

[26] M. Kraft, A. Kenda, T. Sandner, and H. Schenk. Mems-based compact ft-spectrometers-a platform for spectroscopic mid-infrared sensors. In *Sensors, 2008 IEEE*, pages 130–133. IEEE, 2008.

[27] J.N. Palasagaram and R. Ramadoss. Mems-capacitive pressure sensor fabricated using printed-circuit-processing techniques. *Sensors Journal, IEEE*, 6(6):1374–1375, 2006.

[28] N.O. Pérez-Arancibia, K.Y. Ma, K.C. Galloway, J.D. Greenberg, and R.J. Wood. First controlled vertical flight of a biologically inspired microrobot. *Bioinspiration & Biomimetics*, 6:036009, 2011.

[29] K.E. Petersen. Silicon as a mechanical material. *Proc. IEEE*, 70(5):420–457, 1982.

[30] K.S.J. Pister, MW Judy, et al. Microfabricated hinges. *Sens. Act. A: Physical*, 33(3):249–256, 1992.

[31] R. Ramadoss, S. Lee, Y. C. Lee, V. M. Bright, and K. C. Gupta. Fabrication, assembly, and testing of RF MEMS capacitive switches using flexible printed circuit technology. *IEEE Trans. Advanced Packaging*, 26(3):248–254, 2003.

[32] P. Sreetharan and R. Wood. Passive torque regulation in an underactuated flapping wing robotic insect. In *Proceedings of Robotics: Science and Systems*, Zaragoza, Spain, June 2010.

[33] P. S. Sreetharan, J. P. Whitney, M. D. Strauss, and R. J. Wood. Monolithic Fabrication of Millimeter-scale Machines. *J. Micromech. Microeng. (accepted)*, 2012.

[34] P. S. Sreetharan and R. J. Wood. Passive aerodynamic drag balancing in a flapping wing robotic insect. *J. Mech. Des.*, 132, 2010.

[35] PS Sreetharan and RJ Wood. Passive torque regulation in an underactuated flapping wing robotic insect. *Autonomous Robots*, pages 1–10, 2011.

[36] R.R.A. Syms, E.M. Yeatman, V.M. Bright, and G.M. Whitesides. Surface tension-powered self-assembly of microstructures-the state-of-the-art. *J. Microelectromech. Syst.*, 12(4):387–417, 2003.

[37] W.C. Tang, T.C.H. Nguyen, M.W. Judy, and R.T. Howe. Electrostatic-comb drive of lateral polysilicon resonators. *Sens. Act. A: Physical*, 21(1-3):328–331, 1990.

[38] J. P. Whitney, P. S. Sreetharan, K. Y. Ma, and R. J. Wood. Pop-up book MEMS. *J. Micromech. Microeng.*, 21(11):115021, 2011.

[39] JP Whitney and RJ Wood. Aeromechanics of passive rotation in flapping flight. *Journal of Fluid Mechanics*, 660(1):197–220, 2010.

[40] R. J. Wood. The first takeoff of a biologically inspired at-scale robotic insect. *IEEE Trans. Rob.*, 24:341–347, 2008.

[41] R. J. Wood, S. Avadhanula, R. Sahai, E. Steltz, and R. S. Fearing. Microrobot design using fiber reinforced composites. *J. Mech. Des.*, 130, 2008.

[42] R. J. Wood, E. Steltz, and R. S. Fearing. Optimal energy density piezoelectric bending actuators. *Sensors & Actuators: A. Physical*, 119(2):476–488, 2005.

[43] W.C. Wu, R.J. Wood, and R.S. Fearing. Halteres for the micromechanical flying insect. In *Robotics and Automation, 2002. Proceedings. ICRA'02. IEEE International Conference on*, volume 1, pages 60–65. IEEE, 2002.

Appendix A

Dynamics Equations

This section describes the dynamics equations used to numerically model all systems described in this dissertation. The fundamental equations model the behavior of the linkage described in §2.3.3, with multiple linkages and constraints handled through the mathematical formulation given in §3.2.

A.1 Nomenclature

$\vec{v}$ = An arbitrary 3×1 vector.

$\hat{v}$ = A 3×1 unit vector.

$\vec{v}^{i}$ = Vector $\vec{v}$ expressed in coordinate frame i, where $i \in \{1, 2, \cdots, 6\}$.

L_i = Link i, where $i \in \{1, 2, \cdots, 6\}$. L_i is fixed in coordinate frame i.

$\hat{s}_i$ = Unit vector indicating the axis of joint i.

γ_i = Angle of joint i, where $i \in \{1, 2, \cdots, 6\}$.

ϕ,θ,ψ = Three configuration angles of the spherical joint, corresponding to joint angles γ_1,γ_4, and γ_6, respectively.

$\vec{p}$ = The 3×1 configuration vector $\begin{bmatrix} \phi & \theta & \psi \end{bmatrix}^T$.

$\frac{\partial}{\partial \vec{p}}$ = The partial derivative with respect to each element of $\vec{p}$, arranged into a row vector, equivalent to $\begin{bmatrix} \frac{\partial}{\partial \phi} & \frac{\partial}{\partial \theta} & \frac{\partial}{\partial \psi} \end{bmatrix}$.

$\hat{x}_i$,$\hat{y}_i$,$\hat{z}_i$ = Unit vectors indicating the x, y, and z axes of frame i, respectively.

$\hat{x}$,$\hat{y}$,$\hat{z}$ = The coordinates of the unit axis vectors, e.g. $\hat{x} = \begin{bmatrix} 1 & 0 & 0 \end{bmatrix}$.

$\mathbf{R}_i^j$ = A 3×3 rotation matrix mapping vectors from frame i to frame j, e.g. $\vec{v}^2 = \mathbf{R}_1^2 \vec{v}^1$.

$\mathbf{R}_{\hat{v}}(\eta)$ = A 3×3 rotation matrix representing a rotation of angle η about the axis $\hat{v}$.

$\mathbf{S}(\vec{v})$ = A 3×3 skew symmetric matrix created from the elements of $\vec{v}$ according to:

$$\mathbf{S}\left(\begin{bmatrix} a & b & c \end{bmatrix}^T\right) = \begin{bmatrix} 0 & -c & b \\ c & 0 & -a \\ -b & a & 0 \end{bmatrix}$$

A.2 Euler-Lagrange formulation

A.2.1 The lagrangian

We first arrange the configuration variables ϕ, θ, and ψ into the state vector $\vec{p}$:

$$\vec{p} = \begin{bmatrix} \phi & \theta & \psi \end{bmatrix}^T \tag{A.1}$$

We form the lagrangian L as the difference between kinetic energy T and potential energy V:

$$L = T(\vec{p}, \dot{\vec{p}}) - V(\vec{p}) \tag{A.2}$$

The equations of motion arise from the Euler-Lagrange equations, written as a (3×1) vector equation:

$$\left(\frac{\mathrm{d}}{\mathrm{d}t} \frac{\partial L}{\partial \dot{\vec{p}}} - \frac{\partial L}{\partial \vec{p}} \right)^T = \vec{\tau}^p \tag{A.3}$$

In terms of kinetic and potential energy, this reduces to:

$$\left(\frac{\mathrm{d}}{\mathrm{d}t} \frac{\partial T}{\partial \dot{\vec{p}}} - \frac{\partial T}{\partial \vec{p}} \right)^T + \left(\frac{\partial V}{\partial \vec{p}} \right)^T = \vec{\tau}^p \tag{A.4}$$

In the preceding equation, τ_i^p refers to a generalized torque about configuration variable p_i, with the superscript p to emphasize that these component torques pertain to the configuration variables, not a particular coordinate frame.

A.2.2 Potential energy

Potential energy in this system arises entirely from the torsion springs at each joint. Assuming the potential energy stored in joint j with joint angle γ_j is the

function $V_j(\gamma_j)$, we have:

$$V = \sum_{j=1}^{6} V_j(\gamma_j) \tag{A.5}$$

The partial derivative with respect to the configuration variables is:

$$\frac{\partial V}{\partial \vec{p}} = \sum_{j=1}^{6} \frac{\partial V_j}{\partial \gamma_j} \begin{bmatrix} \frac{\partial \gamma_j}{\partial \phi} & \frac{\partial \gamma_j}{\partial \theta} & \frac{\partial \gamma_j}{\partial \psi} \end{bmatrix} \tag{A.6}$$

In the case of each joint j being modeled as a simple linear torsion spring with spring constant k_j, we have the equation:

$$\frac{\partial V}{\partial \vec{p}} = \sum_{j=1}^{6} k_j \gamma_j \begin{bmatrix} \frac{\partial \gamma_j}{\partial \phi} & \frac{\partial \gamma_j}{\partial \theta} & \frac{\partial \gamma_j}{\partial \psi} \end{bmatrix} \tag{A.7}$$

There are 18 quantities of the form $\frac{\partial \gamma_j}{\partial p_i}$ which appear in the equations of motion as a result of potential energy stored in joint torsion springs. For completeness, analytical expressions for all of these quantities are recorded in §A.3.

A.2.3 Kinetic energy

Under the assumptions of this dynamics model, the end-effector is the only significant inertia in the system, and it undergoes rigid body rotations about the spherical center of the linkage as described by coordinate frame 6. Define $\vec{\omega}$ to be the angular velocity vector of frame 6 with respect to frame 1 and $\mathbf{I}$ to be the symmetric inertia tensor of the end-effector, constant when expressed in frame 6. Using coordinate frame 6, the kinetic energy has the form:

$$T = \frac{1}{2} \left(\vec{\omega}^6\right)^T \mathbf{I} \vec{\omega}^6 \tag{A.8}$$

Define the Jacobian matrix $\mathbf{J}^6$ as follows:

$$\mathbf{J}^6(\vec{p}) \equiv \begin{bmatrix} \left(\frac{\partial \gamma_5}{\partial \phi} \hat{y}_4^6 + \hat{x}_3^6\right) & \frac{\partial \gamma_5}{\partial \theta} \hat{y}_4^6 & \hat{z}_6^6 \end{bmatrix} \tag{A.9}$$

Expressed in terms of the state variables $\vec{p}$ and $\dot{\vec{p}}$, and the first partial derivatives of joint angles (see §A.3), the angular velocity is:

$$\vec{\omega}^6 = \mathbf{J}^6(\vec{p})\dot{\vec{p}} \tag{A.10}$$

Using this description, we find that the kinetic energy terms in the equations of motion can be written in the form:

$$\left(\frac{\mathrm{d}}{\mathrm{d}t}\frac{\partial T}{\partial \dot{\vec{p}}} - \frac{\partial T}{\partial \vec{p}}\right)^T = \mathbf{M}(\vec{p})\ddot{\vec{p}} + \vec{c}(\vec{p}, \dot{\vec{p}}) \tag{A.11}$$

The detailed derivations of $\vec{c}(\vec{p}, \dot{\vec{p}})$ and the mass matrix $\mathbf{M}(\vec{p})$ are presented in §A.3.

A.2.4 External torques

For many cases, it is necessary to consider forces and torques applied to the end-effector. For example, aerodynamic effects give rise to force distributions on a flapping wing, while a manipulator or robotic leg receives reaction forces from the environment. Due to the simple spherical motion of the end-effector, only an arbitrary applied torque $\vec{\tau}_{\text{ext}}$ need be considered. The Jacobian allows mapping of this torque into the generalized torques appearing in the equations of motion:

$$\begin{bmatrix} \tau_1^p \\ \tau_2^p \\ \tau_3^p \end{bmatrix} = \left(\mathbf{J}^6\right)^T \vec{\tau}_{\text{ext}}^6 \tag{A.12}$$

A.2.5 The equations of motion

The final equations of motion, expressed as a 3×1 vector equation, are:

$$\mathbf{M}(\vec{p})\ddot{\vec{p}} + \vec{c}(\vec{p}, \dot{\vec{p}}) + \sum_{j=1}^{6} \frac{\partial V_j}{\partial \gamma_j}\left(\frac{\partial \gamma_j}{\partial \vec{p}}\right)^T = \vec{\tau}^p \tag{A.13}$$

A.3 List of analytical expressions

A.3.1 A note on overdetermined equations

Many quantities in the following section are defined in overdetermined sets equations. For example, for quantities x and y, an equation of the following form with known (3×2) matrix $\mathbf{M}$ and (3×1) vector $\vec{v}$ is overdetermined:

$$\mathbf{M} \begin{pmatrix} x \\ y \end{pmatrix} = \vec{v} \tag{A.14}$$

In the cases given, a solution exists despite the overdetermined nature. One method of finding the solution is to use a pseudoinverse of the matrix $\mathbf{M}$:

$$\begin{pmatrix} x \\ y \end{pmatrix} = \left(\mathbf{M}^T\mathbf{M}\right)^{-1}\mathbf{M}^T\vec{v} \tag{A.15}$$

A.3.2 First partial derivatives of joint angles

This section will provide expressions for the eighteen quantities of the form $\frac{\partial \gamma_k}{\partial p_i}$ where $k \in \{1,2,3,4,5,6\}$ and $p \in \{1,2,3\}$, useful for building a dynamic model of this linkage. Since γ_1, γ_4, and γ_6 are defined to be ϕ, θ, and ψ, respectively, the relevant partial derivatives are straightforward:

$$\begin{bmatrix} \frac{\partial \gamma_1}{\partial \phi} & \frac{\partial \gamma_1}{\partial \theta} & \frac{\partial \gamma_1}{\partial \psi} \\ \frac{\partial \gamma_4}{\partial \phi} & \frac{\partial \gamma_4}{\partial \theta} & \frac{\partial \gamma_4}{\partial \psi} \\ \frac{\partial \gamma_6}{\partial \phi} & \frac{\partial \gamma_6}{\partial \theta} & \frac{\partial \gamma_6}{\partial \psi} \end{bmatrix} = \begin{bmatrix} 1 & 0 & 0 \\ 0 & 1 & 0 \\ 0 & 0 & 1 \end{bmatrix} \tag{A.16}$$

Since the remaining joint angles (γ_2, γ_3, and γ_5) are functions of only ϕ and θ, we have:

$$\frac{\partial \gamma_2}{\partial \psi} = \frac{\partial \gamma_3}{\partial \psi} = \frac{\partial \gamma_5}{\partial \psi} = 0 \tag{A.17}$$

By taking partial derivatives of the constraint equation (2.8), we arrive at the following linear equations allowing straightforward calculation of $\frac{\partial \gamma_2}{\partial \phi}$, $\frac{\partial \gamma_2}{\partial \theta}$, $\frac{\partial \gamma_5}{\partial \phi}$, and $\frac{\partial \gamma_5}{\partial \theta}$:

$$\mathbf{S}(\hat{x}_1^1)\hat{s}_3^1 = \begin{bmatrix} \mathbf{S}(\hat{x}_2^1)\hat{s}_3^1 & -\mathbf{S}(\hat{y}_3^1)\hat{s}_3^1 \end{bmatrix} \begin{bmatrix} \frac{\partial \gamma_2}{\partial \phi} \\ \frac{\partial \gamma_5}{\partial \phi} \end{bmatrix} \tag{A.18}$$

$$-\mathbf{S}(\hat{y}_1^1)\hat{s}_3^1 = \begin{bmatrix} \mathbf{S}(\hat{x}_2^1)\hat{s}_3^1 & -\mathbf{S}(\hat{y}_3^1)\hat{s}_3^1 \end{bmatrix} \begin{bmatrix} \frac{\partial \gamma_2}{\partial \theta} \\ \frac{\partial \gamma_5}{\partial \theta} \end{bmatrix} \tag{A.19}$$

Finally, the following expressions allow calculation of partial derivatives of γ_3:

$$\frac{\partial \gamma_3}{\partial \phi} = \left(\hat{s}_3^5 \cdot \hat{x}_1^5\right) - \frac{\partial \gamma_2}{\partial \phi}\left(\hat{s}_3^5 \cdot \hat{x}_5^5\right) + \frac{\partial \gamma_5}{\partial \phi}\left(\hat{s}_3^5 \cdot \hat{y}_3^5\right) \tag{A.20}$$

$$\frac{\partial \gamma_3}{\partial \theta} = -\left(\hat{s}_3^5 \cdot \hat{y}_2^5\right) - \frac{\partial \gamma_2}{\partial \theta}\left(\hat{s}_3^5 \cdot \hat{x}_5^5\right) + \frac{\partial \gamma_5}{\partial \theta}\left(\hat{s}_3^5 \cdot \hat{y}_3^5\right) \tag{A.21}$$

A.3.3 Second partial derivatives of joint angles

This section describes calculation of the six second partial derivatives $\frac{\partial^2 \gamma_2}{\partial \phi^2}$, $\frac{\partial^2 \gamma_2}{\partial \phi \partial \theta}$, $\frac{\partial^2 \gamma_2}{\partial \theta^2}$, $\frac{\partial^2 \gamma_5}{\partial \phi^2}$, $\frac{\partial^2 \gamma_5}{\partial \phi \partial \theta}$, and $\frac{\partial^2 \gamma_5}{\partial \theta^2}$, all of which appear in the equations of motion. Several intermediate quantities will be defined to simplify the resulting expressions:

$$\frac{\partial}{\partial \phi}\hat{s}_3^1 = \left(\mathbf{S}(\hat{x}_1^1) + \frac{\partial \gamma_5}{\partial \phi}\mathbf{S}(\hat{y}_3^1)\right)\hat{s}_3^1 \tag{A.22}$$

$$\frac{\partial}{\partial \phi}\mathbf{S}(\hat{y}_3^1) = \mathbf{S}(\hat{x}_1^1)\mathbf{S}(\hat{y}_3^1) - \mathbf{S}(\hat{y}_3^1)\mathbf{S}(\hat{x}_3^1) \tag{A.23}$$

$$\frac{\partial}{\partial \theta}\hat{s}_3^1 = \frac{\partial \gamma_5}{\partial \theta}\mathbf{S}(\hat{y}_3^1)\hat{s}_3^1 \tag{A.24}$$

$$\frac{\partial}{\partial \theta}\mathbf{S}(\hat{x}_2^1) = \mathbf{S}(\hat{y}_1^1)\mathbf{S}(\hat{x}_2^1) - \mathbf{S}(\hat{x}_2^1)\mathbf{S}(\hat{y}_2^1) \tag{A.25}$$

Using these intermediate quantities, linear equations can be written that allow calculation of all six second partial derivatives, presented in eqns (A.26), (A.27), and (A.28).

$$\left[\, \mathbf{S}(\hat{x}_2^1)\hat{s}_3^1 \; -\mathbf{S}(\hat{y}_3^1)\hat{s}_3^1 \,\right] \begin{bmatrix} \frac{\partial^2 \gamma_2}{\partial \phi^2} \\ \frac{\partial^2 \gamma_5}{\partial \phi^2} \end{bmatrix} = \mathbf{S}(\hat{x}_1^1)\frac{\partial}{\partial \phi}\hat{s}_3^1 + \left[\, -\mathbf{S}(\hat{x}_2^1)\frac{\partial}{\partial \phi}\hat{s}_3^1 \; \left(\left(\frac{\partial}{\partial \phi}\mathbf{S}(\hat{y}_3^1)\right)\hat{s}_3^1 + \mathbf{S}(\hat{y}_3^1)\frac{\partial}{\partial \phi}\hat{s}_3^1\right) \,\right] \begin{bmatrix} \frac{\partial \gamma_2}{\partial \phi} \\ \frac{\partial \gamma_5}{\partial \phi} \end{bmatrix} \quad \text{(A.26)}$$

$$\left[\, \mathbf{S}(\hat{x}_2^1)\hat{s}_3^1 \; -\mathbf{S}(\hat{y}_3^1)\hat{s}_3^1 \,\right] \begin{bmatrix} \frac{\partial^2 \gamma_2}{\partial \theta^2} \\ \frac{\partial^2 \gamma_5}{\partial \theta^2} \end{bmatrix} = -\mathbf{S}(\hat{y}_1^1)\frac{\partial}{\partial \theta}\hat{s}_3^1 + \left[\, -\left(\left(\frac{\partial}{\partial \theta}\mathbf{S}(\hat{x}_2^1)\right)\hat{s}_3^1 + \mathbf{S}(\hat{x}_2^1)\frac{\partial}{\partial \theta}\hat{s}_3^1\right) \; \mathbf{S}(\hat{y}_3^1)\frac{\partial}{\partial \theta}\hat{s}_3^1 \,\right] \begin{bmatrix} \frac{\partial \gamma_2}{\partial \theta} \\ \frac{\partial \gamma_5}{\partial \theta} \end{bmatrix} \quad \text{(A.27)}$$

$$\left[\, \mathbf{S}(\hat{x}_2^1)\hat{s}_3^1 \; -\mathbf{S}(\hat{y}_3^1)\hat{s}_3^1 \,\right] \begin{bmatrix} \frac{\partial^2 \gamma_2}{\partial \phi \partial \theta} \\ \frac{\partial^2 \gamma_5}{\partial \phi \partial \theta} \end{bmatrix} = \mathbf{S}(\hat{x}_1^1)\frac{\partial}{\partial \theta}\hat{s}_3^1 + \left[\, -\left(\left(\frac{\partial}{\partial \theta}\mathbf{S}(\hat{x}_2^1)\right)\hat{s}_3^1 + \mathbf{S}(\hat{x}_2^1)\frac{\partial}{\partial \theta}\hat{s}_3^1\right) \; \mathbf{S}(\hat{y}_3^1)\frac{\partial}{\partial \theta}\hat{s}_3^1 \,\right] \begin{bmatrix} \frac{\partial \gamma_2}{\partial \phi} \\ \frac{\partial \gamma_5}{\partial \phi} \end{bmatrix} \quad \text{(A.28)}$$

A.3.4 Kinetic energy terms

The purpose of this section is to provide an analytical expressions for the mass matrix $M(\vec{p})$ and the Coriolis vector $\vec{c}(\vec{p}, \dot{\vec{p}})$. To simplify these expressions, various derivatives of the angular velocity $\vec{\omega}$ of the end-effector with respect to ground will be described.

Eqns (A.30), (A.31), and (A.32) describe the components of $\frac{\partial \vec{\omega}^6}{\partial \vec{p}}$, while $\frac{\partial \vec{\omega}^6}{\partial \dot{\vec{p}}}$ is calculated as follows:

$$\frac{\partial \vec{\omega}}{\partial \dot{\vec{p}}} = \begin{bmatrix} \left(\hat{y}_4^6 \frac{\partial \gamma_5}{\partial \phi} + \hat{x}_3^6\right) & \left(\hat{y}_4^6 \frac{\partial \gamma_5}{\partial \theta}\right) & \left(\hat{z}_6^6\right) \end{bmatrix} \quad \text{(A.29)}$$

The components of the total time derivative $\frac{\mathrm{d}}{\mathrm{dt}}\frac{\partial \vec{\omega}^6}{\partial \dot{\vec{p}}}$ are presented in eqns (A.33), (A.34), and (A.35). Using one final intermediate quantity $\vec{b}$ presented in (A.37), the Coriolis vector $\vec{c}(\vec{p}, \dot{\vec{p}})$ is described in (A.38) and the mass matrix $\mathbf{M}$ is:

$$\mathbf{M}(\vec{p}) = \left(\frac{\partial \vec{\omega}^6}{\partial \dot{\vec{p}}}\right)^T \mathbf{I}^6 \begin{bmatrix} \left(\hat{x}_3^6 + \hat{y}_4^6 \frac{\partial \gamma_5}{\partial \phi}\right) & \hat{y}_4^6 \frac{\partial \gamma_5}{\partial \theta} & \hat{z}_6^6 \end{bmatrix} \quad \text{(A.36)}$$

$$\frac{\partial\vec{\omega}^6}{\partial\phi} = \left(\frac{\partial^2\gamma_5}{\partial^2\phi}\hat{y}_4^6 - \frac{\partial\gamma_5}{\partial\phi}\mathbf{S}(\hat{y}_4^6)\hat{x}_3^6\right)\dot{\phi} + \left(\frac{\partial^2\gamma_5}{\partial\phi\partial\theta}\hat{y}_4^6\right)\dot{\theta} \tag{A.30}$$

$$\frac{\partial\vec{\omega}^6}{\partial\theta} = \left(\frac{\partial^2\gamma_5}{\partial\phi\partial\theta}\hat{y}_4^6 - \frac{\partial\gamma_5}{\partial\theta}\mathbf{S}(\hat{y}_4^6)\hat{x}_3^6\right)\dot{\phi} + \left(\frac{\partial^2\gamma_5}{\partial^2\theta}\hat{y}_4^6\right)\dot{\theta} \tag{A.31}$$

$$\frac{\partial\vec{\omega}^6}{\partial\psi} = -\left(\frac{\partial\gamma_5}{\partial\phi}\mathbf{S}(\hat{z}_6^6)\hat{y}_4^6 + \mathbf{S}(\hat{z}_6^6)\hat{x}_3^6\right)\dot{\phi} - \left(\frac{\partial\gamma_5}{\partial\theta}\mathbf{S}(\hat{z}_6^6)\hat{y}_4^6\right)\dot{\theta} \tag{A.32}$$

$$\begin{aligned}\frac{\mathrm{d}}{\mathrm{d}t}\left(\frac{\partial\vec{\omega}}{\partial\dot{\phi}}\right) = &\left(\frac{\partial^2\gamma_5}{\partial\phi^2}\hat{y}_4^6 - \frac{\partial\gamma_5}{\partial\phi}\mathbf{S}(\hat{y}_4^6)\hat{x}_3^6\right)\dot{\phi} + \left(\frac{\partial^2\gamma_5}{\partial\phi\partial\theta}\hat{y}_4^6 - \frac{\partial\gamma_5}{\partial\theta}\mathbf{S}(\hat{y}_4^6)\hat{x}_3^6\right)\dot{\theta} \\ &- \mathbf{S}(\hat{z}_6^6)\left(\frac{\partial\gamma_5}{\partial\phi}\hat{y}_4^6 + \hat{x}_3^6\right)\dot{\psi}\end{aligned} \tag{A.33}$$

$$\frac{\mathrm{d}}{\mathrm{d}t}\left(\frac{\partial\vec{\omega}}{\partial\dot{\theta}}\right) = \left(\frac{\partial^2\gamma_5}{\partial\phi\partial\theta}\hat{y}_4^6\right)\dot{\phi} + \left(\frac{\partial^2\gamma_5}{\partial\theta^2}\hat{y}_4^6\right)\dot{\theta} - \left(\frac{\partial\gamma_5}{\partial\theta}\mathbf{S}(\hat{z}_6^6)\hat{y}_4^6\right)\dot{\psi} \tag{A.34}$$

$$\frac{\mathrm{d}}{\mathrm{d}t}\left(\frac{\partial\vec{\omega}}{\partial\dot{\psi}}\right) = \vec{0} \tag{A.35}$$

$$\begin{aligned}\vec{b}(\vec{p},\dot{\vec{p}}) \equiv &\left(\hat{y}_4^6\frac{\partial^2\gamma_5}{\partial\phi^2} - \mathbf{S}(\hat{y}_4^6)\hat{x}_3^6\frac{\partial\gamma_5}{\partial\phi}\right)\dot{\phi}^2 + \left(\hat{y}_4^6\frac{\partial^2\gamma_5}{\partial\theta^2}\right)\dot{\theta}^2 \\ &+ \left(2\hat{y}_4^6\frac{\partial^2\gamma_5}{\partial\phi\partial\theta} - \mathbf{S}(\hat{y}_4^6)\hat{x}_3^6\frac{\partial\gamma_5}{\partial\theta}\right)\dot{\phi}\dot{\theta} \\ &+ \left(-\mathbf{S}(\hat{z}_6^6)\hat{y}_4^6\frac{\partial\gamma_5}{\partial\phi} - \mathbf{S}(\hat{z}_6^6)\hat{x}_3^6\right)\dot{\phi}\dot{\psi} + \left(-\mathbf{S}(\hat{z}_6^6)\hat{y}_4^6\frac{\partial\gamma_5}{\partial\theta}\right)\dot{\theta}\dot{\psi}\end{aligned} \tag{A.37}$$

$$\vec{c}(\vec{p},\dot{\vec{p}}) = \left(\frac{\partial\vec{\omega}^6}{\partial\dot{\vec{p}}}\right)^T\mathbf{I}^6\vec{b}(\vec{p},\dot{\vec{p}}) + \left(\frac{\mathrm{d}}{\mathrm{d}t}\frac{\partial\vec{\omega}^6}{\partial\dot{\vec{p}}} - \frac{\partial\vec{\omega}^6}{\partial\vec{p}}\right)^T\mathbf{I}^6\vec{\omega} \tag{A.38}$$